



# The contribution of shipping to air pollution in the Mediterranean region – a multimodel evaluation: Comparison of photooxidants NO<sub>2</sub> and O<sub>3</sub>

Lea Fink<sup>1</sup>, Matthias Karl<sup>1</sup>, Volker Matthias<sup>1</sup>, Sonia Oppo<sup>2</sup>, Richard Kranenburg<sup>3</sup>, Jeroen Kuenen<sup>3</sup>, Jana  
5 Moldanova<sup>4</sup>, Sara Jutterström<sup>4</sup>, Jukka-Pekka Jalkanen<sup>5</sup>, Elisa Majamäki<sup>5</sup>

<sup>1</sup>Helmholtz-Centre Hereon, Institute of Coastal Environmental Chemistry, 21502 Geesthacht, Germany

<sup>2</sup>AtmoSud, Air Quality Observatory in the Provence-Alpes-Côte d'Azur region, 13006 Marseille, France

<sup>3</sup>TNO, Netherlands Organization for Applied Scientific Research, 3584 CB Utrecht, The Netherlands

<sup>4</sup>IVL, Swedish Environmental Research Institute, 411 33 Göteborg, Sweden

10 <sup>5</sup>FMI, Finnish Meteorological Institute, FI-00560 Helsinki, Finland

*Correspondence to:* Lea Fink (lea.fink@hereon.de)

**Abstract.** Shipping has a significant contribution to the emissions of air pollutants such as NO<sub>x</sub> and particulate matter (PM), and the global maritime transport volumes are projected to increase further in the future. The Mediterranean Sea contains the major route for short sea shipping within Europe and contains the main shipping route between Europe and East Asia. Thus,  
15 it is a highly frequented shipping area, and high levels of air pollutants with significant contributions from shipping emissions are observed at monitoring stations in many cities along the Mediterranean coast.

The present study is part of the EU H2020 project SCIPPER (Shipping contribution to Inland Pollution Push for the Enforcement of Regulations). Five different regional chemistry transport models (CAMx, CHIMERE, CMAQ, EMEP, LOTOS-EUROS) were used to simulate the transport, chemical transformation and fate of atmospheric pollutants in the  
20 Mediterranean Sea for 2015. Shipping emissions were calculated with STEAM version 3.3.0, and land-based emissions were taken from the CAMS-REG v2.2.1 dataset for a domain covering the Mediterranean Sea on a resolution of 12x12 km<sup>2</sup> (or 0.1° x 0.1°). All models used their standard setup for further input. Ship contribution was calculated with the zero-out method. One run using the tagging method was performed with LOTOS-EUROS. The model outputs were compared against each other and to measured background data at monitoring stations.

25 The results showed differing outputs regarding the time series and pattern of model outputs but similar results with regard to the overall underestimation of NO<sub>2</sub> and overestimation of O<sub>3</sub>. The contribution from ships to the total NO<sub>2</sub> concentration was especially high at the main shipping routes and coastal regions (25% to 85%). The contribution from ships to the total O<sub>3</sub> concentration was lowest in regions with the highest NO<sub>2</sub> contribution (down to -20%). A comparison of the zero-out and tagging methods has shown that the annual mean ship contribution to the total NO<sub>2</sub> concentration is smaller (up to 75%) and  
30 has a lower range when the tagging method is used. CAMx and CHIMERE simulated the highest ship contributions to the NO<sub>2</sub> and O<sub>3</sub> air concentrations. Additionally, the strongest correlation was found between CAMx and CHIMERE, which can be traced back to the usage of the same meteorological input data. The CMAQ, EMEP and LOTOS-EUROS simulated values



were within one range for the  $\text{NO}_2$  and  $\text{O}_3$  air concentrations. Regarding deposition output, larger differences between the models were found when compared to air concentration. These uncertainties and deviations between models are caused by  
35 deposition mechanisms, which are unique within each model. A reliable output from models simulating ship contributions can be expected for air concentrations of  $\text{NO}_2$  and  $\text{O}_3$ .

## 1 Introduction

Shipping activity and freight transport via ships are growing, and previous studies have shown that the relative contribution from shipping to total air pollution will also increase (Brandt et al., 2013). Once in the atmosphere, these emissions are  
40 transported over several hundreds of kilometers, with 70 % of shipping emissions occurring less than 400 km from the coast (Eyring et al., 2010; Endresen et al., 2003). Several previous studies have pointed out the negative effect of shipping emissions on the concentration of air pollutants, playing a role as greenhouse gases, impacting human health or contributing to acidification and eutrophication (Tysro and Berge, 1997; Corbett and Fischbeck, 1997; Corbett et al., 1999).

Nevertheless, maritime transport plays a vital role in the international trade of goods worldwide as well as in the European  
45 Union (EU). The Eurostat Press Office (2016) stated that for 2015, the value of EU trade of goods with non-EU countries transported by the sea was approximately 51% of EU traded goods. The Mediterranean Sea contains one main shipping route between Europe and Asia, being the region in Europe with maximal contribution from shipping emissions to gaseous pollutants, in addition to the North Sea (Viana et al., 2014).

Additionally, as one of the fastest growing sources of greenhouse gas emissions, shipping emissions directly result in health  
50 problems and have adverse effects on ecosystems (Brandt et al., 2013). The wide range of gaseous pollutants, such as nitrogen oxides ( $\text{NO}_x = \text{NO}_2 + \text{NO}$ ), coming from shipping emissions have negative impacts by forming smog and acid rain and contribute to eutrophication (Jägerbrand et al., 2019; Brandt et al., 2013; Karl et al., 2019b; Matthias et al., 2010).

Moreover,  $\text{NO}_x$ , as a primary pollutant, plays an important role in the formation of  $\text{O}_3$  and in the deposition of reactive nitrogen compounds (Eyring et al., 2010). The oxidation of VOCs (volatile organic compounds) produces ozone in the troposphere  
55 when  $\text{NO}_x$  and sunlight are present.  $\text{O}_3$  can inflame and damage the respiratory system, make the lungs more susceptible to infection and intensify lung diseases (EPA, 2021). Although it is not directly emitted,  $\text{O}_3$  is an important compound in photochemistry. Especially in the Mediterranean Sea during summer, when radiation is high, the contribution of shipping emissions to mean surface  $\text{O}_3$  concentrations can be significant (Aksoyoglu et al., 2016).

Atmospheric nitrogen deposition mainly comes from agricultural activities and combustion processes such as those in shipping  
60 (Aksoyoglu et al., 2016). This increase in bioavailable nitrogen deposition causes eutrophication (Jägerbrand et al., 2019). The deposition of  $\text{O}_3$  affects the plant's stomata, damages the plants, changes water and carbon cycling and reduces crop yields (Clifton et al., 2020).



Chemistry transport models (CTMs) can be applied to simulate the transport of air pollutants as well as chemical transformation and deposition. These models can be used at different scales, depending on the domain they cover and the question to be answered.

Although shipping emissions have a significant impact on air pollution by NO<sub>2</sub> in the Mediterranean Sea (Marmer and Langmann, 2005), few regional-scale chemistry transport modeling studies have focused on this domain. A literature review study focusing on the assessment of the impacts of shipping emissions on air quality in European coastal areas by Viana et al. (2014) showed that studies regarding shipping emissions in the Mediterranean Sea emphasize PM<sub>x</sub> levels and their chemical composition instead of gaseous pollutants. Marmer and Langmann (2005) investigated the Mediterranean Sea, but on a larger scale or without the comparison of different CTMs. Other studies focus on smaller domains over the Iberian Peninsula (Baldasano et al., 2011; Nunes et al., 2020), the eastern part of the Mediterranean Sea with the Arabian Peninsula (Večera et al., 2008; Tadic et al., 2020; Celik et al.; Friedrich et al., 2021) or urban scale and harbor cities (Schembari et al., 2012; Donato et al., 2014; Prati et al., 2015). However, none of these studies modeled the ship contribution on a regional scale with a subsequent model comparison of different chemical transport models. A comparison of outputs of regional-scale chemistry transport models was performed for the Baltic Sea or for all of Europe (Karl et al., 2019a; Im et al., 2015a) but not exclusively for the western Mediterranean region.

Dry deposition is a substantial sink for atmospheric pollutants. Furthermore, it determines the net flux of pollutants to the Earth's surface (Galmarini et al., 2021). Accurate estimates of dry deposition are required for reliable predictions of atmospheric concentrations, since it is an important loss process scaling with concentrations close to the ground (Emerson et al., 2020; Vivanco et al., 2018). NO<sub>2</sub> deposition contributes to eutrophication, followed by biodiversity loss, whereas O<sub>3</sub> dry deposition injures plant tissues and reduces plant productivity (Vivanco et al., 2018; Clifton et al., 2020). The deposition of N and S was investigated in previous studies (i.e., Vivanco et al., 2018; Jutterström et al., 2021; Galmarini et al., 2021). Nevertheless, few studies have performed model intercomparison for dry deposition; thus far, none of the studies have focused on ship impact over the western part of the Mediterranean Sea. Comparing the dry deposition mechanisms of different models is essential since these mechanisms are unique for each model. In Galmarini et al. (2021), deposition schemes of different models were compared, including LOTOS-EUROS and CMAQ, which are also part of the present study. They showed, i.e., Differences in surface resistance calculation and deposition pathways: LOTOS-EUROS uses a single deposition pathway to soil. In comparison, CMAQ uses two deposition pathways for deposition to soil (one for vegetation-covered and one for bare soil).

Additionally, another important factor is the land use-land cover (LUCL) on which dry deposition strongly depends but is unique in each model. This was also stated by Vivano et al. (2018), explaining that even if models apply similar algorithms in their deposition schemes, they may use different land use or leaf index area data. Thus, mainly over land areas, differences in model outputs are to be expected. A similar mechanism and model output for dry deposition is expected over water and therefore over most of the considered domain in the present study.



The Ship Traffic Emission Assessment Model (STEAM) has been previously applied to evaluate shipping emissions in different regions, such as the North Sea or Baltic Sea (Jalkanen et al., 2009; Jonson et al., 2015; Aulinger et al., 2016; Barregard et al., 2019) or the Iberian Peninsula (Nunes et al., 2020), as well as in European (Jalkanen et al., 2016) and global regions (Johansson et al., 2017). However, the model has not been previously used in a study focusing entirely on the western  
100 Mediterranean Sea region.

In addition, the Mediterranean Sea is not yet the ECA (Emission Control Area). The contracting parties of the Barcelona Convention agreed to designate the Mediterranean Sea as an Emission Control Area for Sulfur emissions (MedECA) by 2025. Nevertheless, although SO<sub>2</sub> emissions must be reduced by 50 % to 80 % by 2030, NO<sub>x</sub> emissions from ships will grow without further control and likely exceed emissions from land-based sources in the European Union after 2030 (Cofala et al., 2018).  
105 Furthermore, the current state of air pollution is calculated to have a basis for investigating the effects of additional legislation. It is important to simulate the ship contribution to several air pollutants to show the impact of ships in a larger area.

The Horizon 2020 SCIPPER project (Shipping Contributions to Inland Pollution Push for the Enforcement of Regulations) aims to determine how existing regulations ensure compliance with the legislation on emissions to air from ships. One part of this project was to focus on CTMs and their possible supportive effects in the monitoring of compliance of threshold levels.

The present study compares and evaluates five different CTMs concerning their predictions of the dispersion and transformation of air pollutants. The main focus of this study is to compare the output of models regarding the ship contribution to atmospheric concentrations and dry deposition of NO<sub>2</sub> and O<sub>3</sub>. Using this comparison, important differences in the photochemical processing between the models and the balance of photochemistry in the models focusing on shipping will be highlighted. Furthermore, the model performance was quantified by comparing the modeled data against the measured data of  
115 air pollutants at background stations in coastal areas of the Mediterranean Sea. The performance of the models was compared based on statistical indicators.

By using five different CTMs in this part of the SCIPPER project, a more robust estimate of the ship contribution to the air pollution can be given. To date, the present study is the first multimodel study to compare ship contributions to five regional-scale CTMs in the Mediterranean Sea.

## 120 **2 Materials and Methods**

### **2.1 Models**

Five different regional-scale CTMs were used for this study, run by four institutions: CAMx and CHIMERE by AtmoSud, CMAQ by Helmholtz Centre Hereon, EMEP by IVL Swedish Environmental Research Institute and LOTOS-EUROS by TNO Netherlands Organization for applied scientific research.

The goal was to have a model setup as similar as possible for all models to receive comparable outputs. As a base, an inner and outer domain with grid resolution was established. Additionally, the emissions were provided for one year. Especially of  
125 importance in the present study was the method for calculating the ship contribution.



An overview of the input data is shown in Table 1. Input data were the same for shipping emissions using STEAM (version 3.3.0.; Jalkanen et al., 2009; Jalkanen et al., 2012; Johansson et al., 2013; Johansson et al., 2017), land-based emissions  
 130 (CAMS-REG, v2.0) as well as projection (WGS84\_lonlat), domain (Mediterranean Sea), resolution ( $0.1^\circ \times 0.1^\circ$ ,  $12 \times 12$  km) and the modeled year (2015). Input data were different for meteorological input data, boundary and initial conditions because the CTMs used their standard setup.

The output of the model runs should all contain  $\text{NO}_2$  and  $\text{O}_3$  in  $\mu\text{g}/\text{m}^3$  at an hourly resolution on a 2D grid from the lowest layer and be provided as a netcdf file following CF conventions. The lowest layer on the ground was used in the present study.  
 135 With all models, a reference run for the current air quality situation was performed, including all emissions (base case). Furthermore, all models did one run without the emissions from shipping (noship case). The difference between the calculations with all emissions and the calculation without shipping emissions is used to determine the contribution of ships to the ambient pollutant concentration (zero-out method). This was done for all five models.

One run was performed with the tagging method by LOTOS-EUROS. In the tagging method, emitted species are tagged  
 140 according to their emission source. These are not necessarily sectors but can also be countries, regions, time of emission, etc. These tags are transferred to other species during the subsequent chemical reactions, where conserved atoms C, N and S are tracked throughout the chemical calculations. Because  $\text{O}_3$  is not directly emitted, the tagging method cannot be used directly to tag  $\text{O}_3$ , so the tagging method is not applied for ozone in this study. This results in a model calculation with identical chemical behavior, while zero-out methods change the chemical behavior of the model. In this study, a tag was placed on the  
 145 shipping emissions to obtain the shipping contribution of the current chemical regime. For a comparison of the different ship contribution methods, LOTOS-EUROS also performed a run with the zero-out method.

**Table 1: Main model parameters and input data for the five chemical transport models.**

<b>Model parameter</b>	<b>CAMx</b>	<b>CHIMERE</b>	<b>CMAQ</b>	<b>EMEP</b>	<b>LOTOS-EUROS</b>
<b>Grid resolution inner domain</b>	12x12 km <sup>2</sup>	12x12 km <sup>2</sup>	12x12 km <sup>2</sup>	$0.1^\circ \times 0.1^\circ$	$0.1^\circ \times 0.1^\circ$
<b>Grid resolution outer domain</b>	36x36 km <sup>2</sup>	36x36 km <sup>2</sup>	36x36 km <sup>2</sup>	none	$0.5^\circ \times 0.25^\circ$
<b>Land-based emissions</b>	CAMS-REG	CAMS-REG	CAMS-REG	CAMS-REG	CAMS-REG
<b>Shipping emissions</b>	STEAM	STEAM	STEAM	STEAM	STEAM
<b>Meteorological driver</b>	WPS/WRF	WPS/WRF	COSMO-5 CLM	ECMWF (IFS)	ECWMF (IFS)



<b>Boundary conditions</b>	Mozart-4 output	Gaseous species: LMDz-INCA model  Aerosols: GOCART model	IFS_CAMS cycle45r1	boundary conditions provided with the open source model distribution for year 2015	CAMS C-IFS
----------------------------	-----------------	--	--------------------	--	------------

### 2.1.1 Model description CAMx

150 CAMx (Comprehensive Air Quality Model with Extensions) is a Eulerian photochemical dispersion model developed by Ramboll Environ. Version CAMx v6.50 of the model was used in the present study.

For this study, a first domain with a 36 km resolution was defined at the European scale. A second nested domain was defined, named MEDI12 (147x249 points), and covered the center of Europe with a resolution of 12 km. Both meteorological and chemical transport simulations were provided for these domains. WRFv3.9 was run for the simulation of meteorological conditions with 28 vertical layers up to 50 hPa, with FNL data for initial conditions.

155 For the CAMx simulation, boundary conditions from the Mozart-4 output and the PSAT and OSAT modules (Particulate Source Apportionment Technology and Ozone Source Apportionment Technology) were activated to quantify the aerosol and ozone sources in Europe and especially the contribution from maritime emissions.

The gas phase chemical mechanism is CB05, in which the NMVOC emissions are split into 13 species (TERP, ISOP, XYL, 160 TOL, ETOH, MEOH, IOLE, OLE, ETH, ALD2, PAR, ETHA and FORM) and describe approximately 156 reactions. For semivolatile inorganic species (sulfate, nitrate, and ammonium), the equilibrium concentration is calculated using the thermodynamic model ISORROPIA (Nenes et al., 1998). Fourteen vertical levels are simulated with a first layer height of approximately 10 km.

### 2.1.2 Model description Chimere

165 CHIMERE is an offline chemistry transport model developed by LMD-IPSL/CNRS (Menuet et al., 2013). The CHIMERE2017r4 version of the model was used in this study.

WRFv3.9 (Weather Research and Forecasting Model) was run for the simulation of meteorological conditions with 28 vertical layers up to 50 hPa, with FNL data for initial conditions.

Concerning CHIMERE simulation, boundary conditions are monthly mean climatologies taken from the LMDz-INCA model (Laboratoire de Météorologie Dynamique General Circulation Model – Interaction with Chemistry and Aerosols; Schultz et 170 al., 2006) for gaseous species and from the GOCART model (Global zone Chemistry Aerosol Radiation and Transport; Ginoux et al., 2001) for aerosols (desert dust, carbonaceous species and sulfate). The gas phase chemical mechanism is MELCHIOR2 (Modele Lagrangien de Chimie de l'Ozone a l'échelle Regionale), in which the NMVOC emissions are split into 10 species (C2H6, NC4H10, C2H4, C3H6, C5H8, OXYL, HCHO, CH3CHO, CH3COE and APINEN) and describe approximately 120 reactions. For semivolatile inorganic species (sulfate, nitrate, and ammonium), the equilibrium concentration is calculated



175 using the thermodynamic model ISORROPIA (Nenes et al., 1998). Nine vertical levels are selected with a first layer height at  
20 m to 25 m. Sea salt emissions were calculated as described in Monahan, 1986. MEGAN Model v2.04 calculated biogenic  
emissions separately (Guenther et al., 2006), which were then included in the land-based emissions  
For this study, a first domain with a 36 km resolution at the European scale was defined. A second domain was nested within,  
named MEDI12 (147 x 249 points), and covered the center of Europe with a resolution of 12 km. Both meteorological and  
180 chemical transport simulations were provided for these domains.

### 2.1.3 Model description CMAQ

The CMAQ Model v5.2 with the aero6 model calculates on the basis of emission input data air concentration as well as  
deposition fluxes of atmospheric gases and aerosols (Byun and Schere, 2006; Appel et al., 2017). Atmospheric chemistry is  
used by the Carbon Bond V mechanism (Yarwood et al., 2005) cb05tucl with updated toluene chemistry (Whitten et al., 2010),  
185 including the chlorine chemistry extension (CB05-TUCL;  
[https://www.airqualitymodeling.org/index.php/CMAQv5.0\\_Chemistry\\_Notes](https://www.airqualitymodeling.org/index.php/CMAQv5.0_Chemistry_Notes), accessed May 2021). The aerosol scheme  
AERO6 is used for the formation of secondary inorganic aerosols. Sulfuric acid (H<sub>2</sub>SO<sub>4</sub>), nitric acid (HNO<sub>3</sub>), hydrochloric  
acid (HCl) and ammonia (NH<sub>3</sub>) gas phase – aerosol partition equilibrium is solved by the ISORROPIA mechanism (Fountoukis  
and Nenes, 2007; Nenes et al., 1998). Contained within is the formation of secondary organic aerosol (SOA) from isoprene,  
190 terpenes, benzene, toluene, xylene and alkanes (Carlton et al., 2010; Pye and Pouliot, 2012).

Sea salt emissions were calculated as described in Kelly et al. (2010). Biogenic emissions (NMVOC from vegetation and soil  
NO) were calculated separately with the MEGAN Model v3 (Model of Emissions of Gases and Aerosols from Nature;  
Guenther et al., 2012). Emissions of windblown dust were not considered. CMAQ Models 30 vertical layers, with the lowest  
layer from 0 m to 42 m and the second layer from 42 m to 85 m.

195 The COSMO model simulated the meteorological data for CMAQ, applying the version COSMO5-CLM16 (Schultze and  
Rockel, 2018; Petrik et al., 2021). The MCIP (Meteorology-Chemistry Interface Processor) processed meteorological model  
output into the input format required for CMAQ. The vertical resolution of the meteorological model output was 40 terrain-  
following geometric height levels up to 22 km. The Boundary Condition driver used was IFS-CAMS cycle45r1 (Integrated  
Forecasting System – Copernicus Atmosphere Monitoring Service; Inness et al., 2019) with a vertical resolution of 60 sigma  
200 levels up to 65 km.

To prevent the effects from initial conditions on the simulated atmospheric concentrations in 2015, the model run started with  
a spin up run in mid-December 2014. The grid size of the Mediterranean Sea domain was 12 x 12 km<sup>2</sup>, nested in a 36 x 36 km<sup>2</sup>  
domain covering all of Europe.

### 2.1.4 Model description EMEP

205 The EMEP MSC-W (European Monitoring and Evaluation Programme, Meteorological Synthesizing Centre – West,  
<https://www.emep.int/mscw/index.html>, assessed June 2021) model is a limited area, terrain-following hybrid coordinate



model designed to calculate air concentrations and deposition fields for major acidifying and eutrophying pollutants, photooxidants and particulate matter (Simpson et al., 2012; Simpson et al., 2020).

210 In this study, a  $0.1^\circ \times 0.1^\circ$  resolution grid on long–lat projection and with 20 vertical levels was used. The meteorological input data are based on forecast experiment runs with the Integrated Forecast System (IFS), a global operational forecasting model from the European Centre for Medium-Range Weather Forecasts (ECMWF). The meteorological fields are retrieved on  $0.1^\circ \times 0.1^\circ$  long–lat coordinates. Vertically, the fields on 60 eta ( $\eta$ ) levels from the IFS model are interpolated onto the 20 EMEP eta levels.

215 The model version used was rv4.34 with chemical mechanism EmChem 19a (Simpson et al., 2012; Simpson et al., 2020). The mechanism builds on surrogate VOC species (Simpson et al., 2012; extended with benzene and toluene) and has 171 gas phase and heterogeneous reactions. The model always assumes equilibrium between the gas and aerosol phases using the MARS equilibrium module (Model for an Aerosol Reacting System) of Binkowski and Shankar (1995). For secondary organic aerosol (SOA), a so-called volatility basis set (VBS) approach (Robinson et al., 2007; Donahue et al., 2009; Bergström et al., 2012) is used. All primary organic aerosol (POA) emissions are treated as nonvolatile to keep emission totals of both PM and VOC  
220 components the same as in the official emission inventories, while the semivolatile ASOA and BSOA species are assumed to oxidize (age) in the atmosphere by OH reactions (Simpson et al., 2012).

The following natural emissions are calculated in the model for each grid cell and at every model time step: Biogenic emissions of isoprene and monoterpenes use near-surface air temperature and photosynthetically active radiation. Soil NO emissions from soils of seminatural ecosystems are specified as a function of N deposition and temperature. The generation of sea salt  
225 aerosol over oceans is driven by the surface wind, and the EMEP model’s parameterization scheme for calculating sea salt generation is based on two source functions, those of Monahan et al. (1986) and Mårtensson et al. (2003). The key parameter driving dust emissions is wind friction velocity. Additionally, daily emissions from forest and vegetation fires are taken from the “Fire INventory from NCAR version 1.0” (FINNv1; Wiedinmyer et al., 2011). For this study, the initial and boundary conditions provided with the open source model distribution for 2015 were used.

### 230 2.1.5 Model description LOTOS-EUROS

LOTOS-EUROS is a Eulerian chemistry transport model (Manders et al., 2017). The model simulates air pollution in the lower troposphere and is of intermediate complexity, allowing ensemble-based simulations and assimilation studies. LOTOS-EUROS performs hourly calculations using ECMWF (European Centre for Medium-Range Weather Forecasts) meteorological data. The gas phase chemistry follows the TNO CBM-IV scheme (Schaap et al., 2008). The dry deposition fluxes are calculated  
235 with the Deposition of Acidifying Compounds (DEPAC) 3.11 module, following the resistance approach, which includes a calculation of bidirectional  $\text{NH}_3$  fluxes (van Zanten et al., 2010; Wichink Kruit et al., 2012). The wet deposition fluxes are computed using the CAMx approach, which includes both in-cloud and below-cloud scavenging (Banzhaf et al., 2012). LOTOS-EUROS has a dynamical vertical layer structure with 5 layers in total. The first layer is at 25 m, while the second layer follows the meteorological boundary layer. On top of that, up to 3500 m and one top layer up to 5000 m above sea level





240 two evenly distributed reservoir layers are defined. The model has participated in multiple model intercomparison studies  
(Bessagnet et al., 2016; Colette et al., 2017), showing overall good performance.

## 2.2 Model Domains and Nesting

245 The domain for the intercomparison of the western part of the Mediterranean Sea covered a spatial extent from longitude:  
-1.0° to 31.2° and latitude: 32.8° to 46.8°. The grid cell size used was 12 x 12 km<sup>2</sup> interpolated on a 0.1° x 0.1° grid nested in  
a larger 36 x 36 km<sup>2</sup> grid (except EMEP) covering all of Europe, as shown in Figure 1.



**Figure 1: Domains and measurement stations. Red trapeze displays the 12 x 12 km<sup>2</sup> domain, black triangles are locations of measurement stations. On bottom left the larger 36 x 36 km<sup>2</sup> domain is displayed.**



## 2.3 Emissions

### 2.3.1 Land-based Emissions

250 Annual anthropogenic land-based gridded emissions for 2015 obtained from the CAMS-REG v2.2 emission inventory were used as input by all five compared models. Gridded emission files contain GNFR (Gridded Nomenclature for Reporting) emission sectors for each country for the air pollutants NO<sub>x</sub>, SO<sub>2</sub>, NMVOC, NH<sub>3</sub>, CO, PM<sub>10</sub>, PM<sub>2.5</sub>, and CH<sub>4</sub>. The emissions are provided at a spatial resolution of 1/10° x 1/20° in longitude and latitude (i.e., ~ 6 x 6 km over central Europe).

The height distribution of emissions per GNFR sector was determined as described in Bieser et al. (2011b). The temporal distribution was determined by separating the annual emissions of each sector into hourly emission data with data splitting as described in Granier et al. (2019). PM was split as described in Bieser et al. (2011a), NO<sub>x</sub> was split according to Manders-Groot et al. (2016), and NMVOC split was used as provided for the CAMS-REG v2.2 emission inventory (Granier et al., 2019).

### 2.3.1 Shipping Emissions

260 The shipping emission dataset produced with the STEAM model has a spatial resolution of 12 x 12 km<sup>2</sup> and a temporal resolution of 1 hour. The STEAM emissions are divided into two vertical layers (0 m to 36 m; 36 m to 1000 m) and are provided for mineral ash, carbon monoxide (CO), carbon dioxide (CO<sub>2</sub>), elemental carbon (EC), NO<sub>x</sub>, organic carbon (OC), PM<sub>2.5</sub>, particle number count (PNC), sulfate (SO<sub>4</sub>), SO<sub>x</sub> (containing SO<sub>2</sub> and SO<sub>3</sub>) and VOC. To reduce the number of generated emission maps and the computational resources needed to run the STEAM model, VOC emissions were divided into four categories according to their properties as a function of the engine load. Emission factors for VOC are based on the average values taken from various publications (Agrawal et al., 2008; Agrawal et al., 2010; Sippula et al., 2014; Reichle et al., 2015).

In CAMx, all shipping emissions are put in the first layer. For CHIMERE, all shipping emissions above 36 m and 88 % of the emissions below 36 m have been added to the second layer. Only 12 % of the emissions below 36 m were emitted in the first layer of the model. This was calculated based on the STEAM emission dataset and therein contained stack heights. Additionally, in CMAQ, shipping emissions were distributed in the two lowest layers, emissions below 36 m were attributed to the lowest layer, and emissions above 36 m were in the second layer. For EMEP simulations, the STEAM emissions were summed from hourly to daily emissions and attributed to the lowest layer (up to 90 m). In LOTOS-EUROS, emissions below 36 m are assigned ~ 70 % to the first layer, which is 25 m thick, and ~ 30 % to the second layer. Emissions above 36 m are divided over different height classes 30 % between 36 m and 90 m, 30 % between 90 m and 170 m, 30 % between 170 m to 310 m and 10 % between 310 cm and 470 m. Due to the dynamic second model layer (following the meteorological boundary layer), those emissions are put in the second and/or third model layer. In the case of a well-mixed and vertically extended meteorological boundary layer (above 470 m), all emissions are in this second layer, whereas when the boundary layer is shallow, some emissions are put in the third layer.



## 2.4 Deposition Mechanisms

280 Deposition velocities for gaseous species in CHIMERE, CMAQ and LOTOS-EUROS are based on the formula introduced by  
Wesely (1989). This formula is the reciprocal sum of aerodynamic resistance ( $R_a$ ), quasi-laminar sublayer resistance ( $R_b$ ) and  
surface resistance ( $R_c$ ). Nevertheless, all models differ in calculating the single variables.  $R_a$  depends on meteorology and  
surface roughness, which is model dependent.  $R_b$  is determined by the friction velocity, depending on the surface type.  $R_c$  is  
the bulk surface resistance, containing different components, i.e., leaf stomata, soil, leaf litter, etc. All of these components  
285 use input data that are unique for each model.

In CHIMERE,  $R_b$  is estimated following Hicks et al. (1987). The resistance  $R_c$  formulation follows Erisman et al. (1994) and  
the developments made in the EMEP model (Emberson et al., 2000; Simpson et al., 2003; Simpson et al., 2012). It uses a  
variety of additional resistances, mostly to account for stomatal and surface processes, both of which are depending on the  
land use type and season. In CMAQ, the m3dry mechanism was used, which takes  $R_a$  and  $R_b$  from the provided meteorological  
290 data.  $R_c$  is calculated in CMAQ as described in Pleim and Ran (2011). The resistance  $R_b$  in LOTOS-EUROS is described  
following the EDACS system (Erisman et al., 1994). In van Zanten et al. (2010), the parametrizations of different resistances  
 $R_c$  that contribute to resistance for dry deposition of  $\text{NO}_2$  and  $\text{O}_3$  are described, depending on land use type.

CAMx uses the gas resistance model of Zhang et al. (2003), which is very similar to the Wesely formulations with regard to  
 $R_a$  and  $R_b$ . However, the  $R_c$  is expressed as several more serial and parallel resistances, based on Wesely (1989) but with some  
295 adjustments within CAMx (Ramboll Environment and Health, 2020).

EMEP deposition mechanisms are not described here, as EMEP does not deliver separate  $\text{NO}_2$  and  $\text{O}_3$  deposition files and will  
not be considered in Sect. 3.4.

## 2.5 Observational Data/Statistical Analysis/Analysis of Model Results

Model results for total surface concentrations of  $\text{NO}_2$  and  $\text{O}_3$  from the five CTMs are evaluated against available measurements  
300 of the air quality monitoring network taken from the download service of Air quality of the European Environment Agency  
EEA (<https://discomap.eea.europa.eu/map/fme/AirQualityExport.htm>, 2021).  $\text{NO}_2$  concentrations are monitored at 67 and  $\text{O}_3$   
at 53 background stations. Figure 1 shows the locations of the measurement stations, and detailed information on the stations  
is given in Appendix B.

The criteria for the selection of the stations were i) station type is “background”, ii) elevation is below 1000 m and iii) data for  
305 more than one of the pollutants  $\text{NO}_2$ ,  $\text{O}_3$  or  $\text{PM}_{2.5}$  are available. The latter was chosen for further comparison in this  
intercomparison project. Preferably, stations close to the sea were chosen since modeling ship contributions were the major  
focus of this study. Furthermore, the domain was divided into four parts (“west”, “north”, “south”, “east”), and a roughly equal  
number of stations should be in each parcel (map in Supplements Figure S1). The measured concentrations at the stations were  
compared against the output of the CTMs. For this purpose, the grid cell of the respective monitoring station was determined,  
310 and modeled concentrations were taken from there.



To quantify the model performance, the root mean square error of the modeled values (RMSE), normalized mean bias (NMB) and Spearman's correlation coefficient (R) were calculated for each monitoring station, as described in Appendix A. A categorization for correlation was performed as described in Schober et al. (2018), adjusted and displayed in Table 2.

315 **Table 2: Interpretation of the correlation coefficient, as described in Schober et al (2018), adjusted.**

<b>Magnitude of Correlation Coefficient</b>	<b>Interpretation</b>
<b>0.00–0.39</b>	Weak correlation
<b>0.40–0.69</b>	Moderate correlation
<b>0.70–1.00</b>	Strong correlation

Time series were used to compare the modeled daily mean concentrations to observations at exemplary stations. In addition, the annual mean ship contribution was calculated based on hourly data. For a graphical comparison of the model performances R, NMB and RMSE, boxplots were used based on annual values calculated from hourly data at each station. For the  
320 intercomparison maps, annual mean values based on the hourly data are used. The correlation R between models was calculated for each grid cell based on hourly data.



### 3 Results and Discussion

In the following section, the results for NO<sub>2</sub> and O<sub>3</sub> model performance and spatial distribution will be shown. Afterward, O<sub>x</sub> and NO<sub>x</sub> will be displayed for a more detailed investigation of the photochemistry and lifetime of the species. The results of dry deposition of NO<sub>2</sub> and O<sub>3</sub> will be considered in Sect. 3.4.

#### 3.1 Model Performance and Intercomparison

To evaluate the performance of the models, modeled concentrations considering all emission sectors (base case) for annual values of 2015 were compared against actual measured data of NO<sub>2</sub> and O<sub>3</sub>. Based on the results of the five models for the cases with (base case) and without shipping emissions (noship case), contributions of the shipping sector to the NO<sub>2</sub> and O<sub>3</sub> concentrations were estimated. Maps display the annual mean values for 2015 and the relative ship contributions. With this setup, the model performance and ship contribution of the different models can be directly compared.

##### 3.1.1 NO<sub>2</sub> Model Performance

Table 2 contains R, NMB and RMSE based on the annual time series for NO<sub>2</sub> at all stations. The highest correlation across all 67 stations showed LOTOS-EUROS followed by CMAQ with a slightly lower correlation (LOTOS-EUROS: R = 0.45; CMAQ: R = 0.43), whereas for CHIMERE, EMEP and CAMx, an overall weak correlation was found (R = 0.06 to R = 0.09). The NMB suggests that all five CTMs underestimate the annual mean concentrations at most measurement sites; the NMB for all stations is negative for all models. The RMSE is within the same range for all models (RMSE = 15.6 µg/m<sup>3</sup> to 19.8 µg/m<sup>3</sup>; Table 2).

Time series for two example stations show the temporal variations between measured and modeled data. The supplements provide an overview of the mean values of stations in each map parcel (“west”, “north”, “south”, “east”; Supplement Figure S1). Figure 2 displays a time series at an urban background station in France (fr08614, “Gauzy”, latitude: 43.8344, longitude: 4.374219), which was chosen because southern France will be investigated in greater detail as part of this study. Figure 3 shows a rural background station in Italy (it1773a, “Genga – Parco Gola della Rossa”, latitude: 43.46806, longitude: 12.95222), which was chosen due to its central location in the domain and the high number of stations in Italy. Figure 4 displays the time series at a station in Greece (gr0035a, “Lykovrysi”, latitude: 38.06963, longitude: 23.77689) to include a station in the eastern part of the domain.

Measurements at the French station show the highest NO<sub>2</sub> values in winter, with peaks between 40 µg/m<sup>3</sup> and 55 µg/m<sup>3</sup> (Figure 2). LOTOS-EUROS and EMEP underestimate the values throughout the year. Moderate correlation was calculated for CMAQ (R = 0.6) and LOTOS-EUROS (R = 0.65) at this station. The modeled ship contribution has annual mean values from 0.2 µg/m<sup>3</sup> (EMEP, CAMx) to 0.6 µg/m<sup>3</sup> (CMAQ) at station fr08614. Shipping emissions have a relative contribution between 1.8 % (EMEP) and 6.7 % (CMAQ) to the total concentration in the annual mean. The highest ship contribution at this station was modeled by CMAQ. At the Italian station, 1773a lower NO<sub>2</sub> concentrations were measured compared to the station in France.



The highest peaks are approximately  $20 \mu\text{g}/\text{m}^3$  in winter. At station it1773a, the ship contribution to the total  $\text{NO}_2$  concentration has annual mean values between  $0.07 \mu\text{g}/\text{m}^3$  (LOTOS-EUROS) and  $0.5 \mu\text{g}/\text{m}^3$  (CAMx). The highest relative ship contribution was 7.9 % and was modeled by CAMx. At station gr0035a, the lowest simulated values are shown by CMAQ and LOTOS-EUROS. The highest values display EMEP at this station, also with the highest correlation between measured and modeled data ( $R = 0.55$ ). The ship contribution at the Greek station is between 5.0 % (EMEP) and 15.3 % (CAMx), which is higher than the ship contribution at the other two stations.

All models underestimate the actual measured total  $\text{NO}_2$  values at both stations, except for LOTOS-EUROS in Italy. None of the models are able to model matching peak values. Neither at the station in France, Italy or Greece models showed seasonal variation in concentrations, whereas  $\text{NO}_2$  usually has higher values in winter and lower values in summer, mainly because of lower photolytical degradation and suppressed vertical mixing, as described, i.e., in Ordóñez (2005).

Differences in ship contributions between the stations are caused by the location and station type (fr08614 = urban background; it1773a = rural background; gr0035a = suburban background). At the French station, the traffic-related  $\text{NO}_2$  concentration might supersede the ship-related  $\text{NO}_2$ . The station in Italy is not located in a city, so the  $\text{NO}_2$  concentration caused by ships comes to the fore. The highest ship contribution was simulated at the station in Greece because it is suburban but close to the Port of Piraeus, which is one of the largest ports in the Mediterranean Sea. As expected, the average ship contribution is low at stations that are not directly located at the coast or to a harbor.

To compare the correlation  $R$ , NMB and RMSE at all measurement stations for all models, the results of the comparison are divided by country and displayed in boxplots (Figure 5). Each dot displays one measurement station. The correlation measured against the modeled annual mean  $\text{NO}_2$  is highest for LOTOS-EUROS and CMAQ in all countries, reflecting the results shown in Table 3 for correlation. Nevertheless, boxplots for NMB and, in particular, for RMSE visualize that differences among countries are larger than differences among the models (Figure 5 b, c). This means that all models show good or bad performance at some stations, which was not found to be statistically relevant.

Underestimations by models of  $\text{NO}_2$  at urban sites were found in other studies (Karl et al., 2019a; Giordano et al., 2015), despite differences in grid size. Karl et al. (2019a) used a grid resolution of 4 km, and Giordano et al. (2015) used a grid resolution of  $\sim 0.25^\circ$  (27 km to 28 km). The underestimation might be due to too low emissions in the inventory used by the models and the heterogeneity of emissions. Regional models cannot display small-scale spatial heterogeneity; coarse grid cells are not representative of the measurement location. Giordano et al. (2015) suggested in their study that the underestimation of  $\text{NO}_2$  could be caused by either an underestimation of the chemical lifetime of  $\text{NO}_x$ , excessively high dry deposition, an underestimation of natural emissions at rural and remote stations or a combination of these factors. Differences in radical concentrations and reactive nitrogen might be additional reasons for underestimation (Knote et al., 2015).

The model performance of  $\text{NO}_2$  has shown that differences in time series between the models occur, caused by the large grid size and the differences in meteorology.



**Table 3: Correlation, normalized mean bias (NMB), root mean square error (RMSE), observational (obs) and modeled (mod) mean values of NO<sub>2</sub> for 2015: first data were averaged stationwise and then averaged for all 67 stations.**

	<b>Correlation R</b>	<b>NMB</b>	<b>RMSE (µg/m<sup>3</sup>)</b>	<b>mod (µg/m<sup>3</sup>)</b>	<b>obs (µg/m<sup>3</sup>)</b>
<b>CAMx</b>	0.06	-0.34	19.8	8.2	
<b>CHIMERE</b>	0.09	-0.54	19.0	5.7	
<b>CMAQ</b>	0.43	-0.56	17.6	6.9	17.2
<b>EMEP</b>	0.09	-0.42	19.3	7.1	
<b>LOTOS-EUROS</b>	0.45	-0.52	15.6	7.6	



390

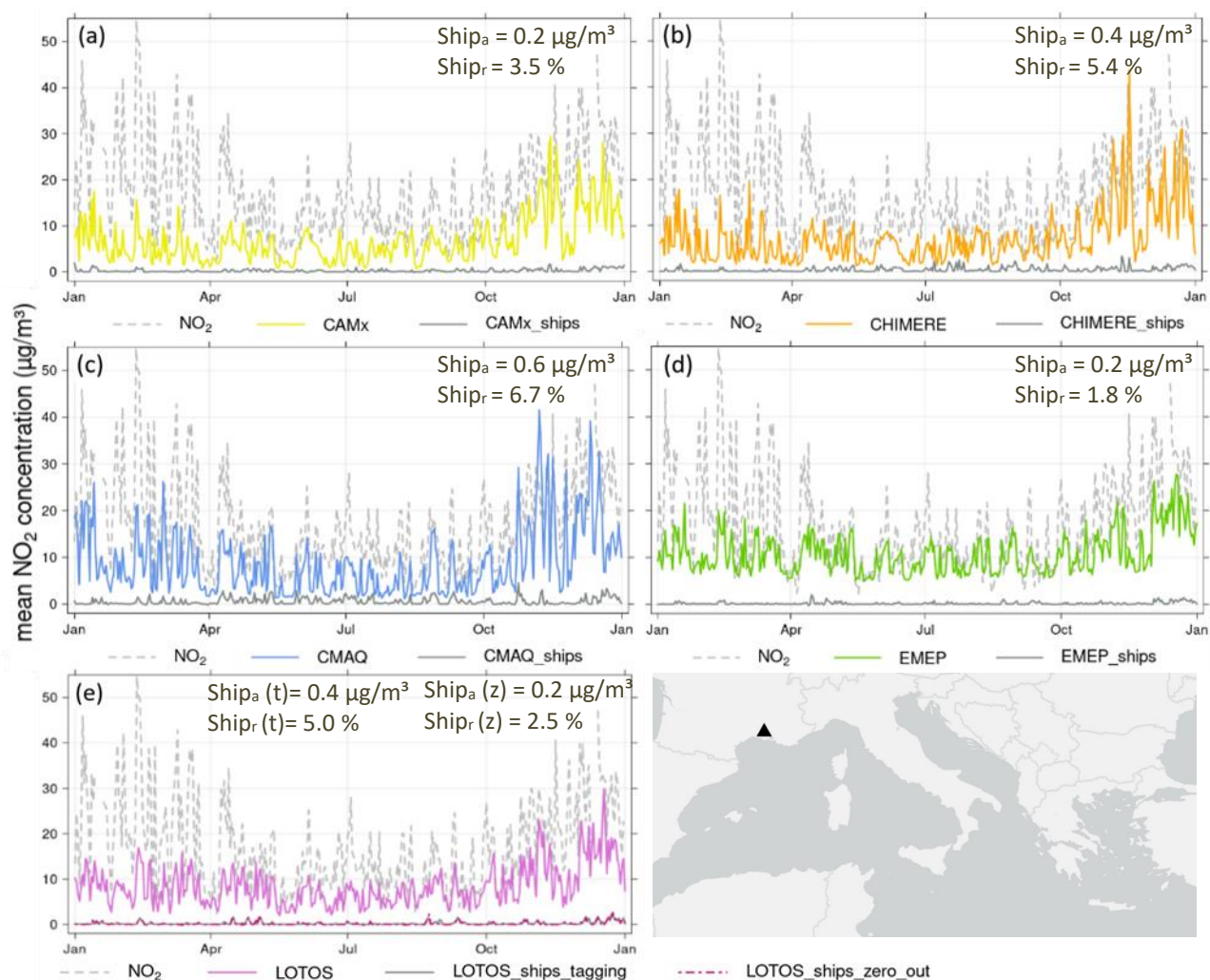


**Figure 2:** Time series with daily mean NO<sub>2</sub> concentrations in 2015 at station fr08614 in France. The black triangle on the map (bottom right) displays the location of the station. (a) = CAMx, (b) = CHIMERE, (c) = CMAQ, (d) = EMEP, (e) = LOTOS-EUROS. Dashed grey line = measured data, colored lines = modelled data, grey line = modelled ship contribution. Correlation between modelled and measured data for hourly total emission data for 2015: CAMx = 0.23, CHIMERE = 0.20, CMAQ = 0.60, EMEP = 0.02, LOTOS-EUROS = 0.65. Ship<sub>a</sub> displays absolute ship contribution, Ship<sub>r</sub> relative ship contribution of the respective model. (t) = tagging, (z) = zero-out method for LOTOS-EUROS.



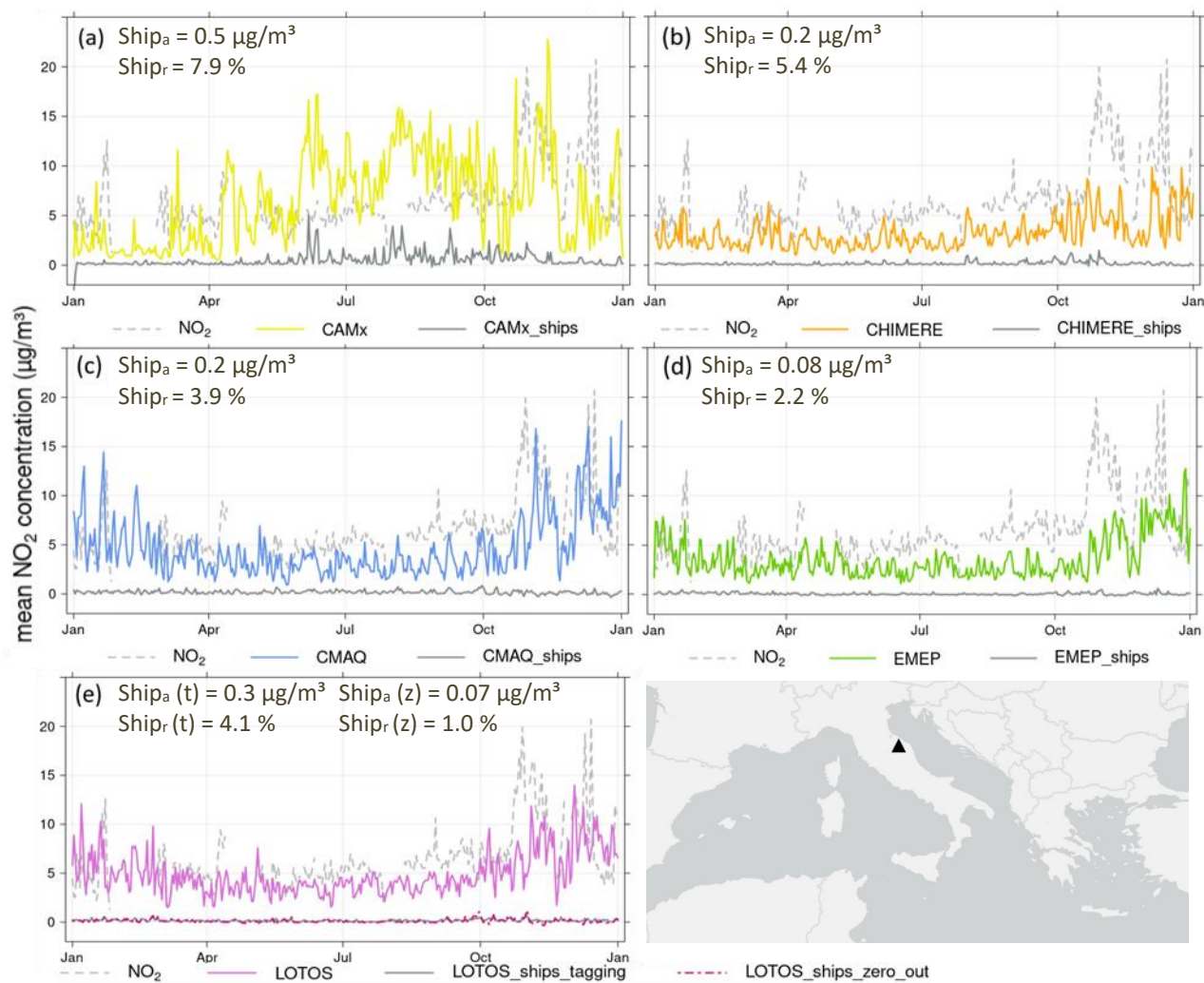


**Figure 3:** Time series with daily mean  $\text{NO}_2$  concentration in 2015 at station it1773a in Italy. The black triangle on the map (bottom right) displays the location of the station. (a) = CAMx, (b) = CHIMERE, (c) = CMAQ, (d) = EMEP, (e) = LOTOS-EUROS. Dashed grey line = measured data, colored lines = modelled data, grey line = modelled ship contribution. Correlation between modelled and measured data for hourly total emission data for 2015: CAMx = 0.03; CHIMERE = 0.03; CMAQ = 0.20; EMEP = -0.09; LOTOS-EUROS = 0.14 Ship<sub>a</sub> displays absolute ship contribution, Ship<sub>r</sub> relative ship contribution of the respective model. (t) = tagging, (z) = zero-out method for LOTOS-EUROS.

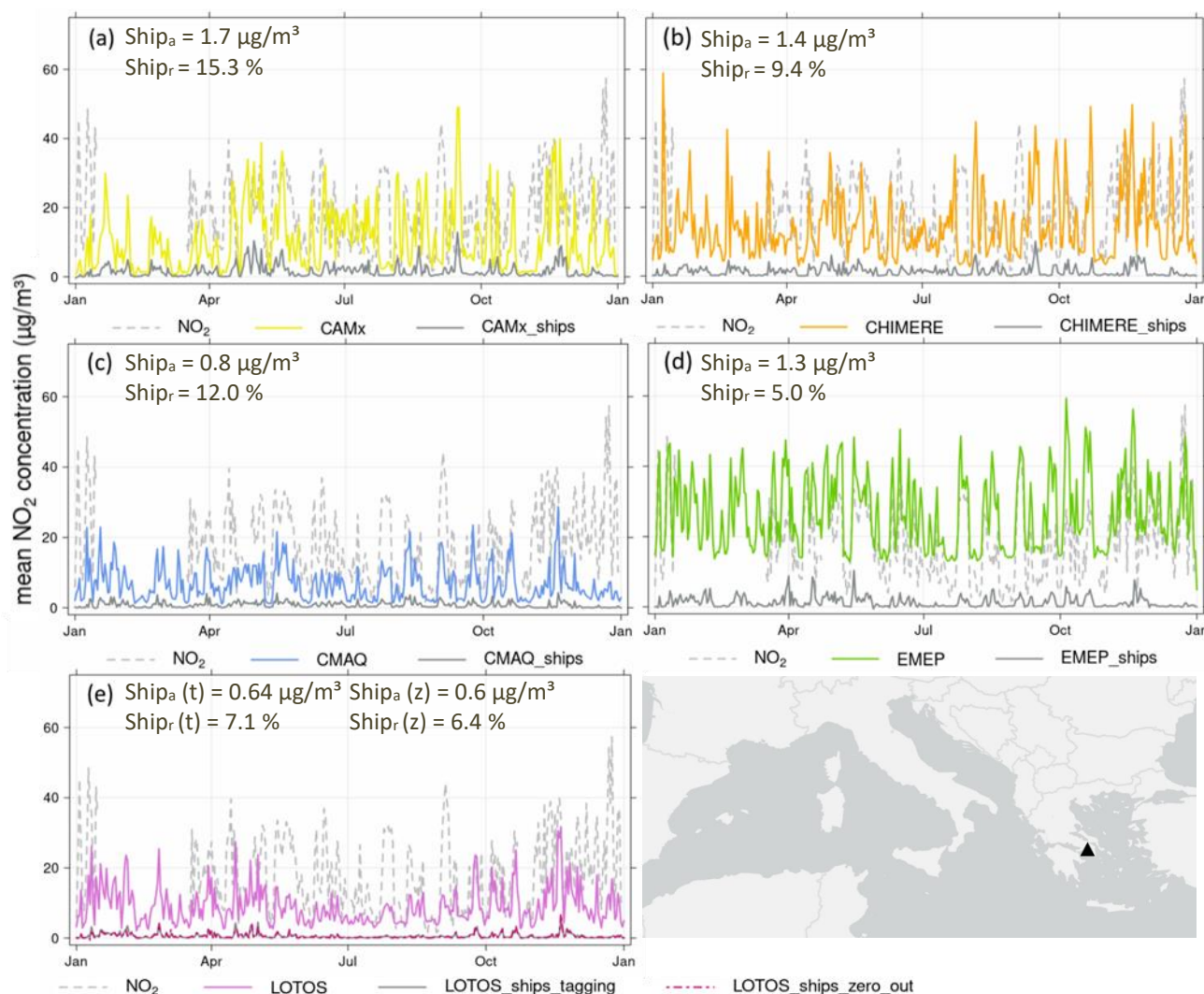


**Figure 4:** Time series with daily mean  $\text{NO}_2$  concentration in 2015 at station gr0035a in Greece. The black triangle on the map (bottom right) displays the location of the station. (a) = CAMx, (b) = CHIMERE, (c) = CMAQ, (d) = EMEP, (e) = LOTOS-EUROS. Dashed grey line = measured data, colored lines = modelled data, grey line = modelled ship contribution. Correlation between modelled and measured data for hourly total emission data for 2015: CAMx = 0.15; CHIMERE = 0.20; CMAQ = 0.28; EMEP = 0.55; LOTOS-EUROS = 0.38.  $\text{Ship}_a$  displays absolute ship contribution,  $\text{Ship}_r$  relative ship contribution of the respective model. (t) = tagging, (z) = zero-out method for LOTOS-EUROS.

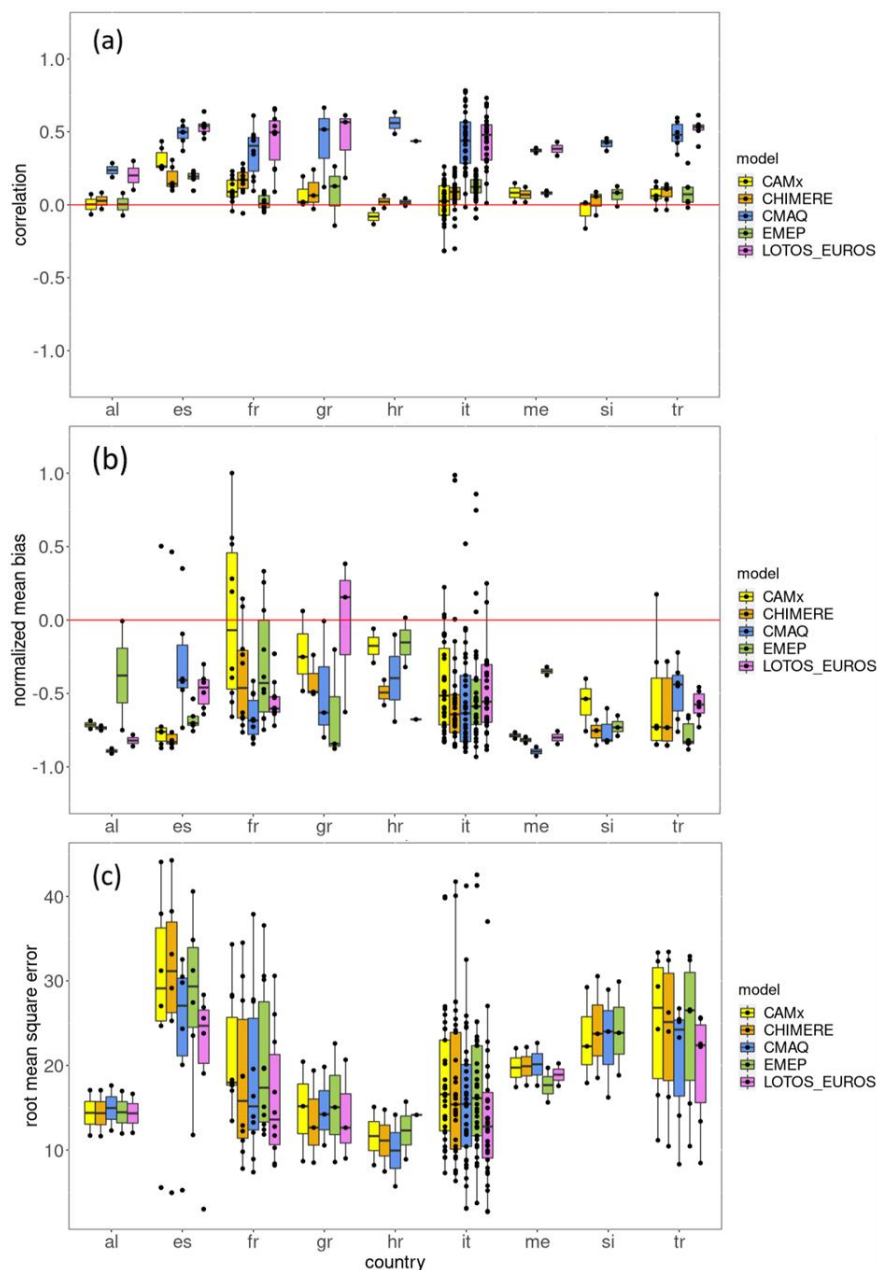


**Figure 5:** (a) = Correlation, (b) = NMB, (c) = RMSE for annual mean NO<sub>2</sub> concentration based on hourly data. Dots display annual mean values at measurement stations for the respective countries (al= Albania; es = Spain; fr =France; gr = Greece; hr = Croatia; it = Italy; me = Montenegro; si = Slovenia; tr = Turkey). Boxplots are for the models with the boxes displaying the interquartile range (IQR) between the 25<sup>th</sup> (Q1) and 75<sup>th</sup> (Q3) percentile, the black line displays the median (Q2), whiskers are calculated as  $Q1 - 1.5 * IQR$  (minimum) and  $Q3 + 1.5 * IQR$  (maximum).



### 3.1.2 NO<sub>2</sub> Spatial Distribution

395 The modeled annual mean NO<sub>2</sub> concentrations considering all emission sectors are similar for all models, with most values between 0 µg/m<sup>3</sup> and 2 µg/m<sup>3</sup> (Figure 7). CAMx and CHIMERE have the largest areas, with values exceeding 5 µg/m<sup>3</sup>, especially along the main shipping routes and in urban areas. The CMAQ, EMEP and LOTOS-EUROS maps look similar, which is in good agreement with the displayed time series in Sect. 3.1., where the results are within the same range.

Over land area, all model outputs display a concentration pattern ranging within one order of magnitude. Nevertheless, the  
400 frequency distributions of the CMAQ, EMEP and LOTOS-EUROS model outputs show the highest frequency between 0.5 µg/m<sup>3</sup> and 1.5 µg/m<sup>3</sup>, whereas for CAMx and CHIMERE, they are more equally distributed. Higher values of NO<sub>2</sub> concentrations simulated by CAMx and CHIMERE indicate a longer lifetime of NO<sub>2</sub> in the atmosphere. NO<sub>2</sub> reacts quickly with hydroxyl radicals (OH) and forms HNO<sub>3</sub>, or NO<sub>2</sub> photolysis creates O<sub>3</sub> during the daytime. The correlation between the models for total NO<sub>2</sub> concentration was calculate based on hourly data (Table 4). The highest correlation was found between  
405 CAMx and CHIMERE outputs (R = 0.80), but EMEP and CMAQ output were also within one range, demonstrating a strong correlation (R = 0.74). Weak correlations were found between LOTOS-EUROS and CAMx (R = 0.25) and LOTOS-EUROS and CHIMERE (R = 0.26). This weak correlation is due to the differences in frequency distribution, with LOTOS-EUROS showing most values below 1 µg/m<sup>3</sup>, whereas for CAMx and CHIMERE, more values are located in the higher value ranges. Overall, the models can give a robust estimate regarding the base run of the annual mean of NO<sub>2</sub>.

410 The highest contribution of ships to total NO<sub>2</sub> concentrations was found at the main shipping routes, with values > 85 % (Figure 8). Similar values were found for the Baltic Sea (Karl et al., 2019a) and for the Iberian Peninsula (Nunes et al., 2020). CHIMERE and CAMx model the highest values over the sea region, expecting a ship contribution to NO<sub>2</sub> between 60 % and 85 %. CMAQ, LOTOS-EUROS and EMEP have similar patterns for ship contributions over the sea.

On the Mediterranean coastline, CMAQ, CHIMERE, LOTOS-EUROS and EMEP simulate a similar contribution, with 25 %  
415 to 45 % ship contributions to total NO<sub>2</sub>. The CAMx model reveals a higher contribution with > 85 % at the coastline. The ship contribution displayed in the time series in Sect. 3.1 was lower, although the measurement stations were not far from the coast. This shows that although the contribution from ships reaches regions far from the coast, the highest impact is over the sea area. The frequency distribution for the relative ship contribution shows that all models simulate most values between 0 % and 5 % of the ship contribution. Interestingly, the distribution is lowest at values between  
420 20% and 40% (CMAQ, EMEP, LOTOS-EUROS) and 60 % (CAMx, CHIMERE) and then increases again at higher values, showing a bimodal distribution. This is due to large areas with high contributions over water and large areas with low contributions over land.

Over land in the northeast area of the domain, slightly negative ship contributions are derived from the CMAQ, CAMx, LOTOS-EUROS and EMEP model results. CHIMERE shows only very few negative values, but in the same region. Negative  
425 ship contributions to NO<sub>2</sub> concentrations may arise when the zero-out method is applied. They might be a consequence of the



nonlinear NO<sub>x</sub> gas phase chemistry. Especially in areas where the impact of NO<sub>x</sub> emissions from shipping is very low, less NO oxidation takes place because the additional NO from shipping in other areas already consumed the oxidants (e.g., O<sub>3</sub>). The boxplots in Figure 6 display the annual mean values for the whole model domain of NO<sub>2</sub>. Model outputs vary for the base run but also for the ship contribution output. This variability needs to be taken into account when the predictive power of models is considered. The “all\_mean” boxplot displays the mean of all models and displays that in comparison with other models, CAMx has high values. It further helps to show which models tend to simulate higher or lower values compared to others. The “all\_mean” boxplots show similar ranges as boxplots for CMAQ and EMEP, particularly regarding absolute and relative ship contributions. Additionally, models simulating a higher overall concentration of pollutants also tend to simulate a higher ship contribution. The relative ship contribution is highest for CAMx and CHIMERE and lowest for LOTOS-EUROS.

435

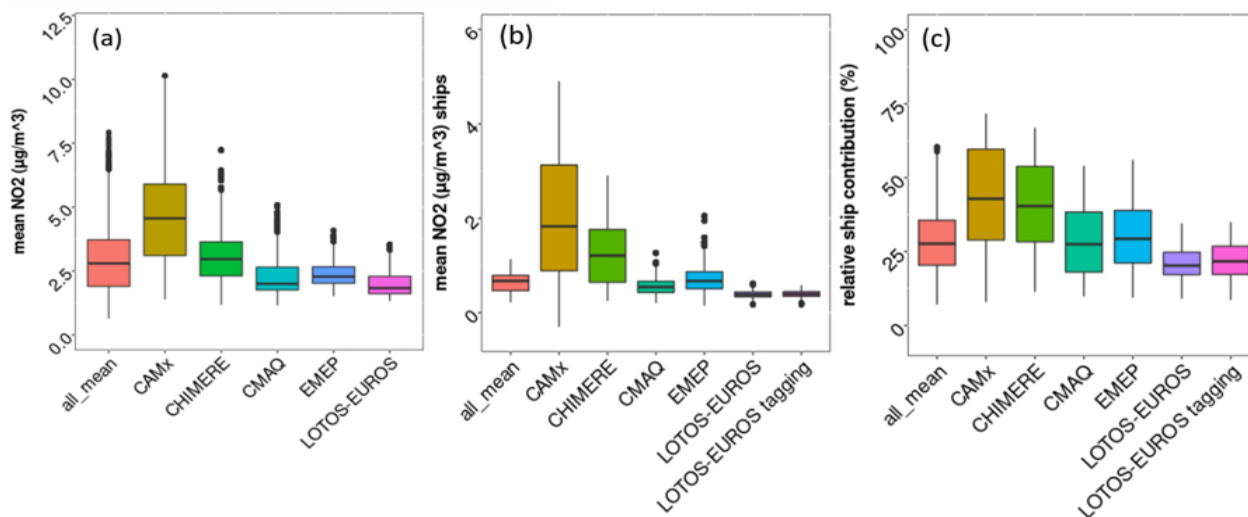
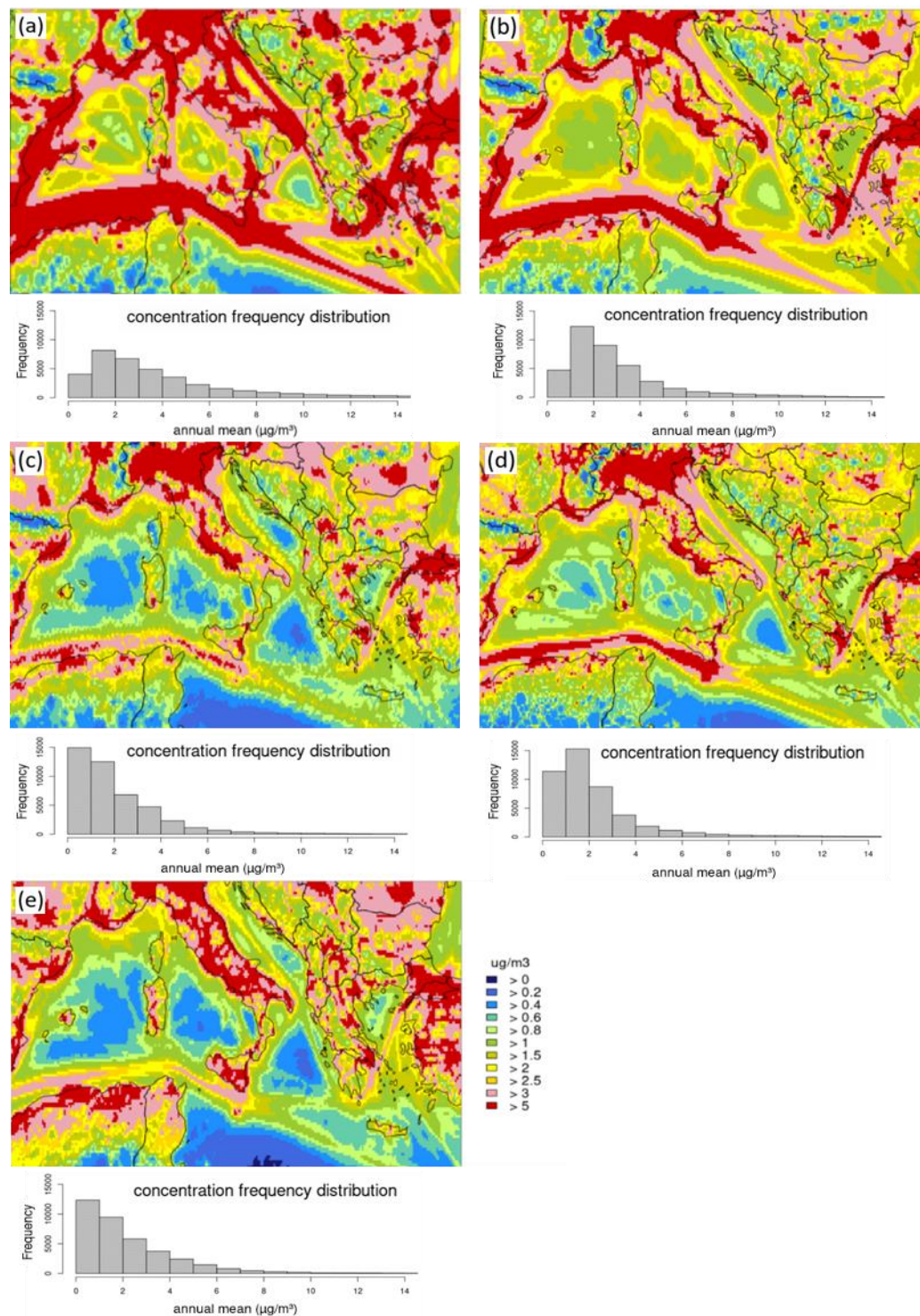


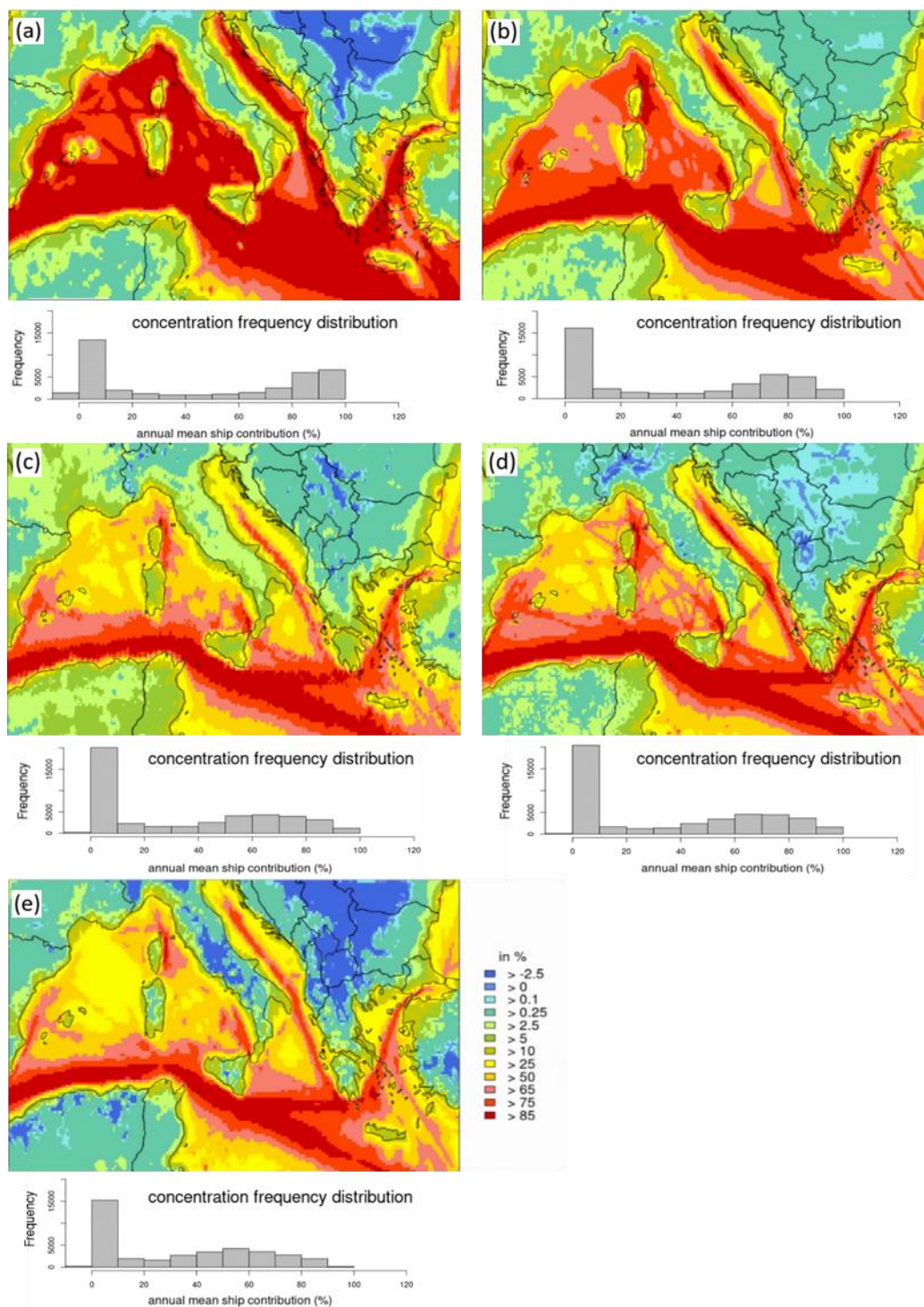
Figure 6: Annual mean for all grid cells in the whole model domain. (a) = mean NO<sub>2</sub> for all emission sectors (base case), (b) = mean NO<sub>2</sub> for shipping only, (c) = relative ship contribution to total NO<sub>2</sub> concentration. All\_mean is the mean value of all models, with a median of (a) = 2.8 µg/m<sup>3</sup>, (b) = 0.7 µg/m<sup>3</sup> and (c) = 27.7 µg/m<sup>3</sup>.

Table 4: Correlation for the NO<sub>2</sub> base run between models for the whole domain (all grid cells), based on hourly data for NO<sub>2</sub> total concentration.

all	CAMx	CHIMERE	CMAQ	EMEP	LOTOS-EUROS
LOTOS-EUROS	0.25	0.26	0.54	0.59	-
EMEP	0.40	0.44	0.74	-	-
CMAQ	0.40	0.44	-	-	-
CHIMERE	0.80	-	-	-	-
CAMx	-	-	-	-	-



**Figure 7: Annual mean NO<sub>2</sub> total concentration. (a) = CAMx, (b) = CHIMERE, (c) = CMAQ, (d) = EMEP, (e) = LOTOS-EUROS. Below the maps is the respective frequency distribution displayed for the annual mean NO<sub>2</sub> concentration, referred to the whole model domain.**



**Figure 8: Annual mean NO<sub>2</sub> ship contribution. (a) = CAMx, (b) = CHIMERE, (c) = CMAQ, (d) = EMEP, (e) = LOTOS-EUROS. Below the maps is the respective frequency distribution displayed for the annual mean NO<sub>2</sub> ship contribution, referred to the whole model domain.**



### 3.1.3 LOTOS-EUROS: zero-out vs. tagging

The LOTOS-EUROS model used two methods to calculate the ship contribution for  $\text{NO}_2$ . The range of values calculated with the zero-out method for ship contribution is larger compared to the tagging method, reaching from -2.5 % over land areas to 85 % at the main shipping lanes (Figure 9, a). By using the tagging method, ship contributions range from 0.2 % over land areas to 75 % at the main shipping lanes (Figure 9, b). The tagging method does not produce negative values. Regarding the overall output in boxplots (Figure 6), ship contribution for both methods is within the same range.

Although all models use relatively precise higher-order algorithms for chemical calculations, they still have a certain amount of numerical noise, causing over- or underestimation of certain emission sources when using the zero-out method (European Commission, Joint Research Centre et al., 2020; Brandt et al., 2013). The tagging method simulates the concentration for shipping as an emission source parallel with the background concentrations in the CTMs and is expected to be more accurate (Brandt et al., 2013). Thürkow et al. (2021) compared the tagging method against brute force simulations of  $\text{NO}_x$  with variable emission reduction percentages to study the nonlinearity. They concluded that the sector wise reductions in emissions would overestimate the base run concentration with all sectors for NO and underestimate  $\text{NO}_2$  concentrations when brute force simulations are carried out in comparison to tagging. Nevertheless, for  $\text{NO}_x$ , the differences were small. Small differences in  $\text{NO}_x$  ship contribution between the tagging and zero-out methods were also found in the present study (Figure 9 c, d).

However, the preference of the method that shall be used for quantifying the ship contribution also depends on the question that needs to be answered. Zero-out focuses on a situation that would appear when emissions from a certain source are shut off entirely, whereas the tagging method assigns a relative value to each source. In addition, for comparing the ship contribution output of different models, the zero-out method is the most common way to obtain a standardized output. For the comparison of model outputs with regard to the shipping contribution, zero-out is an adequate method. Furthermore, the tagging method used in the present study only traces emission-preserved atoms (i.e., carbon or nitrogen). Thus, it did not produce a source allocation for  $\text{O}_3$  in shipping emissions. Mertens et al. (2018) introduced an advanced tagging method for the contribution of land transport and shipping emissions to  $\text{O}_3$ , which is not yet included in LOTOS-EUROS, which can resolve the problem of lacking ship contributions to  $\text{O}_3$ . A sensitivity run with stepwise reduction of  $\text{NO}_x$  emissions for the zero-out method could hint at a possible shift in the atmospheric photochemical regime. However, this was not the focus of the present study.



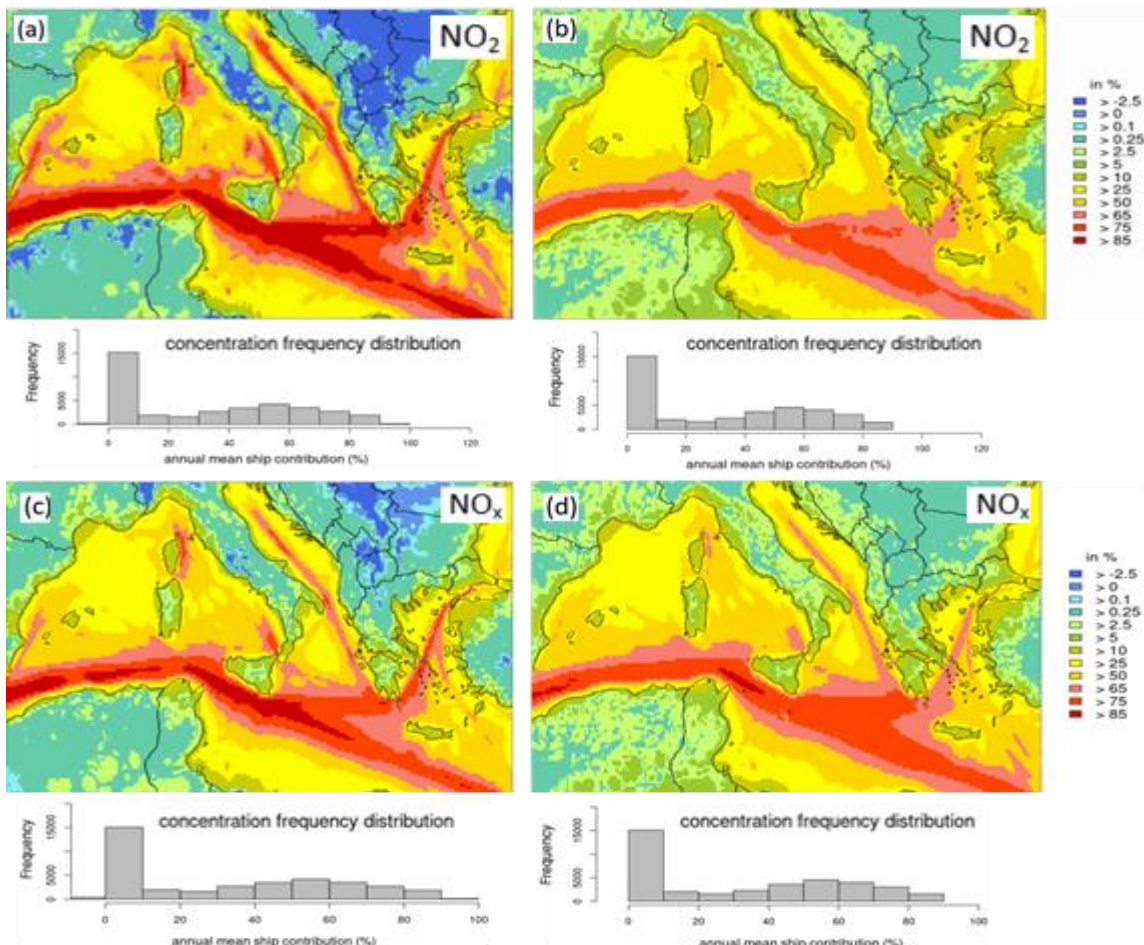


**Figure 9: Annual mean ship contribution for NO<sub>2</sub> (upper two maps) and NO<sub>x</sub> (lower two maps), calculated with LOTOS-EUROS (a) = zero-out method ship contribution NO<sub>2</sub>, (b) = tagging method ship contribution NO<sub>2</sub>, (c) = zero-out method ship contribution NO<sub>x</sub>, (d) = tagging method ship contribution NO<sub>x</sub>. Below the maps is the respective frequency distribution displayed for the annual mean NO<sub>2</sub> and NO<sub>x</sub> ship contribution, referred to the whole model domain.**



### 3.1.4 O<sub>3</sub> Model Performance

The tropospheric O<sub>3</sub> concentrations are strongly connected to the NO<sub>2</sub> concentration and to the oxidized nitrogen chemistry in the atmosphere. O<sub>3</sub> can be both an initiator and a product of photochemistry; thus, it is crucial in tropospheric chemistry.

Modeled versus measured data of one-year daily mean O<sub>3</sub> time series show a weak (EMEP: R = 0.38) to moderate correlation (CAMx: R = 0.40; CHIMERE: R = 0.48; CMAQ: R = 0.60; LOTOS-EUROS: R = 0.69; Table 5).

Selected time series represent these differences in correlation. Nevertheless, for the first months of the year CHIMERE, CAMx and CMAQ overestimate the actual measured O<sub>3</sub> values (Figure 10: station fr08614; Figure 11: station it1773a; Figure 12: gr0035a).

During summer months, O<sub>3</sub> shows the highest values due to increased photochemical activity. The modeled ship contribution is between 1.1 µg/m<sup>3</sup> (CAMx) and 2.8 µg/m<sup>3</sup> (LOTOS-EUROS) at station fr08614 and has a relative contribution between 1.3 % (CAMx) and 4.0 % (CHIMERE) to the total concentration. At station it1773a, the mean O<sub>3</sub> ship contribution is between 1.0 µg/m<sup>3</sup> (CAMx) and 3.0 µg/m<sup>3</sup> (CHIMERE), and the relative contribution ranges from 1.1 % (CAMx) to 3.5 % (LOTOS-EUROS). The ship contribution of station gr0035s ranges from -0.1 µg/m<sup>3</sup> (CAMx) to 3.7 µg/m<sup>3</sup> (CMAQ; LOTOS-EUROS), which is a relative contribution of -0.1 % (CAMx) and 3.7 % (CMAQ).

The O<sub>3</sub> ship contribution is within the same range at both stations and for all five models. Figure 13 shows that CMAQ has the smallest bias compared to the other models (NMB = 0.29), followed by LOTOS-EUROS (NMB = 0.36). The RMSE is lowest for CMAQ (RMSE = 32.0 µg/m<sup>3</sup>) and LOTOS-EUROS (RMSE = 32.6 µg/m<sup>3</sup>), along with the lower NMB compared to the other models. The performance analysis revealed that all five models predict higher O<sub>3</sub> concentrations than those measured at almost all stations (NMB > 0). The overestimation of actual measured O<sub>3</sub> by the models is in line with results from previous studies (Karl et al., 2019a; Appel et al., 2017; Im et al., 2015a; Im et al., 2015b). Im et al. (2015a) showed that O<sub>3</sub> concentrations above 140 µg/m<sup>3</sup> are underestimated, while concentrations below 50 µg/m<sup>3</sup> are overestimated by 40 % to 80 % in all considered models. This overestimation of O<sub>3</sub> by the models is likely linked to the chemical boundary conditions used in the regional CTMs. Analyses of the boundary conditions revealed that, especially in winter, O<sub>3</sub> levels are mostly driven by transport instead of local production due to limited photochemistry (Giordano et al., 2015).

CHIMERE uses boundary conditions from monthly mean climatologies simulated with the LMDz-INCA model, CAMx uses Mozart-4 output, LOTOS-EUROS and CMAQ use IFS-CAMS reanalysis data and the EMEP model uses ozone boundary conditions provided with the open source model distribution for 2015. These differences in input for the boundary conditions can be seen as the reason for the varying output in O<sub>3</sub>.

All models performed relatively well and are able to represent the course of the year, with higher values in summer and lower values in winter. Nevertheless, in some cases, the values in spring are overestimated.



500

**Table 5: Correlation, normalized mean bias (NMB), root mean square error (RMSE), observational (obs) and modeled (mod) of O<sub>3</sub> as the mean values for 2015: the first data were averaged stationwise and then averaged for all 53 stations.**

	<b>Correlation R</b>	<b>NMB</b>	<b>RMSE (<math>\mu\text{g}/\text{m}^3</math>)</b>	<b>mod (<math>\mu\text{g}/\text{m}^3</math>)</b>	<b>obs (<math>\mu\text{g}/\text{m}^3</math>)</b>
<b>CAMx</b>	0.40	0.45	41.8	90.6	
<b>CHIMERE</b>	0.48	0.62	47.0	101.2	
<b>CMAQ</b>	0.60	0.29	32.0	81.2	65.2
<b>EMEP</b>	0.38	0.42	40.4	87.9	
<b>LOTOS-EUROS</b>	0.69	0.36	32.6	87.7	

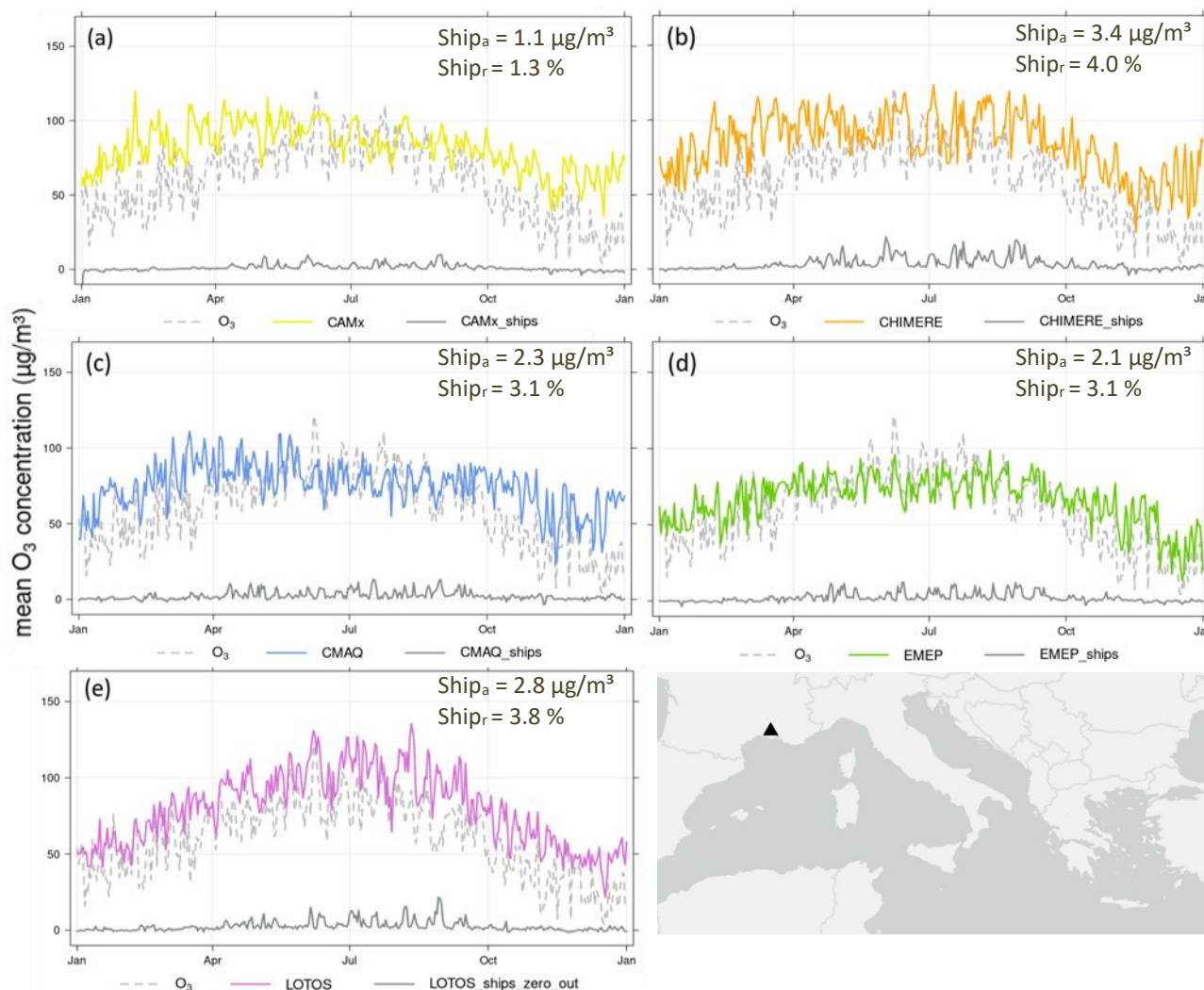


**Figure 10:** Time series with daily mean  $O_3$  concentration in 2015 at station fr08614 in France. The black triangle on the map (bottom right) displays the location of the station. (a) = CAMx, (b) = CHIMERE, (c) = CMAQ, (d) = EMEP, (e) = LOTOS-EUROS. Dashed gray line = measured data, colored lines = modeled data, gray line = modeled ship contribution. Correlation between modeled and measured data for hourly total emission data for 2015: CAMx= 0.57; CHIMERE = 0.6; CMAQ = 0.71; EMEP = 0.39; LOTOS-EUROS = 0.78. Ship<sub>a</sub> displays absolute ship contribution, Ship<sub>r</sub> relative ship contribution of the respective model.

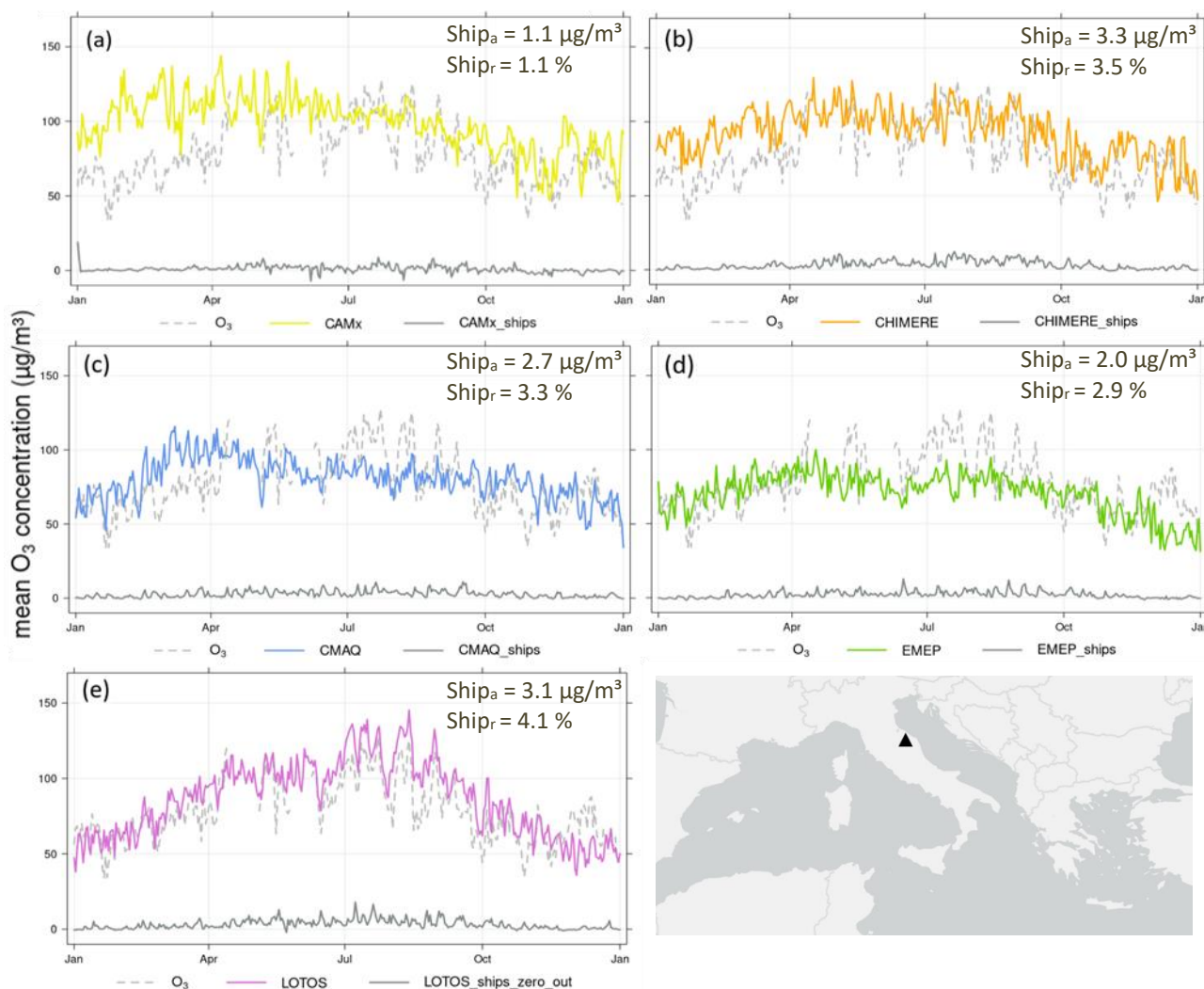


**Figure 11: Time series with daily mean  $O_3$  concentration in 2015 at station it1773a in Italy. The black triangle on the map (bottom right) displays the location of the station. (a) = CAMx, (b) = CHIMERE, (c) = CMAQ, (d) = EMEP, (e) = LOTOS-EUROS. Dashed gray line = measured data, colored lines = modeled data, gray line = modeled ship contribution. Correlation between modeled and measured data for hourly total emission data for 2015: CAMx = 0.37; CHIMERE = 0.4; CMAQ = 0.58; EMEP = 0.35; LOTOS-EUROS = 0.7.  $\text{Ship}_a$  displays absolute ship contribution,  $\text{Ship}_r$  relative ship contribution of the respective model.**

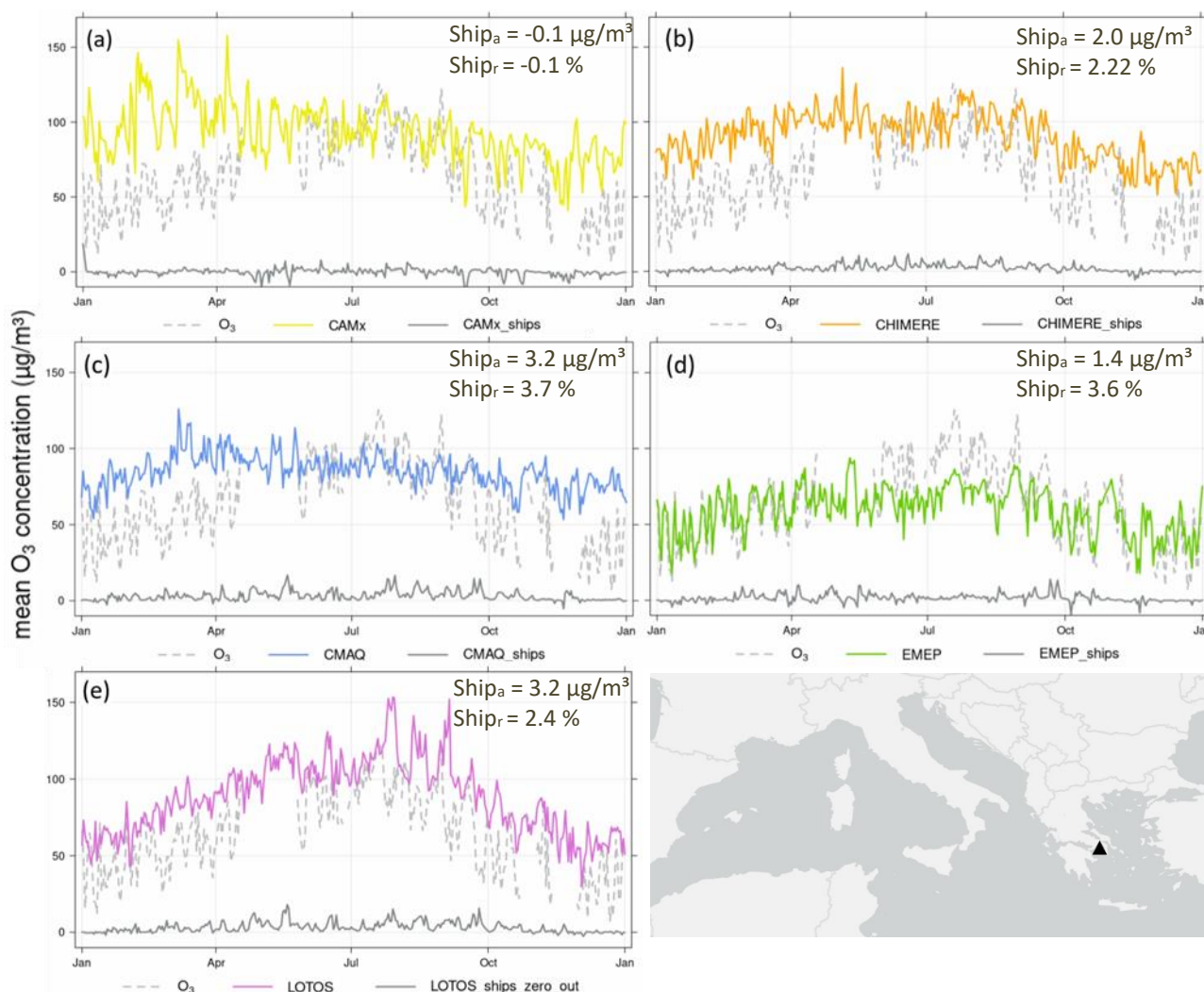


**Figure 12:** Time series with daily mean  $O_3$  concentration in 2015 at station gr0035a in Greece. The black triangle on the map (bottom right) displays the location of the station. (a) = CAMx, (b) = CHIMERE, (c) = CMAQ, (d) = EMEP, (e) = LOTOS-EUROS. Dashed gray line = measured data, colored lines = modeled data, gray line = modeled ship contribution. Correlation between modeled and measured data for hourly total emission data for 2015: CAMx = 0.29; CHIMERE = 0.46; CMAQ = 0.50; EMEP = 0.71; LOTOS-EUROS = 0.57. Ship<sub>a</sub> displays absolute ship contribution, Ship<sub>r</sub> relative ship contribution of the respective model.

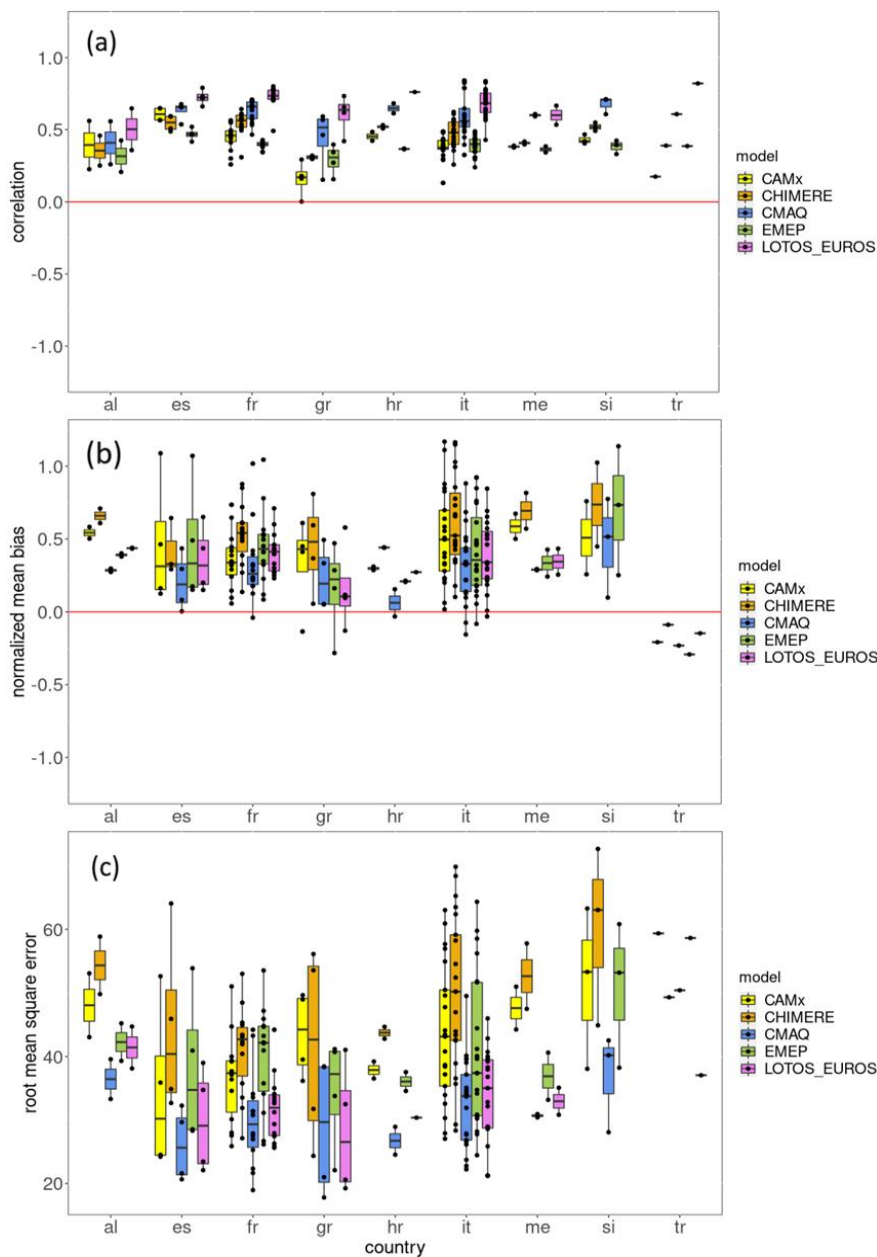


**Figure 13:** (a) = Correlation, (b) = NMB, (c) = RMSE for annual mean O<sub>3</sub> concentration. Dots display values at measurement stations for the respective countries (al= Albania; es = Spain; fr =France; gr = Greece; hr = Croatia; it = Italy; me = Montenegro; si = Slovenia; tr = Turkey). Boxplots are for the models with the boxes displaying the interquartile range (IQR) between the 25<sup>th</sup> (Q1) and 75<sup>th</sup> (Q3) percentile, the black line displays the median (Q2), whiskers are calculated as  $Q1 - 1.5 * IQR$  (minimum) and  $Q3 + 1.5 * IQR$  (maximum).



### 3.1.5 O<sub>3</sub> Spatial Distribution

The annual mean concentration of O<sub>3</sub> considering all emission sectors is between 60 µg/m<sup>3</sup> and 120 µg/m<sup>3</sup> for all models (Figure 15). This is consistent with the measurements displayed in the time series in Sect. 3.2.1. CHIMERE, CAMx and LOTOS-EUROS show particularly high O<sub>3</sub> concentrations over the sea. Interestingly, EMEP results are similarly high over the sea area, but in comparison with other models, concentrations are lower over land, and even values below 60 µg/m<sup>3</sup> can be seen in the Po valley (Figure 15, d). Regarding the correlation between the models for total concentration over the whole domain, it is highest between CMAQ and EMEP (R = 0.71) and lowest for CAMx and LOTOS-EUROS (R = 0.39), but predominantly moderate correlations were found among the models (Table 6).

In general, all models show high annual mean concentrations over the sea areas and low annual mean concentrations over land areas, which might be traced back to the emission input datasets that were split into land-based emissions and emissions from oceangoing ships. Furthermore, high values of O<sub>3</sub> are expected to enter the domain from the eastern part of the Mediterranean Sea. This point will be discussed in Sect. 4. The frequency distribution of the annual mean total concentration of O<sub>3</sub> has a bimodal distribution for CHIMERE, CMAQ and EMEP. This reflects photochemical O<sub>3</sub> depletion or production, with high values over water areas and lower values over land. Over water, low O<sub>3</sub> depletion is expected during the night. A comparison of diurnal cycles of O<sub>3</sub> over water and over land shows that this presumption is reflected by CMAQ and EMEP output, showing more pronounced cycles of O<sub>3</sub> in grid cells over land (Appendix C). However, the diurnal cycles of CAMx, CHIMERE and LOTOS-EUROS do not show differences in amplitude over land and water. Despite this, over water, all models show a higher spread of values within diurnal cycles, displaying that there is more variability in the course of the year over water than over land.

The relative contribution of ships to total O<sub>3</sub> concentrations is lowest in areas with a high contribution of shipping to total NO<sub>2</sub> (Figure 16). It decreases to -20 % in areas with high NO<sub>2</sub> concentrations in all model outputs, displaying a local scale titration of O<sub>3</sub> by NO, which is emitted by ships. This reverse relationship between NO<sub>2</sub> and O<sub>3</sub> was already shown in other studies (e.g., Karl et al., 2019b). Consequently, the largest areas with O<sub>3</sub> destruction for the CAMx and CHIMERE models coincide with areas where the models show the highest contribution of shipping to NO<sub>2</sub>. The comparison with the time series shows the highest ship contribution to the total O<sub>3</sub> concentration in summer. Likewise, in Sect. 3.1.4 lowest ship contribution was found for CAMx.

Figure 14 shows boxplots with annual mean values of the models for the whole domain. It shows that CAMx, CHIMERE and LOTOS-EUROS are within one range regarding the annual mean total concentration. The CMAQ and EMEP outputs are lowest for the annual mean O<sub>3</sub> total concentration. Regarding ship contribution, all models except CAMx are within one range. The present study does not contain the parts of the Mediterranean Sea furthest east due to the focus of the project on the western Mediterranean Sea with its harbor cities as well as due to the limited extent of the WRF domain. A more detailed investigation of the boundary conditions of CMAQ has shown high O<sub>3</sub> values in the eastern part of the domain. A high O<sub>3</sub> production over the eastern Mediterranean Sea and a steep west-east gradient of O<sub>3</sub> were described in previous studies (i.e., Doche et al., 2014;





Safieddine et al., 2014; Liu et al., 2009). This production influences the amount of O<sub>3</sub> in the western part of the Mediterranean Sea. Safieddine et al. (2014) found an increase of up to 22 % in O<sub>3</sub> in the eastern part of the Mediterranean basin compared to the middle of the basin. Doche et al. (2014) described a steep west–east O<sub>3</sub> gradient with the highest concentrations over the eastern part of the Mediterranean basin.

545 Overall, all models showed a relatively good performance for O<sub>3</sub> but differed in modeling spatial distribution and ship contribution mainly over water. Although boxplots for annual mean values of O<sub>3</sub> differ, for relative ship contribution they show that CHIMERE, CMAQ, EMEP and LOTOS-EUROS are within one range. Diurnal cycles did not reveal differences in O<sub>3</sub> depletion over water and land between the models.

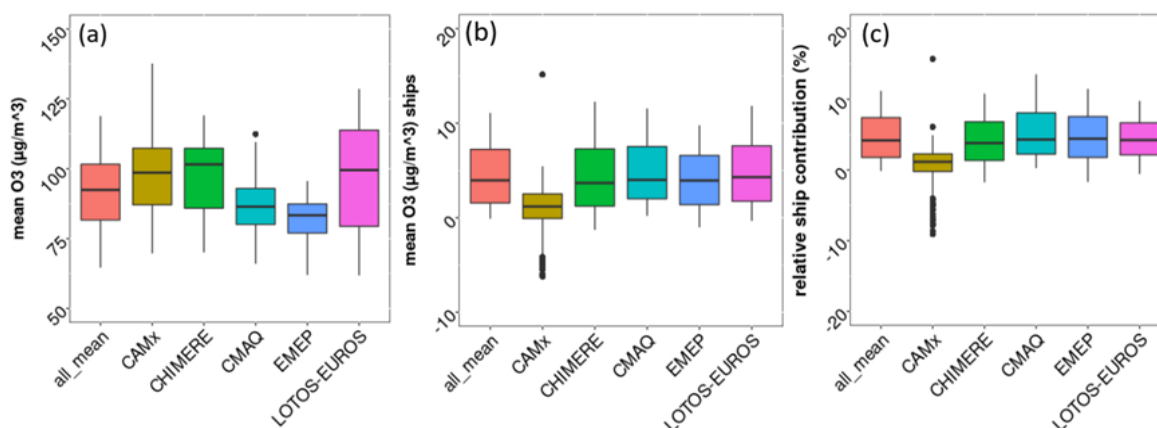
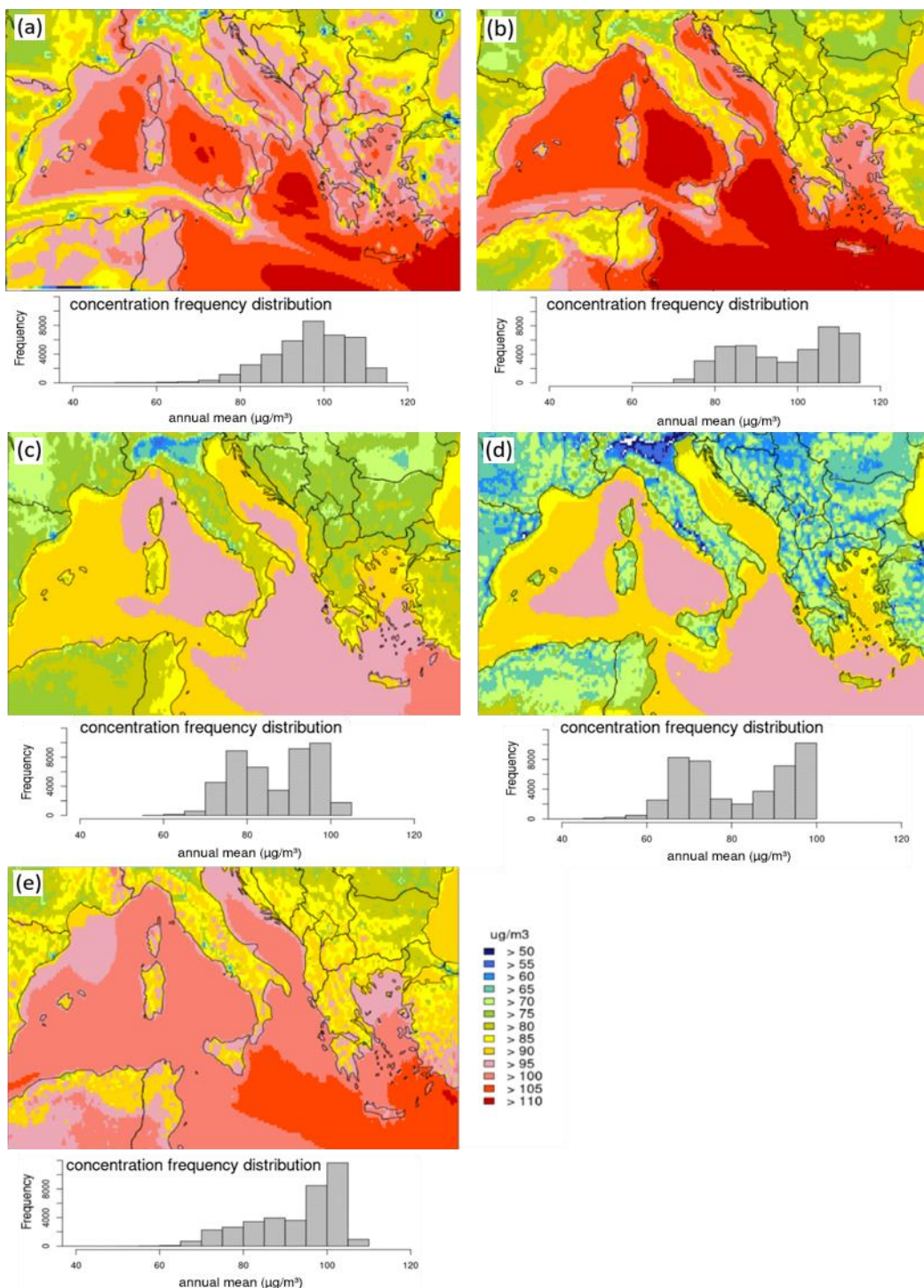


Figure 14: Annual mean for the whole model domain. (a) = mean O<sub>3</sub> for all emission sectors (base case), (b) = mean O<sub>3</sub> for shipping only, (c) = relative ship contribution to total O<sub>3</sub> concentration. All\_mean is the mean value of all models, with a median of (a) = 92.4 µg/m<sup>3</sup>, (b) = 4.0 µg/m<sup>3</sup> and (c) = 4.2 µg/m<sup>3</sup>.

550 Table 6: Correlation between models for the whole domain (all grid cells) based on hourly data for O<sub>3</sub> total concentration.

all	CAMx	CHIMERE	CMAQ	EMEP	LOTOS-EUROS
LOTOS-EUROS	0.39	0.56	0.49	0.55	-
EMEP	0.44	0.58	0.71	-	
CMAQ	0.50	0.56	-		
CHIMERE	0.63	-			
CAMx	-				



**Figure 15: Annual mean O<sub>3</sub> total concentration. (a) = CAMx, (b) = CHIMERE, (c) = CMAQ, (d) = EMEP, (e) = LOTOS-EUROS; emisbase maps, annual mean value, white areas contain values below 60 µg/m<sup>3</sup>. Below the maps is the respective frequency distribution displayed for the annual mean O<sub>3</sub> concentration, referred to the whole model domain.**

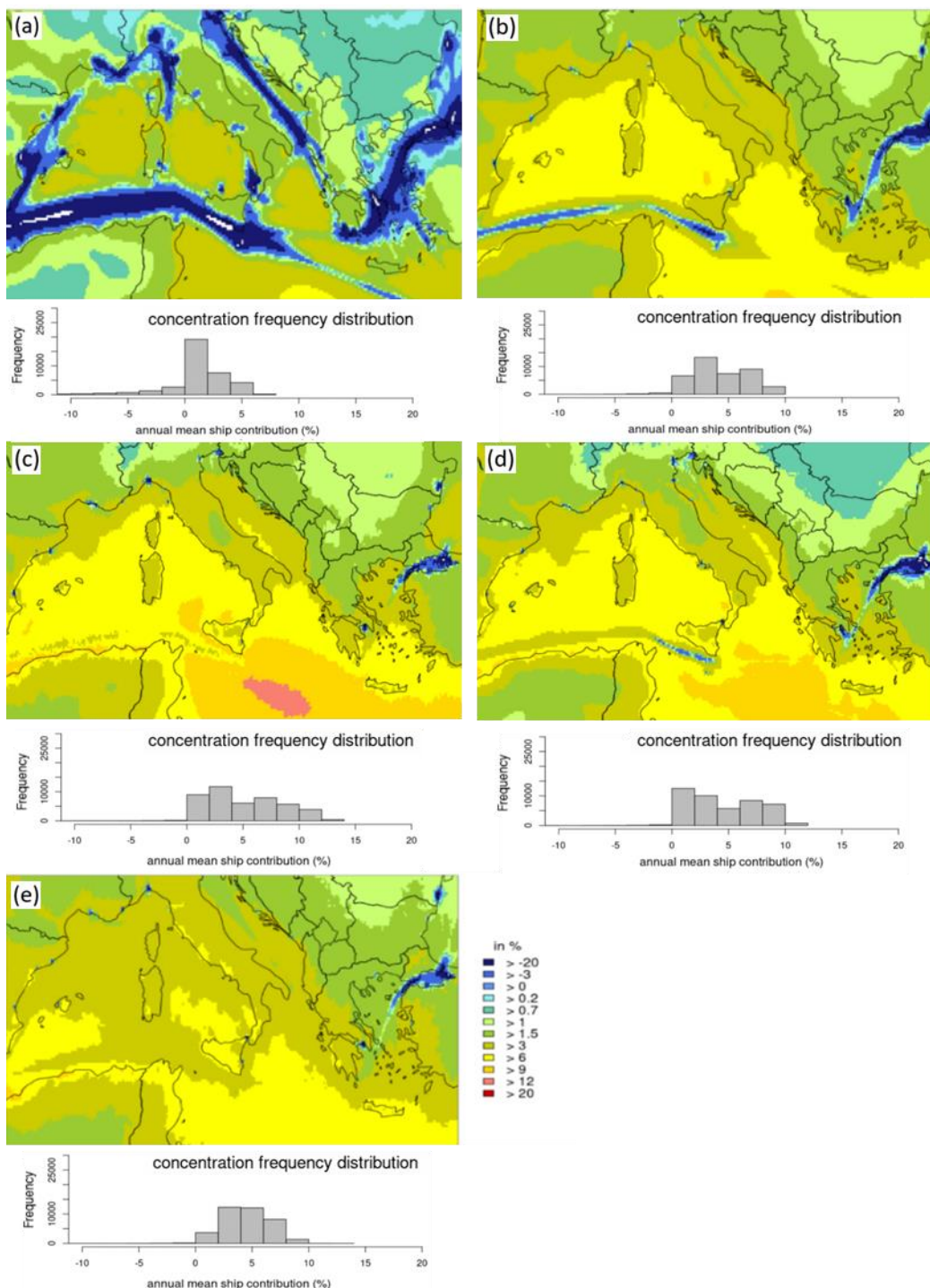


**Figure 16: Annual mean O<sub>3</sub> ship contribution. (a) = CAMx, (b) = CHIMERE, (c) = CMAQ, (d) = EMEP, (e) = LOTOS-EUROS; white areas display values below -20 %. Below the maps is the respective frequency distribution displayed for the annual mean O<sub>3</sub> ship contribution, referred to the whole model domain.**



### 3.2 O<sub>x</sub> Spatial Distribution

555 The oxidation of VOCs produce O<sub>3</sub> in the troposphere when nitrogen oxides (NO; NO<sub>2</sub>) and sunlight are present. Central to understanding this production is the photostationary state formed between NO, NO<sub>2</sub>, and O<sub>3</sub> in sunlight. In emission-free air, a steady equilibrium would be expected; nevertheless, emission sources disturb this equilibrium. In areas with high NO emissions, O<sub>3</sub> destruction is expected, resulting in lower O<sub>3</sub> concentrations along the main shipping routes, in urban areas and in harbor cities.

560 The results show that all five models tend to underestimate NO<sub>2</sub> and overestimate O<sub>3</sub>, but at different magnitudes. For a better understanding of photochemical air pollution and chemical coupling, the oxidant levels (O<sub>x</sub> = O<sub>3</sub> + NO<sub>2</sub>) were calculated and displayed for all emission sources and for the ship contribution. Clapp and Jenkin (2001) showed that the concentration of O<sub>x</sub> levels can be described as a NO<sub>x</sub>-independent regional contribution, where the O<sub>x</sub> contribution equates to the O<sub>3</sub> background, and a NO<sub>x</sub>-dependent local contribution. The NO<sub>x</sub>-dependent contribution correlates with the primary pollution, coming from direct NO<sub>2</sub> emissions or VOC, which promote conversion from NO to NO<sub>2</sub> (Clapp and Jenkin, 2001).

565 In comparison with the O<sub>3</sub> spatial distribution and frequency distribution, the annual mean concentration of O<sub>x</sub> displays a similar pattern for the model outputs (Figure 17). As was the case for O<sub>3</sub>, the CHIMERE and CAMx models show the highest values over the sea area, and EMEP shows the lowest values over land areas. The frequency distribution shows bimodal distributed values for CHIMERE, CMAQ and EMEP, as it was for O<sub>3</sub>. Thus, O<sub>x</sub> levels are mainly NO<sub>x</sub>-independent.

570 Nevertheless, NO<sub>x</sub>-dependent O<sub>x</sub> formation can also be seen in the ship contribution to the total O<sub>x</sub> concentration (Figure 18). High O<sub>x</sub> contributions at the main shipping routes for CHIMERE, CMAQ, EMEP and LOTOS-EUROS indicate the local contribution from shipping emissions (NO<sub>2</sub> and VOC), which cause high O<sub>x</sub> levels in these areas. For CAMx, such a pattern was not found.

### 3.3 NO<sub>x</sub> Spatial Distribution

575 To gain further insight into the differences in the lifetime of NO<sub>2</sub> in the models, NO<sub>x</sub> (= NO + NO<sub>2</sub>) was calculated and displayed (Appendix D). Differences in NO<sub>x</sub> give a hint on the lifetimes because of the reaction of NO<sub>2</sub> with OH to HNO<sub>3</sub>. The latter forms ammonium nitrate aerosol together with ammonia; thus, NO<sub>2</sub> is no longer in the gaseous phase. Another explanation is the dry deposition of NO<sub>2</sub>, which also causes a loss and consequently differences in the NO<sub>x</sub> pattern due to different deposition mechanisms.

580 The spatial distribution of the annual mean NO<sub>x</sub> and ship contribution to the total NO<sub>x</sub> concentration have shown a very similar pattern as for NO<sub>2</sub>. The values of CAMx and CHIMERE output are within one range, displaying higher values compared to CMAQ, EMEP and LOTOS-EUROS. These three models show an output that is also within one range.

To see the chemical fate of NO<sub>2</sub> the dry deposition could give a hint and will be considered in the following Sect 3.4.

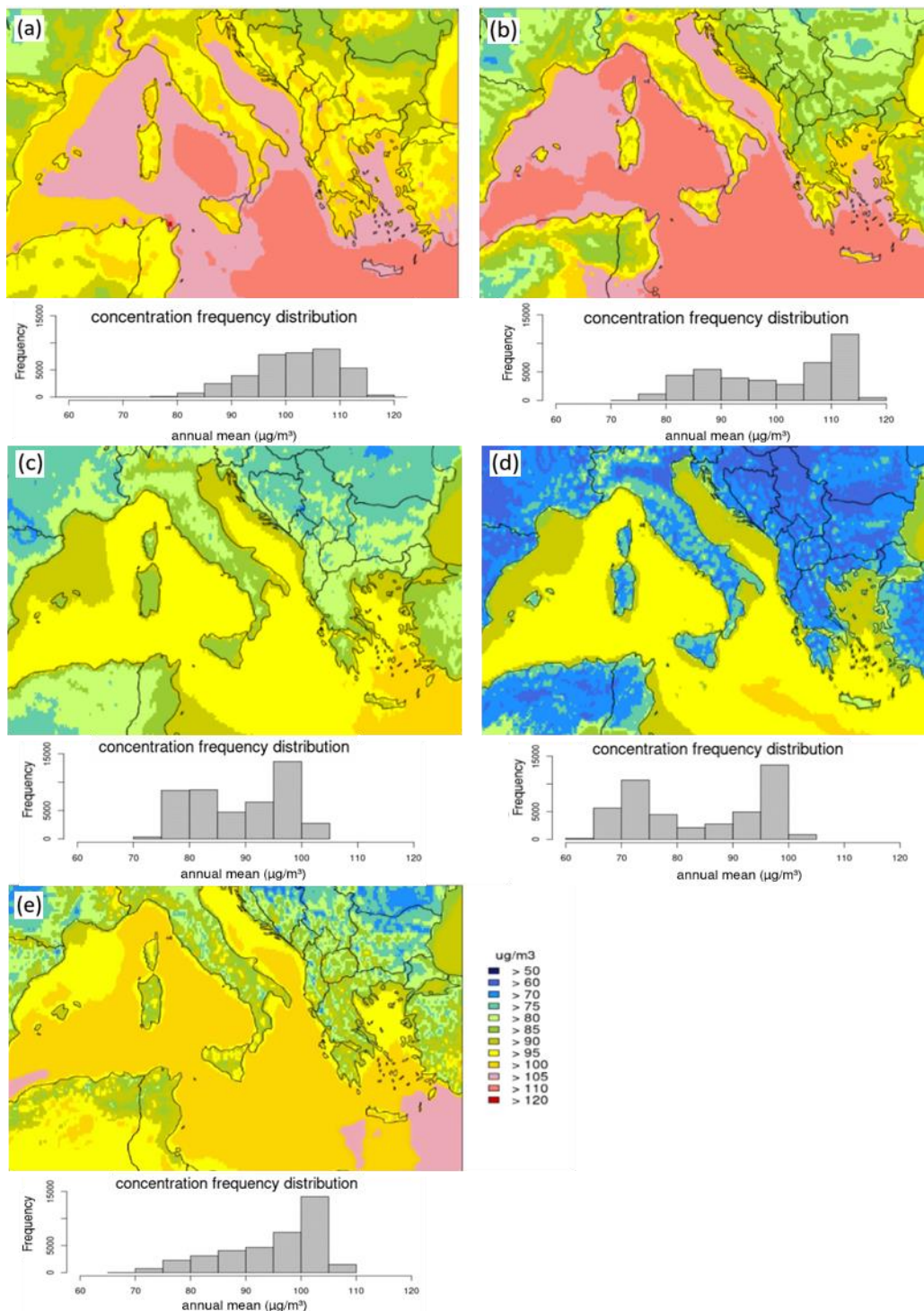


**Figure 17: Annual mean  $O_x$  ( $= \text{NO}_2 + \text{O}_3$ ) concentration. (a) = CAMx, (b) = CHIMERE, (c) = CMAQ, (d) = EMEP, (e) = LOTOS-EUROS. Below the maps is the respective frequency distribution for the annual mean  $O_x$  concentration, referred to the whole model domain.**

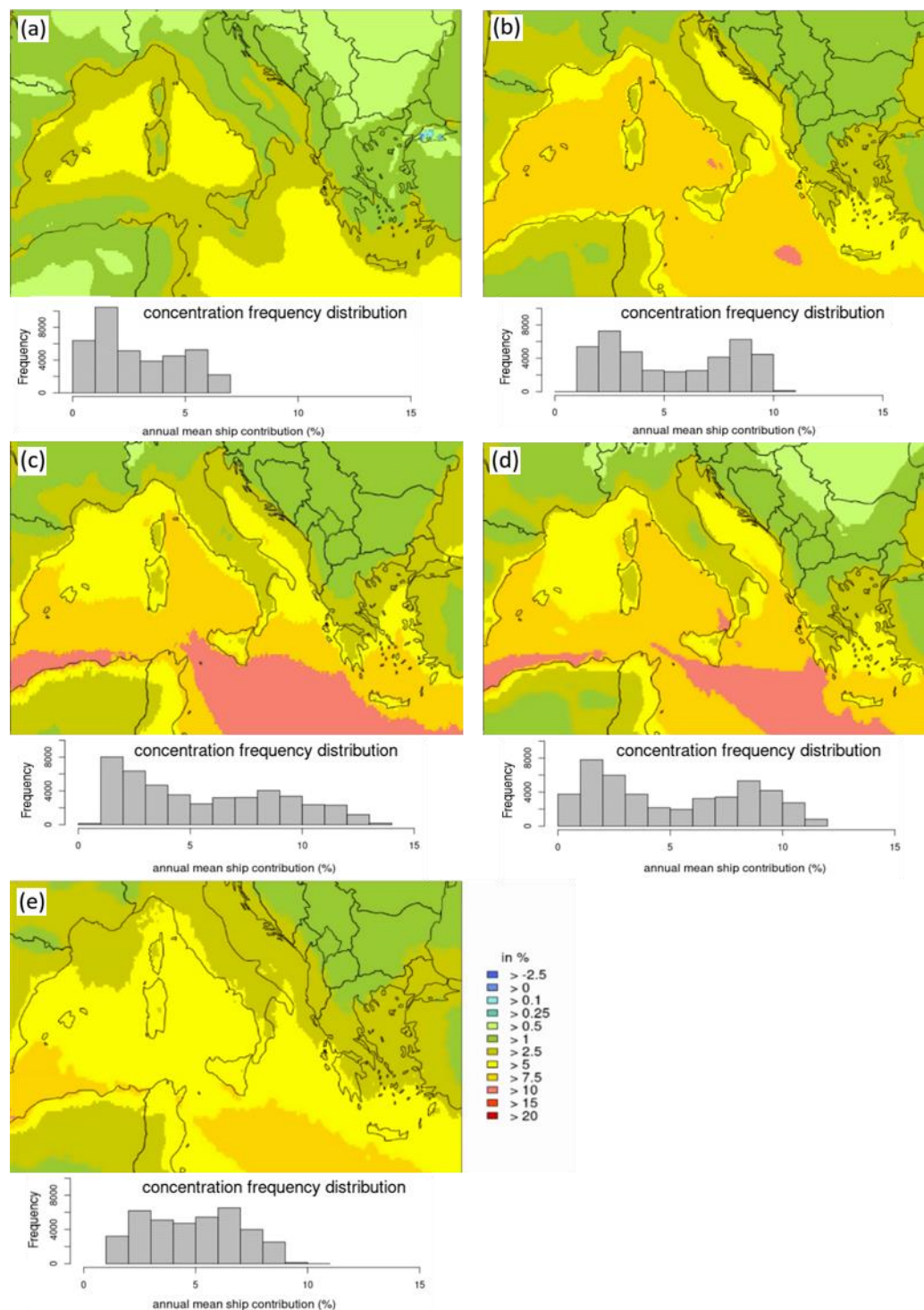


**Figure 18: Annual mean  $O_x$  ( $= NO_2 + O_3$ ) ship contribution. (a) = CAMx, (b) = CHIMERE, (c) = CMAQ, (d) = EMEP, (e) = LOTOS-EUROS. Below the maps is the respective frequency distribution is displayed for the annual mean  $O_x$  ship contribution, referred to the whole model domain.**



### 3.4 Dry Deposition

In the present study, dry deposition of NO<sub>2</sub> and O<sub>3</sub> are displayed for the base and the no ship case for CAMx, CHIMERE, CMAQ and LOTOS-EUROS. EMEP does not deliver separate NO<sub>2</sub> and O<sub>3</sub> deposition files but does deliver oxidized and reactive nitrogen. Thus, EMEP output is not considered in this chapter.

#### 3.4.1 Dry Deposition of NO<sub>2</sub>

The annual mean NO<sub>2</sub> dry deposition of all four compared models displays similar values over land areas (Figure 19). In cities and densely populated regions, all models show high NO<sub>2</sub> dry deposition, with values over 300 mg/m<sup>2</sup>/year. Nevertheless, the frequency distribution of all values shows that this is mainly the case for CAMx and LOTOS-EUROS. Additionally, over the sea, the pattern of annual mean dry deposition of NO<sub>2</sub> is also similar for CAMx and LOTOS-EUROS.

Table 7 shows that the correlation was strongest between CHIMERE and CAMx (R = 0.78). Similarities and strong correlations in the output of both models were also found for the NO<sub>2</sub> concentration in Section 3.1.2. This can be traced back to the same meteorology data that were used by both models.

The relative ship contribution to the annual dry deposition of NO<sub>2</sub> is displayed in Figure 20. The lowest ship contribution to NO<sub>2</sub> dry deposition is modeled by CMAQ and LOTOS-EUROS. In particular, CMAQ shows large areas with negative (-2.5 %) ship contributions over land. The CHIMERE output looks similar to the CAMx output over land. Along the coastline, CMAQ and LOTOS-EUROS show a ship contribution between 10 % and 25 %; CAMx and CHIMERE expect a ship contribution to the total annual deposition of 25 % to 75 %. The highest contribution is displayed by CAMx.

Differences in NO<sub>2</sub> dry deposition model output can be due to the dry deposition velocities but also due to the different meteorology data used by the models (Wichink Kruit et al., 2014).

Overall, the models have more differences in NO<sub>2</sub> dry deposition than in air concentration. As was the case for NO<sub>2</sub> concentration, CAMx simulated the highest values in dry deposition. The lowest values in NO<sub>2</sub> dry deposition are displayed by CMAQ. In addition, the correlation between CMAQ and the other models was lowest.

High NO<sub>2</sub> deposition over water areas caused by ships contributes to eutrophication (Vivanco et al., 2018). A study by Im et al. (2013) showed values of approximately 500 kg (N) m<sup>-2</sup> per year ( $\cong$  50000 mg/m<sup>2</sup>/year) over the Mediterranean Sea, which means an exceedance of the critical load of 2 g to 3 g (N) m<sup>-2</sup> per year ( $\cong$  2000 to 3000 mg/m<sup>2</sup>/year) to marine and coastal habitats (Bobbink and Hettelingh, 2011). The present study focused on NO<sub>2</sub> dry deposition; thus, a direct comparison with critical load levels or with other studies regarding total N deposition would not be possible. A subsequent calculation of N showed that the simulated values in the present study do not exceed the critical loads (Appendix E). Nevertheless, NO<sub>2</sub> dry deposition from ships contributes to the total N deposition budget, thus increasing with ship traffic and impacting the ecosystems in the Mediterranean Sea.



620 Table 7: Correlation between models for the whole domain (all grid cells) based on hourly data for NO<sub>2</sub> total dry deposition.

all	CAMx	CHIMERE	CMAQ	LOTOS-EUROS
LOTOS-EUROS	0.64	0.72	0.20	-
CMAQ	0.11	0.14	-	
CHIMERE	0.78	-		
CAMx	-			

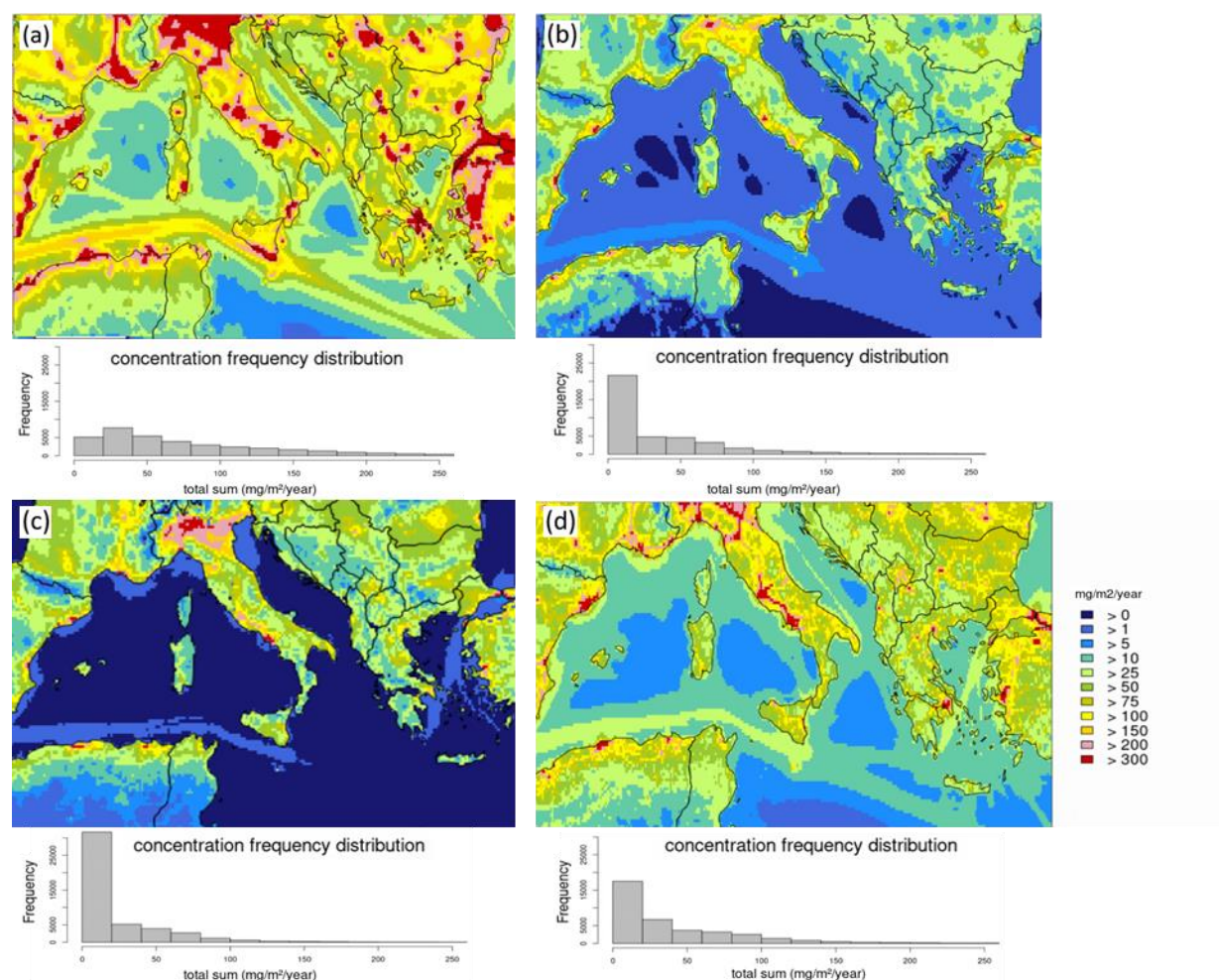
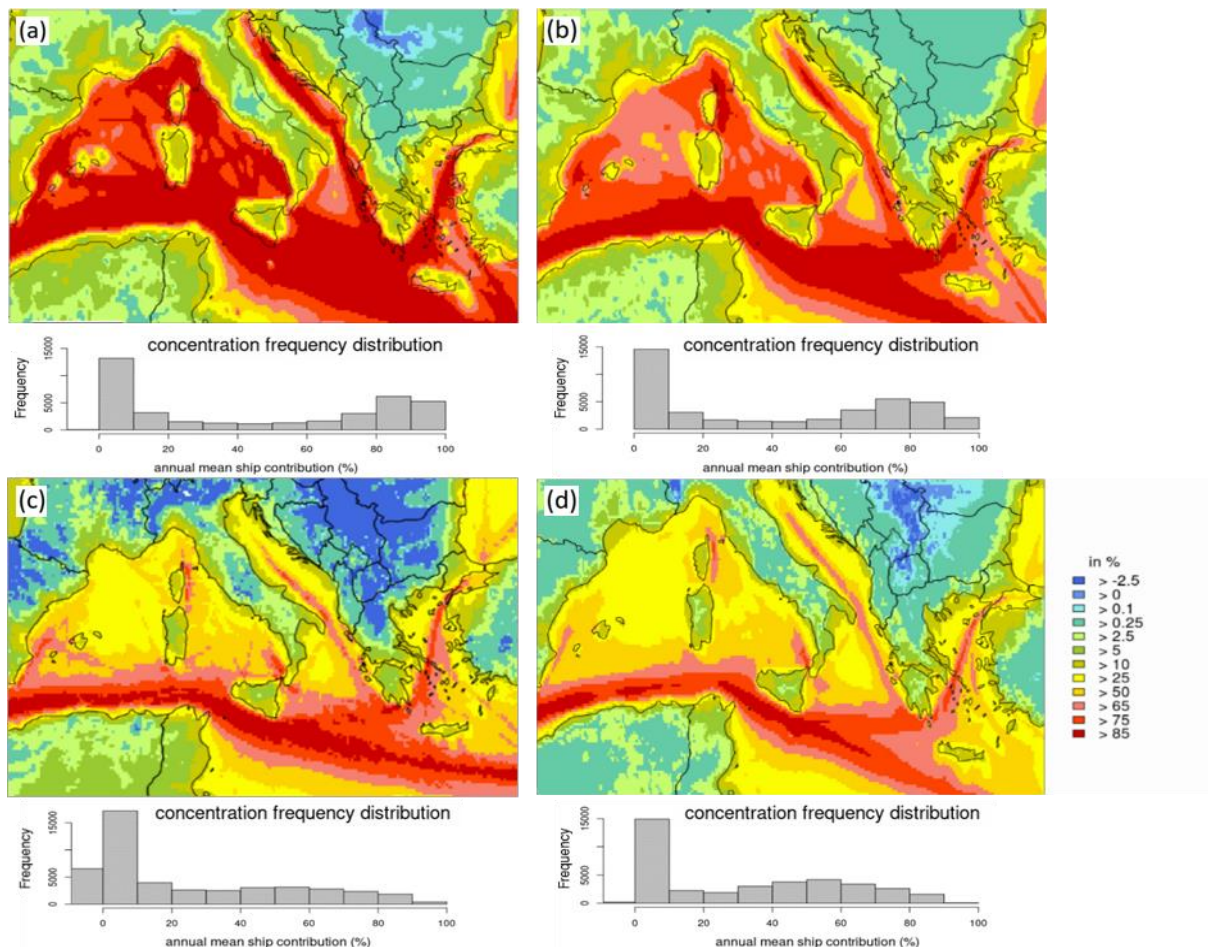


Figure 19: Annual total dry deposition of NO<sub>2</sub>. (a) = CAMx, (b) = CHIMERE, (c) = CMAQ, (d) = LOTOS-EUROS. Below the maps are the respective frequency distribution displayed for the annual mean NO<sub>2</sub> dry deposition, referred to the whole model domain.





**Figure 20: Annual mean dry deposition of NO<sub>2</sub> relative ship contribution. (a) = CAMx, (b) = CHIMERE, (c) = CMAQ, (d) = LOTOS-EUROS. Below the maps are the respective frequency distribution displayed for the annual mean NO<sub>2</sub> dry deposition ship contribution, referred to the whole model domain.**



### 625 3.4.2 Dry Deposition O<sub>3</sub>

Dry deposition is a major sink for O<sub>3</sub> in the lowest model layer. O<sub>3</sub> has high destruction rates on vegetated surfaces through plant stomata and lower rates on surfaces such as water or snow (Clifton et al., 2020). Spatial patterns of annual total O<sub>3</sub> dry deposition maps confirm this distribution. Over sea annual totals are lower (250 mg/m<sup>2</sup>/year to 1000 mg/m<sup>2</sup>/year) compared to values over land (2500 mg/m<sup>2</sup>/year to 10000 mg/m<sup>2</sup>/year; Figure 21). The correlation for the annual total concentration of O<sub>3</sub> dry deposition is highest between CHIMERE and CAMx, showing a moderate correlation (R = 0.59; Table 8). Nevertheless, the correlation is weak between all other models.

630 Figure 22 shows the ship contribution to the total dry deposition of O<sub>3</sub>. CMAQ and LOTOS-EUROS are within a similar range, with ship contributions of 5 % to 10 % over water surfaces. The lowest contribution of -5 % at the main shipping lanes is modeled by CAMx, showing a similar pattern as for the O<sub>3</sub> ship contribution. Over land areas, ships contribute to dry O<sub>3</sub> deposition from 0.25 % to 2.5 %.

In addition to the impact of O<sub>3</sub> dry deposition on plant stomata, it is important to explain differences in surface O<sub>3</sub> concentration model outputs. The O<sub>3</sub> concentration is sensitive to the deposition velocity (Clifton et al., 2020), which differs among the four models. This can be confirmed by studies comparing deposition schemes, where differences in O<sub>3</sub> concentration between models are caused by the variety of processes (Clifton et al., 2020). In particular, the variability in deposition velocities across models, as discussed in Sect. 3.3.1, is seen as an originator leading to uncertainties in tropospheric O<sub>3</sub> (Wild, 2007).

640 A model comparison study with 15 models by Hardacre et al. (2015) found the greatest differences in total O<sub>3</sub> dry deposition occurring in areas where deposition velocities and O<sub>3</sub> concentrations are highest. Additionally, soil moisture has an important impact on O<sub>3</sub> deposition and concentration. An evaluation study within the CHIMERE model found that especially in southern Europe, where soil is close to the wilting point during summer and affects stomatal opening, O<sub>3</sub> dry deposition declines (Anav et al., 2018). This in turn affects the concentration of gases in the lower atmosphere and thus has an impact on O<sub>3</sub> concentrations.



650 **Table 8: Correlation between models for the whole domain (all grid cells) based on hourly data for O<sub>3</sub> total dry deposition.**

<b>all</b>	<b>CAMx</b>	<b>CHIMERE</b>	<b>CMAQ</b>	<b>LOTOS- EUROS</b>
<b>LOTOS- EUROS</b>	0.32	0.39	0.08	-
<b>CMAQ</b>	0.11	0.04	-	
<b>CHIMERE</b>	0.59	-		
<b>CAMx</b>	-			

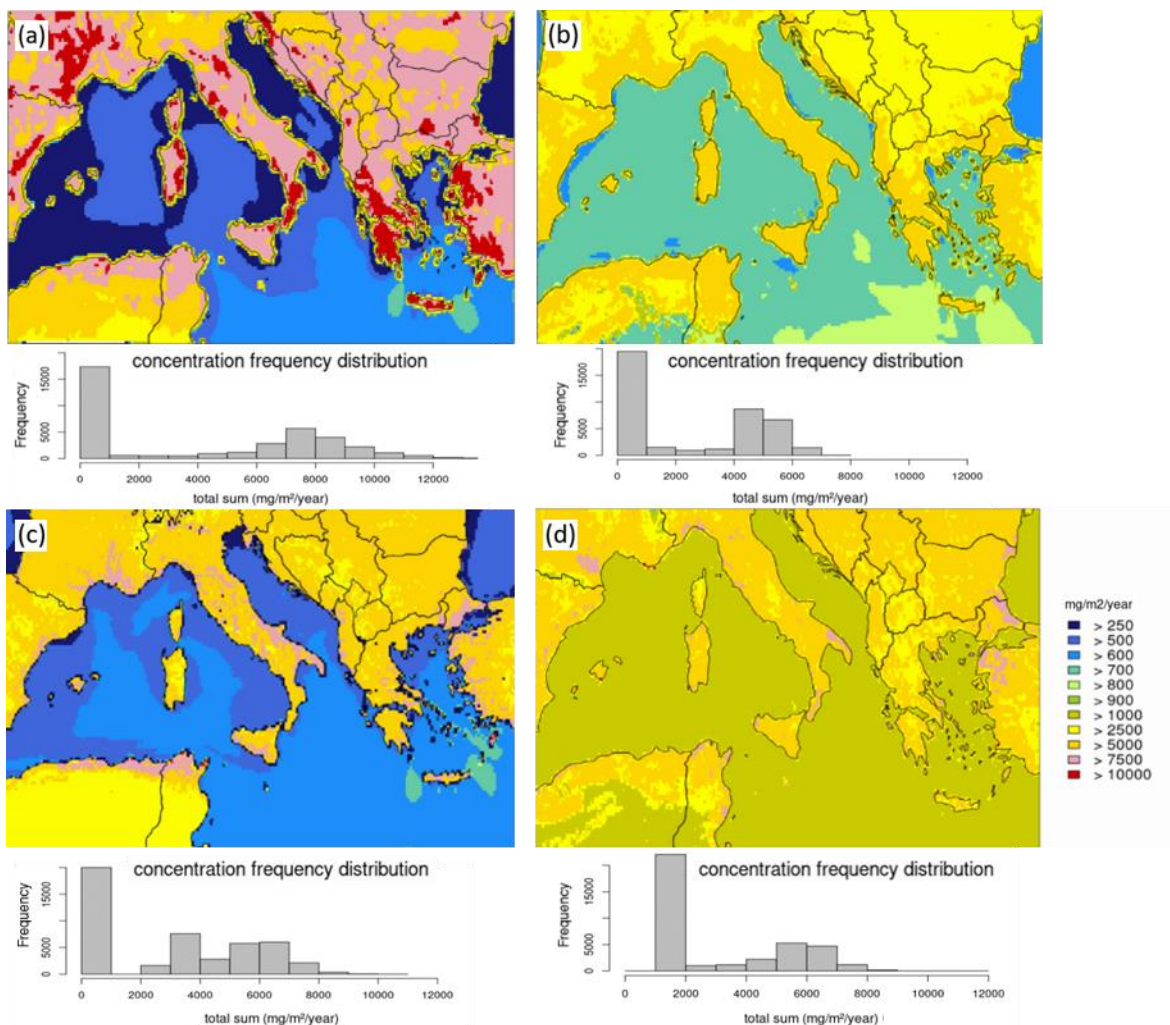


**Figure 21:** Annual total dry deposition of O<sub>3</sub>. (a) = CAMx, (b) = CHIMERE, (c) = CMAQ, (d) = LOTOS-EUROS. Below the maps are the respective frequency distribution displayed for the annual mean O<sub>3</sub> dry deposition, referred to the whole model domain.

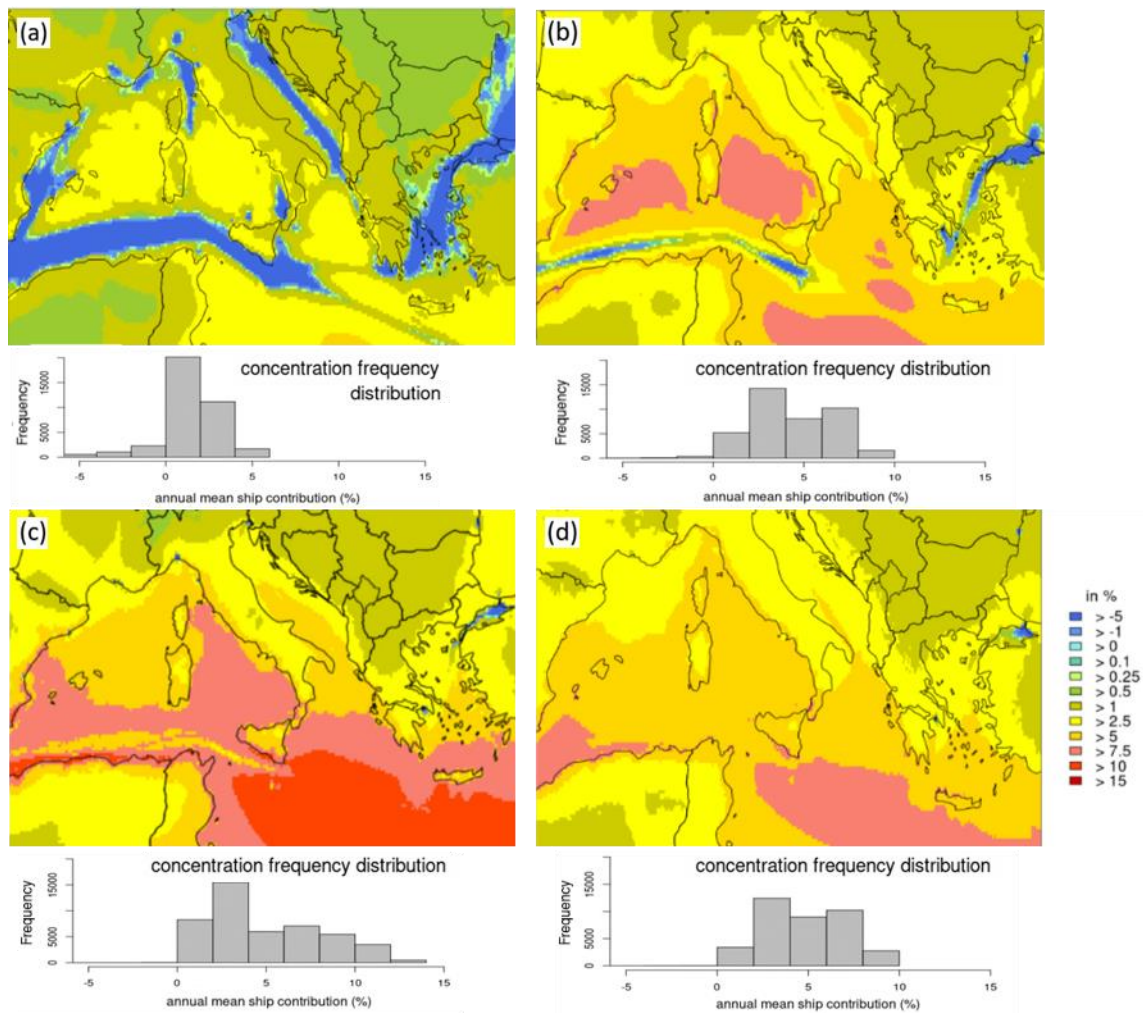


**Figure 22: Annual mean dry deposition of  $O_3$  relative ship contribution. (a) = CAMx, (b) = CHIMERE, (c) = CMAQ, (d) = LOTOS-EUROS. Below the maps are the respective frequency distribution displayed for the annual mean  $O_3$  dry deposition ship contribution, referred to the whole model domain.**



#### 655 **4 Summary and Conclusion**

The ship contribution to air pollution in the Mediterranean Sea was simulated with five different regional-scale CTMs (CAMx, CHIMERE, CMAQ, EMEP, LOTOS-EUROS). An evaluation of the results for NO<sub>2</sub> and O<sub>3</sub> concentrations is presented here. By using different CTMs, a more robust estimate of the ship contribution to atmospheric concentrations and deposition can be obtained compared to single model runs.

660 The emission data, modeled year and domain were the same for all models. The models were run in their standard setup. The outputs of the model runs were quantified by comparing the measurements from urban and rural background stations around the Mediterranean Sea.

The focus of the study was the comparison of model outputs concerning the concentration of regulatory pollutants and the calculation of ship contributions to total air pollution concentrations.

665 Concerning the results of NO<sub>2</sub>, the model performance showed differences in the time series between the models, caused by the large grid size and the differences in meteorology. All five CTMs underestimated the actual measured NO<sub>2</sub> concentration data at most stations, along with results from previous studies (e.g., Karl et al., 2019a; Giordano et al., 2015; Knote et al., 2015). The ship contribution to the total concentration of NO<sub>2</sub> at the measurement stations over land differed among the models. It was between 1.0 % and 15.3 % at the presented stations. Ship contributions mean values of several stations in one area, as  
670 shown in the supplements Figures S2-S9, display values up to 48.1 %. This was found in the eastern part of the domain (Figure S6), where the main shipping routes are close to the shore. Studies regarding the North and Baltic Seas found similar results because shipping lanes are located closer to the shore and have a higher contribution to the total NO<sub>2</sub> concentration in coastal regions (Matthias et al., 2010; Karl et al., 2019a). Nevertheless, over water, the maps in the present study display a ship contribution > 85 % at the main shipping routes. High values are also expected for the African coast since the main shipping  
675 route is close, but measurement stations are in continental Europe; no measurements were available for Northern Africa.

The variability in modeling the ship contribution was similar to that for the annual mean concentration of NO<sub>2</sub>. In both cases, CAMx and CHIMERE displayed the highest annual mean concentration and highest relative ship contribution. CMAQ, EMEP and LOTOS-EUROS simulated values within one range, which can be confirmed by similarities in frequency distribution. Comparison of the LOTOS-EUROS zero-out and tagging methods for NO<sub>2</sub> shows that the zero-out method models a larger  
680 range of values for ship contribution (-2.5 % to 85 %) compared to the tagging method (0.2 % to 75 %) with the largest deviations at the main shipping lanes. The comparison of both methods for ship contributions at measurement stations displayed even smaller differences, with the highest deviation of 3.1 % in ship contributions. This leads to the conclusion that the tagging results do not largely deviate from the zero-out method.

A relatively good model performance for O<sub>3</sub> was shown by all five models, but the model outputs differed in spatial distribution and ship contribution over water. An overestimation of O<sub>3</sub> was found at almost all stations. The overestimation of actual  
685 measured O<sub>3</sub> by models agrees with results found in other studies (Appel et al., 2017; Im et al., 2015a, b). Although boxplots for annual mean values of O<sub>3</sub> vary, for relative ship contribution they show that CHIMERE, CMAQ, EMEP and LOTOS-



EUROS are within one range. The relative contribution of ships to total O<sub>3</sub> decreases to -20 % in areas with high NO<sub>2</sub> concentrations in all model outputs, but mostly for CAMx. Diurnal cycles did not reveal differences in O<sub>3</sub> depletion over water  
690 and land between the models.

The focus of the second part of the present study was dry deposition of NO<sub>2</sub> and O<sub>3</sub>. The motivation to examine the dry deposition of NO<sub>2</sub> and O<sub>3</sub> more closely was to explain the model differences found for O<sub>3</sub> and NO<sub>2</sub>. Investigations of dry deposition are crucial to explain the conservation of mass and fate of these substances. Although dry deposition has effects on ecosystems and human health, the impact was not a major focus of the study.

695 Regarding air concentration, for NO<sub>2</sub> dry deposition and the ship contribution, CAMx showed the highest values. CMAQ displayed the lowest values in NO<sub>2</sub> dry deposition. Additionally, the correlation between CMAQ and the other models was lowest.

Along the shoreline, CMAQ and LOTOS-EUROS reveal a ship contribution between 10 % and 25 %; CAMx and CHIMERE expect a ship contribution to total annual NO<sub>2</sub> dry deposition of 25 % to 75 %, in some regions also along the coast. These  
700 differences are caused by mechanisms to calculate dry deposition velocities, which are unique for each model, as well as differing inputs, such as land use data (Wichink Kruit et al. 2014; Vivanco et al. 2018).

The ship contribution to the total dry deposition of O<sub>3</sub> displays the highest contribution with values between 75 % and 85 % by CHIMERE. CMAQ and LOTOS-EUROS are within a similar range, with ship contributions mainly 5 % to 10 % over water areas. The lowest contribution of -5 % at main shipping lanes is modelled by CAMx. The correlation of model-observation  
705 data for the annual total concentration of O<sub>3</sub> dry deposition was highest for CHIMERE and CAMx. Nevertheless, no or a low correlation was found for all other models.

In general, more deviations between the dry deposition model outputs were found compared to the model outputs of the air concentration of pollutants. This is because NO<sub>2</sub> and O<sub>3</sub> in the atmosphere are formed more or less “directly” from the emission data, but dry deposition differs because there are other, model-specific mechanisms behind it.

710 In an additional investigation of ship contributions to air pollution, aerosol particles and wet deposition also need to be considered, which is a next step in the current intercomparison study. The aerosol formation mechanism differs in most models; therefore, a detailed investigation of PM<sub>2.5</sub> and its chemical composition is necessary and will be part of further investigations in this project.

A more reliable estimate of ship contributions to the atmospheric concentration as well as deposition could be acquired when  
715 using five different CTMs than when using only one model. This estimate can be achieved using a mean value with standard deviations of model outputs, regarding all emissions but also ship contributions, as was done in the present study. This gives a data range that is more robust and reliable compared to the output of one single model. Furthermore, possible limitations, over- and underestimations of model outputs are pointed out with the intercomparison.



## 720 Acknowledgement

This work was supported by the SCIPPER project, which has received funding from the European Union's Horizon 2020 research and innovation programme under grant agreement Nr.814893.

## References

- 725 Agrawal, H., Welch, W. A., Henningsen, S., Miller, J. W., and Cocker, D. R.: Emissions from main propulsion engine on container ship at sea, 35, <https://doi.org/10.1029/2009JD013346>, 2010.
- Agrawal, H., Welch, W. A., Miller, J. W., and Cockert, D. R.: Emission measurements from a crude oil tanker at sea, 19, <https://doi.org/10.1021/es703102y>, 2008.
- Aksoyoglu, S., Baltensperger, U., and Prévôt, A. S. H.: Contribution of ship emissions to the concentration and deposition of air pollutants in Europe, 4, <https://doi.org/10.5194/acp-16-1895-2016>, 2016.
- 730 Anav, A., Proietti, C., Menut, L., Carnicelli, S., Marco, A. de, and Paoletti, E.: Sensitivity of stomatal conductance to soil moisture: Implications for tropospheric ozone, 8, <https://doi.org/10.5194/acp-18-5747-2018>, 2018.
- Appel, K. W., Napelenok, S. L., Foley, K. M., Pye, H. O. T., Hogrefe, C., Luecken, D. J., Bash, J. O., Roselle, S. J., Pleim, J. E., Foroutan, H., Hutzell, W. T., Pouliot, G. A., Sarwar, G., Fahey, K. M., Gantt, B., Gilliam, R. C., Heath, N. K., Kang, D., Mathur, R., Schwede, D. B., Spero, T. L., Wong, D. C., and Young, J. O.: Description and evaluation of the Community
- 735 Multiscale Air Quality (CMAQ) modeling system version 5.1, 4, <https://doi.org/10.5194/gmd-10-1703-2017>, 2017.
- Aulinger, A., Matthias, V., Zeretzke, M., Bieser, J., Quante, M., and Backes, A.: The impact of shipping emissions on air pollution in the greater North Sea region – Part 1: Current emissions and concentrations, 2, <https://doi.org/10.5194/acp-16-739-2016>, 2016.
- Baldasano, J. M., Pay, M. T., Jorba, O., Gassó, S., and Jiménez-Guerrero, P.: An annual assessment of air quality with the CALIOPE modeling system over Spain, 11, <https://doi.org/10.1016/j.scitotenv.2011.01.041>, 2011.
- Banzhaf, S., Schaap, M., Kerschbaumer, A., Reimer, E., Stern, R., van der Swaluw, E., and Builtjes, P.: Implementation and evaluation of pH-dependent cloud chemistry and wet deposition in the chemical transport model REM-Calgrid, 17, <https://doi.org/10.1016/j.atmosenv.2011.10.069>, 2012.
- Barregard, L., Molnàr, P., Jonson, J. E., and Stockfelt, L.: Impact on Population Health of Baltic Shipping Emissions, 11, <https://doi.org/10.3390/ijerph16111954>, 2019.
- Bergström, R., van der Denier Gon, H. A. C., Prévôt, A. S. H., Yttri, K. E., and Simpson, D.: Modelling of organic aerosols over Europe (2002–2007) using a volatility basis set (VBS) framework: application of different assumptions regarding the formation of secondary organic aerosol, 18, <https://doi.org/10.5194/acp-12-8499-2012>, 2012.
- Bessagnet, B., Pirovano, G., Mircea, M., Cuvelier, C., Aulinger, A., Calori, G., Ciarelli, G., Manders, A., Stern, R., Tsyro, S.,
- 750 García Vivanco, M., Thunis, P., Pay, M.-T., Colette, A., Couvidat, F., Meleux, F., Rouïl, L., Ung, A., Aksoyoglu, S., Baldasano, J. M., Bieser, J., Briganti, G., Cappelletti, A., D'Isidoro, M., Finardi, S., Kranenburg, R., Silibello, C., Carnevale, C., Aas, W., Dupont, J.-C., Fagerli, H., Gonzalez, L., Menut, L., Prévôt, A. S. H., Roberts, P., and White, L.: Presentation of the EURODELTA III intercomparison exercise – evaluation of the chemistry transport models' performance on criteria pollutants and joint analysis with meteorology, 19, <https://doi.org/10.5194/acp-16-12667-2016>, 2016.
- 755 Bieser, J., Aulinger, A., Matthias, V., Quante, M., and Builtjes, P.: SMOKE for Europe – adaptation, modification and evaluation of a comprehensive emission model for Europe, 1, <https://doi.org/10.5194/gmd-4-47-2011>, 2011a.





- Bieser, J., Aulinger, A., Matthias, V., Quante, M., and van der Denier Gon, H. A. C.: Vertical emission profiles for Europe based on plume rise calculations, 10, <https://doi.org/10.1016/j.envpol.2011.04.030>, 2011b.
- 760 Binkowski, F. S. and Shankar, U.: The Regional Particulate Matter Model: 1. Model description and preliminary results, 12, <https://doi.org/10.1029/95JD02093>, 1995.
- Bobbink, R. and Hettelingh, J.-P.: Review and revision of empirical critical loads and dose-response relationships, 2011.
- Brandt, J., Silver, J. D., Christensen, J. H., Andersen, M. S., Bønløkke, J. H., Sigsgaard, T., Geels, C., Gross, A., Hansen, A. B., Hansen, K. M., Hedegaard, G. B., Kaas, E., and Frohn, L. M.: Contribution from the ten major emission sectors in Europe and Denmark to the health-cost externalities of air pollution using the EVA model system – an integrated modelling approach, 15, <https://doi.org/10.5194/acp-13-7725-2013>, 2013.
- 765 Byun, D. and Schere, K. L.: Review of the Governing Equations, Computational Algorithms, and Other Components of the Models-3 Community Multiscale Air Quality (CMAQ) Modeling System, 2, <https://doi.org/10.1115/1.2128636>, 2006.
- Carlton, A. G., Bhawe, P. V., Napelenok, S. L., Edney, E. O., Sarwar, G., Pinder, R. W., Pouliot, G. A., and Houyoux, M.: Model representation of secondary organic aerosol in CMAQv4.7, 22, <https://doi.org/10.1021/es100636q>, 2010.
- 770 Celik, S., Drewnick, F., Fachinger, F., Brooks, J., Darbyshire, E., Coe, H., Paris, J.-D., Eger, P. G., Schuladen, J., Tadic, I., Friedrich, N., Dienhart, D., Hottmann, B., Fischer, H., Crowley, J. N., Harder, H., and Borrmann, S.: Influence of vessel characteristics and atmospheric processes on the gas and particle phase of ship emission plumes: In situ measurements in the Mediterranean Sea and around the Arabian Peninsula, 8, <https://doi.org/10.5194/acp-20-4713-2020>.
- Clapp, L. J. and Jenkin, M. E.: Analysis of the relationship between ambient levels of O<sub>3</sub>, NO<sub>2</sub> and NO as a function of NO<sub>x</sub> in the UK, 2001.
- 775 Clifton, O. E., Fiore, A. M., Massman, W. J., Baublitz, C. B., Coyle, M., Emberson, L., Fares, S., Farmer, D. K., Gentine, P., Gerosa, G., Guenther, A. B., Helmig, D., Lombardozzi, D. L., Munger, J. W., Patton, E. G., Pusede, S. E., Schwede, D. B., Silva, S. J., Sörgel, M., Steiner, A. L., and Tai, A. P. K.: Dry Deposition of Ozone over Land: Processes, Measurement, and Modeling, 1, <https://doi.org/10.1029/2019RG000670>, 2020.
- 780 Cofala, J., Amann, M., Borken-Kleefeld, J., Gomez-Sanabria, A., Heyes, C., Kiesewetter, G., Sander, R., Schoepp, W., Holland, M., Fagerli, H., and Nyiri, A.: Final Report. The potential for cost-effective air emission reductions from international shipping through designation of further Emission Control Areas in EU waters with focus on the Mediterranean Sea, 2018.
- Colette, A., Andersson, C., Manders, A., Mar, K., Mircea, M., Pay, M.-T., Raffort, V., Tsyro, S., Cuvelier, C., Adani, M., Bessagnet, B., Bergström, R., Briganti, G., Butler, T., Cappelletti, A., Couvidat, F., D'Isidoro, M., Doumbia, T., Fagerli, H., 785 Granier, C., Heyes, C., Klimont, Z., Ojha, N., Otero, N., Schaap, M., Sindelarova, K., Stegehuis, A. I., Roustan, Y., Vautard, R., van Meijgaard, E., Vivanco, M. G., and Wind, P.: EURODELTA-Trends, a multi-model experiment of air quality hindcast in Europe over 1990–2010, 9, <https://doi.org/10.5194/gmd-10-3255-2017>, 2017.
- Corbett, J. J. and Fischbeck, P.: Emissions from ships, *Science* 278 (5339). 823- 824, 1997.
- 790 Corbett, J. J., Fischbeck, P., and Pandis, S.: Global nitrogen and sulfur inventories for oceangoing ships, *Journal of Geophysical Research-Atmospheres* 104 (3). 3457-3470, 1999.
- Doche, C., Dufour, G., Foret, G., Eremenko, M., Cuesta, J., Beekmann, M., and Kalabokas, P.: Summertime tropospheric-ozone variability over the Mediterranean basin observed with IASI, 19, <https://doi.org/10.5194/acp-14-10589-2014>, 2014.
- Donahue, N. M., Robinson, A. L., and Pandis, S. N.: Atmospheric organic particulate matter: From smoke to secondary organic aerosol, 1, <https://doi.org/10.1016/j.atmosenv.2008.09.055>, 2009.



- 795 Donateo, A., Gregoris, E., Gambaro, A., Merico, E., Giua, R., Nocioni, A., and Contini, D.: Contribution of harbour activities and ship traffic to PM<sub>2.5</sub>, particle number concentrations and PAHs in a port city of the Mediterranean Sea (Italy), 15, <https://doi.org/10.1007/s11356-014-2849-0>, 2014.
- Emerson, E. W., Hodshire, A. L., DeBolt, H. M., Bilsback, K. R., Pierce, J. R., McMeeking, G. R., and Farmer, D. K.: Revisiting particle dry deposition and its role in radiative effect estimates, 42, <https://doi.org/10.1073/pnas.2014761117>, 2020.
- 800 Endresen, Ø., Sørgård, E., Sundet, J. K., Dalsøren, S. B., Isaksen, I. S., Berglen, T. F., and Gravir, G.: Emission from international sea transportation and environmental impact, D17, <https://doi.org/10.1029/2002JD002898>, 2003.
- EPA: Health Effects of Ozone Pollution, 2021.
- Erisman, J. W., van Pul, A., and Wyers, P.: Parametrization of surface resistance for the quantification of atmospheric deposition of acidifying pollutants and ozone, 16, [https://doi.org/10.1016/1352-2310\(94\)90433-2](https://doi.org/10.1016/1352-2310(94)90433-2), 1994.
- 805 European Commission, Joint Research Centre, Belis, C., Pirovano, G., Mircea, M., and Calori, G.: European guide on air pollution source apportionment for particulate matter with source oriented models and their combined use with receptor models, Publications Office, <https://doi.org/10.2760/470628>, 2020.
- Eurostat Press Office: World Maritime Day. Half of EU trade in goods is carried by sea, 2016.
- Eyring, V., Isaksen, I. S.A., Berntsen, T., Collins, W. J., Corbett, J. J., Endresen, O., Grainger, R. G., Moldanova, J., Schlager, H., and Stevenson, D. S.: Transport impacts on atmosphere and climate: Shipping, 37, <https://doi.org/10.1016/j.atmosenv.2009.04.059>, 2010.
- Fountoukis, C. and Nenes, A.: ISORROPIA II: A computationally efficient thermodynamic equilibrium model for K<sup>+</sup>–Ca<sup>2+</sup>–Mg<sup>2+</sup>–NH<sub>4</sub><sup>+</sup>–Na<sup>+</sup>–SO<sub>4</sub><sup>2-</sup>–NO<sub>3</sub><sup>-</sup>–Cl<sup>-</sup>–H<sub>2</sub>O aerosols, 17, <https://doi.org/10.5194/acp-7-4639-2007>, 2007.
- 815 Friedrich, N., Eger, P., Shenolikar, J., Sobanski, N., Schuladen, J., Dienhart, D., Hottmann, B., Tadic, I., Fischer, H., Martinez, M., Rohloff, R., Tauer, S., Harder, H., Pfannerstill, E. Y., Wang, N., Williams, J., Brooks, J., Drewnick, F., Su, H., Li, G., Cheng, Y., Lelieveld, J., and Crowley, J. N.: Reactive nitrogen around the Arabian Peninsula and in the Mediterranean Sea during the 2017 AQABA ship campaign, 10, <https://doi.org/10.5194/acp-21-7473-2021>, 2021.
- Galmarini, S., Makar, P., Clifton, O. E., Hogrefe, C., Bash, J. O., Bellasio, R., Bianconi, R., Bieser, J., Butler, T., Ducker, J., Flemming, J., Hodzic, A., Holmes, C. D., Kioutsioukis, I., Kranenburg, R., Lupascu, A., Perez-Camanyo, J. L., Pleim, J., Ryu, Y.-H., Jose, R. S., Schwede, D., Silva, S., and Wolke, R.: Technical note: AQMEII4 Activity 1: evaluation of wet and dry deposition schemes as an integral part of regional-scale air quality models, 20, <https://doi.org/10.5194/acp-21-15663-2021>, 2021.
- 820 Ginoux, P., Chin, M., Tegen, I., Prospero, J. M., Holben, B., Dubovik, O., and Lin, S.-J.: Sources and distributions of dust aerosols simulated with the GOCART model, D17, <https://doi.org/10.1029/2000JD000053>, 2001.
- 825 Giordano, L., Brunner, D., Flemming, J., Hogrefe, C., Im, U., Bianconi, R., Badia, A., Balzarini, A., Baró, R., Chemel, C., Curci, G., Forkel, R., Jiménez-Guerrero, P., Hirtl, M., Hodzic, A., Honzak, L., Jorba, O., Knote, C., Kuenen, J.J.P., Makar, P. A., Manders-Groot, A., Neal, L., Pérez, J. L., Pirovano, G., Pouliot, G., San José, R., Savage, N., Schröder, W., Sokhi, R. S., Syrakov, D., Torian, A., Tuccella, P., Werhahn, J., Wolke, R., Yahya, K., Žabkar, R., Zhang, Y., and Galmarini, S.: Assessment of the MACC reanalysis and its influence as chemical boundary conditions for regional air quality modeling in AQMEII-2, 1, <https://doi.org/10.1016/j.atmosenv.2015.02.034>, 2015.
- 830 Granier, C., Darras, S., van der Denier Gon, H., Doubalova, J., Elguindi, N., Galle, B., Gauss, M., Guevara, M., Jalkanen, J.-P., Kuenen, J., Liousse, C., Quack, B., Simpson, D., and Sindelarova, K.: The Copernicus Atmosphere Monitoring Service global and regional emissions: (April 2019 version), Copernicus Atmosphere Monitoring Service (CAMS) report, <https://doi.org/10.24380/d0bn-kx16>, 2019.



- 835 Guenther, A., Karl, T., Harley, P., Wiedinmyer, C., Palmer, P. I., and Geron, C.: Estimates of global terrestrial isoprene emissions using MEGAN (Model of Emissions of Gases and Aerosols from Nature), 11, 30 pp., <https://doi.org/10.5194/acp-6-3181-2006>, 2006.
- Guenther, A. B., Jiang, X., Heald, C. L., Sakulyanontvittaya, T., Duhl, T., Emmons, L. K., and Wang, X.: The Model of Emissions of Gases and Aerosols from Nature version 2.1 (MEGAN2.1): An extended and updated framework for modeling  
840 biogenic emissions, 6, 22 pp., <https://doi.org/10.5194/gmd-5-1471-2012>, 2012.
- Hardacre, C., Wild, O., and Emberson, L.: An evaluation of ozone dry deposition in global scale chemistry climate models, 11, <https://doi.org/10.5194/acp-15-6419-2015>, 2015.
- Hicks, B. B., Baldocchi, D. D., Meyers, T. P., Hosker, R. P., and Matt, D. R.: A preliminary multiple resistance routine for deriving dry deposition velocities from measured quantities, 3-4, <https://doi.org/10.1007/BF00229675>, 1987.
- 845 Im, U., Christodoulaki, S., Violaki, K., Zampas, P., Kocak, M., Daskalakis, N., Mihalopoulos, N., and Kanakidou, M.: Atmospheric deposition of nitrogen and sulfur over southern Europe with focus on the Mediterranean and the Black Sea, 1, <https://doi.org/10.1016/j.atmosenv.2013.09.048>, 2013.
- Im, U., Bianconi, R., Solazzo, E., Kioutsioukis, I., Badia, A., Balzarini, A., Baró, R., Bellasio, R., Brunner, D., Chemel, C.,  
850 Curci, G., Flemming, J., Forkel, R., Giordano, L., Jiménez-Guerrero, P., Hirtl, M., Hodzic, A., Honzak, L., Jorba, O., Knote, C., Kuenen, J. J. P., Makar, P. A., Manders-Groot, A., Neal, L., Pérez, J. L., Pirovano, G., Pouliot, G., San Jose, R., Savage, N., Schroder, W., Sokhi, R. S., Syrakov, D., Torian, A., Tuccella, P., Werhahn, J., Wolke, R., Yahya, K., Zabkar, R., Zhang, Y., Zhang, J., Hogrefe, C., and Galmarini, S.: Evaluation of operational on-line-coupled regional air quality models over Europe and North America in the context of AQMEII phase 2. Part I: Ozone, 4,  
855 <https://doi.org/10.1016/j.atmosenv.2014.09.042>, 2015a.
- Im, U., Bianconi, R., Solazzo, E., Kioutsioukis, I., Badia, A., Balzarini, A., Baró, R., Bellasio, R., Brunner, D., Chemel, C.,  
Curci, G., van der Denier Gon, H., Flemming, J., Forkel, R., Giordano, L., Jiménez-Guerrero, P., Hirtl, M., Hodzic, A., Honzak, L., Jorba, O., Knote, C., Makar, P. A., Manders-Groot, A., Neal, L., Pérez, J. L., Pirovano, G., Pouliot, G., San Jose, R., Savage, N., Schroder, W., Sokhi, R. S., Syrakov, D., Torian, A., Tuccella, P., Wang, K., Werhahn, J., Wolke, R., Zabkar, R., Zhang, Y., Zhang, J., Hogrefe, C., and Galmarini, S.: Evaluation of operational online-coupled regional air quality models over Europe  
860 and North America in the context of AQMEII phase 2. Part II: Particulate matter, 17, <https://doi.org/10.1016/j.atmosenv.2014.08.072>, 2015b.
- Inness, A., Ades, M., Agustí-Panareda, A., Barré, J., Benedictow, A., Blechschmidt, A.-M., Dominguez, J. J., Engelen, R.,  
Eskes, H., Flemming, J., Huijnen, V., Jones, L., Kipling, Z., Massart, S., Parrington, M., Peuch, V.-H., Razinger, M., Remy, S., Schulz, M., and Suttie, M.: The CAMS reanalysis of atmospheric composition, 6, <https://doi.org/10.5194/acp-19-3515-2019>, 2019.
- Jägerbrand, A. K., Brutemark, A., Barthel Svedén, J., and Gren, I.-M.: A review on the environmental impacts of shipping on aquatic and nearshore ecosystems, <https://doi.org/10.1016/j.scitotenv.2019.133637>, 2019.
- Jalkanen, J.-P., Johansson, L., Kukkonen, J., Brink, A., Kalli, J., and Stipa, T.: Extension of an assessment model of ship traffic exhaust emissions for particulate matter and carbon monoxide, 5, 19 pp., <https://doi.org/10.5194/acp-12-2641-2012>, 2012.
- 870 Jalkanen, J.-P., Johansson, L., and Kukkonen, J.: A comprehensive inventory of ship traffic exhaust emissions in the European sea areas in 2011, 1, <https://doi.org/10.5194/acp-16-71-2016>, 2016.
- Jalkanen, J.-P., Brink, A., Kalli, J., Pettersson, H., Kukkonen, J., and Stipa, T.: A modelling system for the exhaust emissions of marine traffic and its application in the Baltic Sea area, 23, <https://doi.org/10.5194/acp-9-9209-2009>, 2009.



- Johansson, L., Jalkanen, J.-P., Kalli, J., and Kukkonen, J.: The evolution of shipping emissions and the costs of regulation changes in the northern EU area, 22, <https://doi.org/10.5194/acp-13-11375-2013>, 2013.
- Johansson, L., Jalkanen, J.-P., and Kukkonen, J.: Global assessment of shipping emissions in 2015 on a high spatial and temporal resolution, 2, <https://doi.org/10.1016/j.atmosenv.2017.08.042>, 2017.
- 880 Jonson, J. E., Jalkanen, J. P., Johansson, L., Gauss, M., and van der Denier Gon, H. A. C.: Model calculations of the effects of present and future emissions of air pollutants from shipping in the Baltic Sea and the North Sea, 2, <https://doi.org/10.5194/acp-15-783-2015>, 2015.
- Jutterström, S., Moldan, F., Moldanová, J., Karl, M., Matthias, V., and Posch, M.: The impact of nitrogen and sulfur emissions from shipping on the exceedance of critical loads in the Baltic Sea region, *Atmos. Chem. Phys.*, 21, 15827–15845, <https://doi.org/10.5194/acp-21-15827-2021>, 2021.
- 885 Karl, M., Jonson, J. E., Uppstu, A., Aulinger, A., Prank, M., Jalkanen, J.-P., Johansson, L., Quante, M., and Matthias, V.: Effects of ship emissions on air quality in the Baltic Sea region simulated with three different chemistry transport models, <https://doi.org/10.5194/acp-2018-1317>, 2019a.
- Karl, M., Bieser, J., Geyer, B., Matthias, V., Jalkanen, J.-P., Johansson, L., and Fridell, E.: Impact of a nitrogen emission control area (NECA) on the future air quality and nitrogen deposition to seawater in the Baltic Sea region, 3, <https://doi.org/10.5194/acp-19-1721-2019>, 2019b.
- 890 Kelly, J. T., Bhave, P. V., Nolte, C. G., Shankar, U., and Foley, K. M.: Simulating emission and chemical evolution of coarse sea-salt particles in the Community Multiscale Air Quality (CMAQ) model, 1, <https://doi.org/10.5194/gmd-3-257-2010>, 2010.
- Knote, C., Tuccella, P., Curci, G., Emmons, L., Orlando, J. J., Madronich, S., Baró, R., Jiménez-Guerrero, P., Luecken, D., Hogrefe, C., Forkel, R., Werhahn, J., Hirtl, M., Pérez, J. L., San José, R., Giordano, L., Brunner, D., Yahya, K., and Zhang, Y.: Influence of the choice of gas-phase mechanism on predictions of key gaseous pollutants during the AQMEII phase-2 intercomparison, 40, <https://doi.org/10.1016/j.atmosenv.2014.11.066>, 2015.
- Liu, J. J., Jones, D. B. A., Worden, J. R., Noone, D., Parrington, M., and Kar, J.: Analysis of the summertime buildup of tropospheric ozone abundances over the Middle East and North Africa as observed by the Tropospheric Emission Spectrometer instrument, D5, <https://doi.org/10.1029/2008JD010993>, 2009.
- 900 Manders, A. M. M., Bultjes, P. J. H., Curier, L., van der Denier Gon, H. A. C., Hendriks, C., Jonkers, S., Kranenburg, R., Kuenen, J. J. P., Segers, A. J., Timmermans, R. M. A., Visschedijk, A. J. H., Wichink Kruit, R. J., van Pul, W. A. J., Sauter, F. J., van der Swaluw, E., Swart, D. P. J., Douros, J., Eskes, H., van Meijgaard, E., van Ulft, B., van Velthoven, P., Banzhaf, S., Mues, A. C., Stern, R., Fu, G., Lu, S., Heemink, A., van Velzen, N., and Schaap, M.: Curriculum vitae of the LOTOS–EUROS (v2.0) chemistry transport model, 11, <https://doi.org/10.5194/gmd-10-4145-2017>, 2017.
- Manders-Groot, A., Segers, A., and Jonkers, S.: LOTOS-EUROS v2.0 Reference Guide, 2016.
- Marmer, E. and Langmann, B.: Impact of ship emissions on the Mediterranean summertime pollution and climate: A regional model study, 26, <https://doi.org/10.1016/j.atmosenv.2005.04.014>, 2005.
- 910 Mårtensson, E. M., Nilsson, E. D., Leeuw, G. de, Cohen, L. H., and Hansson, H.-C.: Laboratory simulations and parameterization of the primary marine aerosol production, D9, <https://doi.org/10.1029/2002JD002263>, 2003.
- Matthias, V., Bewersdorff, I., Aulinger, A., and Quante, M.: The contribution of ship emissions to air pollution in the North Sea regions, 6, <https://doi.org/10.1016/j.envpol.2010.02.013>, 2010.



- 915 Menut, L., Bessagnet, B., Khvorostyanov, D., Beekmann, M., Blond, N., Colette, A., Coll, I., Curci, G., Foret, G., Hodzic, A., Mailler, S., Meleux, F., Monge, J.-L., Pison, I., Siour, G., Turquety, S., Valari, M., Vautard, R., and Vivanco, M. G.: CHIMERE 2013: A model for regional atmospheric composition modelling, 4, <https://doi.org/10.5194/gmd-6-981-2013>, 2013.
- Mertens, M., Grewe, V., Rieger, V. S., and Jöckel, P.: Revisiting the contribution of land transport and shipping emissions to tropospheric ozone, 8, <https://doi.org/10.5194/acp-18-5567-2018>, 2018.
- 920 Monahan, E. C., Spiel, D. E., and Davidson, K. L.: A Model of Marine Aerosol Generation Via Whitecaps and Wave Disruption, [https://doi.org/10.1007/978-94-009-4668-2\\_16](https://doi.org/10.1007/978-94-009-4668-2_16), 1986.
- Nenes, A., Pandis, S. N., and Pilinis, C.: ISORROPIA: A New Thermodynamic Equilibrium Model for Multiphase Multicomponent Inorganic Aerosols, 1, <https://doi.org/10.1023/A:1009604003981>, 1998.
- 925 Nunes, R. A. O., Alvim-Ferraz, M. C. M., Martins, F. G., Calderay-Cayetano, F., Durán-Grados, V., Moreno-Gutiérrez, J., Jalkanen, J.-P., Hannuniemi, H., and Sousa, S. I. V.: Shipping emissions in the Iberian Peninsula and the impacts on air quality, 15, <https://doi.org/10.5194/acp-20-9473-2020>, 2020.
- Ordóñez, C., Richter, A., Steinbacher, M., Zellweger, C., Nüß, H., Burrows, J. P., and Prévôt, A. S. H.: Comparison of 7 years of satellite-borne and ground-based tropospheric NO<sub>2</sub> measurements around Milan, Italy, D5, <https://doi.org/10.1029/2005JD006305>, 2006.
- 930 Petrik, R., Geyer, B., and Rockel, B.: On the diurnal cycle and variability of winds in the lower planetary boundary layer: evaluation of regional reanalyses and hindcasts, 1, <https://doi.org/10.1080/16000870.2020.1804294>, 2021.
- Pleim, J. and Ran, L.: Surface Flux Modeling for Air Quality Applications, 3, <https://doi.org/10.3390/atmos2030271>, 2011.
- Prati, M. V., Costagliola, M. A., Quaranta, F., and Murena, F.: Assessment of ambient air quality in the port of Naples, 8, <https://doi.org/10.1080/10962247.2015.1050129>, 2015.
- 935 Pye, H. O. T. and Pouliot, G. A.: Modeling the role of alkanes, polycyclic aromatic hydrocarbons, and their oligomers in secondary organic aerosol formation, 11, 2012.
- Ramboll Environment and Health: User's Guide COMPREHENSIVE AIR QUALITY MODEL WITH EXTENSIONS: Version 7.10, 2020.
- 940 Reichle, L. J., Cook, R., Yanca, C. A., and Sonntag, D. B.: Development of organic gas exhaust speciation profiles for nonroad spark-ignition and compression-ignition engines and equipment, 10, <https://doi.org/10.1080/10962247.2015.1020118>, 2015.
- Robinson, A. L., Donahue, N. M., Shrivastava, M. K., Weitkamp, E. A., Sage, A. M., Grieshop, A. P., Lane, T. E., Pierce, J. R., and Pandis, S. N.: Rethinking organic aerosols: semivolatile emissions and photochemical aging, 5816, <https://doi.org/10.1126/science.1133061>, 2007.
- 945 Safieddine, S., Boynard, A., Coheur, P.-F., Hurtmans, D., Pfister, G., Quennehen, B., Thomas, J. L., Raut, J.-C., Law, K. S., Klimont, Z., Hadji-Lazarou, J., George, M., and Clerbaux, C.: Summertime tropospheric ozone assessment over the Mediterranean region using the thermal infrared IASI/MetOp sounder and the WRF-Chem model, 18, <https://doi.org/10.5194/acp-14-10119-2014>, 2014.
- 950 Schaap, M., Timmermans, R. M.A., Roemer, M., Boersen, G.A.C., Builtjes, P. J.H., Sauter, F. J., Velders, G. J.M., and Beck, J. P.: The LOTOS EUROS model: Description, validation and latest developments, 2, <https://doi.org/10.1504/IJEP.2008.017106>, 2008.



- Schembari, C., Cavalli, F., Cuccia, E., Hjorth, J., Calzolari, G., Pérez, N., Pey, J., Prati, P., and Raes, F.: Impact of a European directive on ship emissions on air quality in Mediterranean harbours, 3, <https://doi.org/10.1016/j.atmosenv.2012.06.047>, 2012.
- 955 Schober, P., Boer, C., and Schwarte, L. A.: Correlation Coefficients: Appropriate Use and Interpretation, 5, <https://doi.org/10.1213/ANE.0000000000002864>, 2018.
- Schultze, M. and Rockel, B.: Direct and semi-direct effects of aerosol climatologies on long-term climate simulations over Europe, 9-10, <https://doi.org/10.1007/s00382-017-3808-5>, 2018.
- Schulz, M., Textor, C., Kinne, S., Balkanski, Y., Bauer, S., Berntsen, T., Berglen, T., Boucher, O., Dentener, F., Guibert, S., Isaksen, I. S. A., Iversen, T., Koch, D., Kirkevåg, A., Liu, X., Montanaro, V., Myhre, G., Penner, J. E., Pitari, G., Reddy, S., Seland, Ø., Stier, P., and Takemura, T.: Radiative forcing by aerosols as derived from the AeroCom present-day and pre-industrial simulations, 12, <https://doi.org/10.5194/acp-6-5225-2006>, 2006.
- 960 Simpson, D., Benedictow, A., Berge, H., Bergström, R., Emberson, L. D., Fagerli, H., Flechard, C. R., Hayman, G. D., Gauss, M., Jonson, J. E., Jenkin, M. E., Nyíri, A., Richter, C., Semeena, V. S., Tsyro, S., Tuovinen, J.-P., Valdebenito, Á., and Wind, P.: The EMEP MSC-W chemical transport model – technical description, 16, <https://doi.org/10.5194/acp-12-7825-2012>, 2012.
- 965 Simpson, D., Fagerli, H., Jonson, J. E., Tsyro, S., and Wind, P.: Transboundary Acidification, Eutrophication and Ground Level Ozone in Europe. PART I. Unified EMEP Model Description., 2003.
- Simpson, D., Bergström, R., Briolat, A., Imhof, H., Johansson, J., Priestley, M., and Valdebenito, A.: GenChem v1.0 – a chemical pre-processing and testing system for atmospheric modelling, 12, <https://doi.org/10.5194/gmd-13-6447-2020>, 2020.
- 970 Sippula, O., Stengel, B., Sklorz, M., Streibel, T., Rabe, R., Orasche, J., Lintelmann, J., Michalke, B., Abbaszade, G., Radischat, C., Gröger, T., Schnelle-Kreis, J., Harndorf, H., and Zimmermann, R.: Particle emissions from a marine engine: chemical composition and aromatic emission profiles under various operating conditions, 19, <https://doi.org/10.1021/es502484z>, 2014.
- Tadic, I., Crowley, J. N., Dienhart, D., Eger, P., Harder, H., Hottmann, B., Martinez, M., Parchatka, U., Paris, J.-D., Pozzer, A., Rohloff, R., Schuladen, J., Shenolikar, J., Tauer, S., Lelieveld, J., and Fischer, H.: Net ozone production and its relationship to nitrogen oxides and volatile organic compounds in the marine boundary layer around the Arabian Peninsula, 11, <https://doi.org/10.5194/acp-20-6769-2020>, 2020.
- 975 Thürkow, M., Pültz, J., Banzhaf, S., Butler, T., Kranenburg, R., and Schaap, M.: Source attribution of nitrogen oxides across Germany with the LOTOS-EUROS CTM, International Technical Meeting on Air Pollution Modelling and its Application, Barcelona, 2021.
- 980 Tysro, S. G. and Berge, E.: The Contribution of Ship Emission from the North Sea and the North-eastern Atlantic Ocean to Acidification in Europe, EMEP/MSC-W Note 4/97. EMEP. Meteorol. Synthesizing Centre e West, Norwegian Meteorological Institute, Oslo. Norway, 1997.
- van Zanten, M. C., Sauter, F. J., Wichink Kruit, R. J., van Jaarsveld, J. A., and van Pul, W. A. J.: Description of the DEPAC module: Dry deposition modelling with DEPAC\_GCN2010, 76 pp., 2010.
- 985 Večeřa, Z., Mikuška, P., Smolík, J., Eleftheriadis, K., Bryant, C., Colbeck, I., and Lazaridis, M.: Shipboard Measurements of Nitrogen Dioxide, Nitrous Acid, Nitric Acid and Ozone in the Eastern Mediterranean Sea, 1, <https://doi.org/10.1007/s11267-007-9133-y>, 2008.
- 990 Viana, M., Hammingh, P., Colette, A., Querol, X., Degraeuwe, B., Vliieger, I. d., and van Aardenne, J.: Impact of maritime transport emissions on coastal air quality in Europe, <https://doi.org/10.1016/j.atmosenv.2014.03.046>, 2014.



- 995 Vivanco, M. G., Theobald, M. R., García-Gómez, H., Garrido, J. L., Prank, M., Aas, W., Adani, M., Alyuz, U., Andersson, C., Bellasio, R., Bessagnet, B., Bianconi, R., Bieser, J., Brandt, J., Briganti, G., Cappelletti, A., Curci, G., Christensen, J. H., Colette, A., Couvidat, F., Cuvelier, C., D'Isidoro, M., Flemming, J., Fraser, A., Geels, C., Hansen, K. M., Hogrefe, C., Im, U., Jorba, O., Kitwiroon, N., Manders, A., Mircea, M., Otero, N., Pay, M.-T., Pozzoli, L., Solazzo, E., Tsyro, S., Unal, A., Wind, P., and Galmarini, S.: Modeled deposition of nitrogen and sulfur in Europe estimated by 14 air quality model systems: evaluation, effects of changes in emissions and implications for habitat protection, 14, <https://doi.org/10.5194/acp-18-10199-2018>, 2018.
- 1000 Wesely, M. L.: Parameterization of surface resistances to gaseous dry deposition in regional-scale numerical models, 6, [https://doi.org/10.1016/0004-6981\(89\)90153-4](https://doi.org/10.1016/0004-6981(89)90153-4), 1989.
- Whitten, G. Z., Heo, G., Kimura, Y., McDonald-Buller, E., Allen, D. T., Carter, W. P.L., and Yarwood, G.: A new condensed toluene mechanism for Carbon Bond: CB05-TU☆, 40, 12 pp., <https://doi.org/10.1016/j.atmosenv.2009.12.029>, 2010.
- Wichink Kruit, R. J., Schaap, M., Sauter, F. J., van Zanten, M. C., and van Pul, W. A. J.: Modeling the distribution of ammonia across Europe including bi-directional surface-atmosphere exchange, <https://doi.org/10.5194/bgd-9-4877-2012>, 2012.
- 1005 Wichink Kruit, R. W., Schaap, M., Segers, A., Heslinga, D., Builjtes, P., Branzhaf, S., and Scheuschner, T.: Modelling and mapping of atmospheric nitrogen and sulphur deposition and critical loads for ecosystem specific assessment of threats to biodiversity in Germany – PINETI (Pollutant INput and EcosysTem Impact) Substudy Report 1., 2014.
- 1010 Wiedinmyer, C., Akagi, S. K., Yokelson, R. J., Emmons, L. K., Al-Saadi, J. A., Orlando, J. J., and Soja, A. J.: The Fire INventory from NCAR (FINN): A high resolution global model to estimate the emissions from open burning, 3, <https://doi.org/10.5194/gmd-4-625-2011>, 2011.
- Wild, O.: Modelling the global tropospheric ozone budget: Exploring the variability in current models, 10, <https://doi.org/10.5194/acp-7-2643-2007>, 2007.
- Yarwood, G., Rao, S., Yocke, M., and Whitten, G. Z.: Updates to the carbon bond chemical mechanism: CB05. 2005.
- 1015 van Zanten, M. C., Sauter, F. J., Wichink Kruit, R. J., van Jaarsveld, J. A., and van Pul, W.A.J.: Description of the DEPAC module: Dry deposition modelling with DEPAC\_GCIN2010, RIVM Report 680180001/2010, 2010.
- Zhang, L., Brook, J. R., and Vet, R.: A revised parameterization for gaseous dry deposition in air-quality models, 6, <https://doi.org/10.5194/acp-3-2067-2003>, 2003.



## Appendix

### Appendix A: Definitions of NMB, R and RMSE

$$\text{Normalized Mean Bias (NMB)} = \frac{\sum_1^n (M-O)}{\sum_1^n (O)} \quad (1)$$

1025 where  $M$  and  $O$  stand for model and observation results, respectively. The time average is indicated over  $n$  time intervals (number of observations). The time average is done for one year.

$$\text{Correlation (R)} = \frac{1}{(n-1)} \sum_1^n \left( \left( \frac{O-\bar{O}}{\sigma_o} \right) * \left( \frac{M-\bar{M}}{\sigma_m} \right) \right) \quad (2)$$

$$\text{Root Mean Square Error (RMSE)} = \sqrt{\frac{\sum_1^n (M-O)^2}{n}} \quad (3)$$

1030 RMSE is a measure of accuracy and allows prediction errors of different models to be compared for a particular dataset.





## Appendix B:

**Table B1: detailed overview of monitoring stations**

Name	Code	Country	Latitude	Longitude	Elevation	Station Type	Data Points	Measured Pollutants
<b>Vlora</b>	al0204a	Albania	40.40309	19.4862	25	urban background	6850	benzene, CO, NO <sub>2</sub> , NO <sub>x</sub> , O <sub>3</sub> , PM <sub>10</sub> , PM <sub>2.5</sub> , SO <sub>2</sub>
<b>Shkoder</b>	al0206a	Albania	42.3139	19.52342	13	urban background	7536	CO, NO <sub>2</sub> , NO <sub>x</sub> , O <sub>3</sub> , PM <sub>10</sub> , PM <sub>2.5</sub> , SO <sub>2</sub>
<b>Els Torms</b>	es0014r	Spain	41.39389	0.73472	470	rural background	8549	NO, NO <sub>2</sub> , NO <sub>x</sub> , O <sub>3</sub> , SO <sub>2</sub>
<b>Vila-seca (RENFE)</b>	es1117a	Spain	41.11209	1.151824	41	suburban background	8594	NO, NO <sub>2</sub> , NO <sub>x</sub>
<b>Sant Celoni (Carles Damm)</b>	es1275a	Spain	41.68905	2.495747	145	suburban background	7180	NO, NO <sub>x</sub> , NO <sub>2</sub> , SO <sub>2</sub>
<b>Barcelona (Ciutadella)</b>	es1679a	Spain	41.38641	2.187417	7	urban background	8565	NO, NO <sub>2</sub> , NO <sub>x</sub>
<b>Mataró (passeig dels Molins)</b>	es1816a	Spain	41.54716	2.443254	40	urban background	8484	NO, NO <sub>x</sub> , NO <sub>2</sub> , O <sub>3</sub> , CO
<b>Barcelona (Palau Reial)</b>	es1992a	Spain	41.38748	2.11515	81	urban background	8393	NO, NO <sub>2</sub> , NO <sub>x</sub> , SO <sub>2</sub> , CO
<b>Marseille 5 Avenues</b>	fr03043	France	43.30607	5.395794	73	urban background	8585	NO <sub>2</sub> , O <sub>3</sub> , PM <sub>10</sub> , PM <sub>2.5</sub> , SO <sub>2</sub>
<b>Esterel</b>	fr03070	France	43.43786	6.768366	5	suburban background	1820	NO <sub>2</sub> , O <sub>3</sub>
<b>Agathois-piscénois</b>	fr08022	France	43.28776	3.504831	20	suburban background	8382	NO <sub>2</sub> , O <sub>3</sub>
<b>Gauzy</b>	fr08614	France	43.8344	4.374219	40	urban background	8406	NO <sub>2</sub> , O <sub>3</sub> , PM <sub>10</sub> , PM <sub>2.5</sub>
<b>Rigaud</b>	fr08713	France	42.68402	2.903453	50	urban background	8419	NO <sub>2</sub> , PM <sub>10</sub>



<b>Cannes Broussilles</b>	fr24009	France	43.5625	7.007222	71	urban background	8587	NO <sub>2</sub> , O <sub>3</sub> , PM <sub>10</sub> , PM <sub>2.5</sub>
<b>Manosque</b>	fr24018	France	43.83527	5.785831	385	urban background	8517	NO <sub>2</sub> , O <sub>3</sub> , PM <sub>10</sub> , PM <sub>2.5</sub>
<b>Nice Arson</b>	fr24036	France	43.70207	7.286264	11	urban background	8701	NO <sub>2</sub> , O <sub>3</sub> , PM <sub>10</sub> , PM <sub>2.5</sub>
<b>Ajaccio Sposata</b>	fr41007	France	41.94923	8.757586	60	suburban background	8497	NO <sub>2</sub> , O <sub>3</sub>
<b>Bastia Montesoro</b>	fr41017	France	42.67134	9.434644	47	rural background	8626	NO <sub>2</sub> , O <sub>3</sub> , PM <sub>2.5</sub>
<b>Lykovrysi</b>	gr0035a	Greece	38.06963	23.77689	210	suburban background	6719	NO <sub>2</sub> , NO <sub>2</sub> , O <sub>3</sub>
<b>Neochorouda</b>	gr0045a	Greece	40.73984	22.87623	229	suburban background	8725	NO <sub>2</sub> , NO, O <sub>3</sub>
<b>Finokalia</b>	gr0002r	Greece	35.315871	25.666216	250	rural background	6825	PM <sub>10</sub> , O <sub>3</sub>
<b>NA</b>	hr0012a	Croatia	46.16906	15.66064	0	rural background	6063	NO <sub>2</sub> , NO <sub>x</sub> , O <sub>3</sub> , PM <sub>10</sub> , PM <sub>2.5</sub>
<b>NA</b>	hr0025a	Croatia	44.86247	13.81686	0	suburban background	8293	NO <sub>2</sub> , NO <sub>x</sub> , O <sub>3</sub>
<b>Melilli</b>	it0611a	Italy	37.18237	15.12883	300	urban background	7964	NO <sub>2</sub> , O <sub>3</sub> , SO <sub>2</sub>
<b>Priolo</b>	it0614a	Italy	37.15612	15.19087	35	urban background	7902	NO <sub>2</sub> , benzene, SO <sub>2</sub>
<b>SR - Via Gela</b>	it0620a	Italy	37.10247	15.26564	60	suburban background	6958	NO <sub>2</sub> , O <sub>3</sub> , SO <sub>2</sub>
<b>Gambara</b>	it0741a	Italy	45.24889	10.29944	51	suburban background	8413	NO <sub>2</sub> , O <sub>3</sub>
<b>Gela Enimed</b>	- it0815a	Italy	37.06222	14.28422	13	suburban background	8052	NO <sub>2</sub> , benzene, SO <sub>2</sub>
<b>Aprilia</b>	it0865a	Italy	41.59528	12.65361	83	urban background	8169	NO <sub>2</sub>



<b>Leonessa</b>	it0989a	Italy	42.5725	12.96194	948	urban background	8207	NO <sub>2</sub> , O <sub>3</sub>
<b>Gherardi</b>	it1179a	Italy	44.83972	11.96111	-2	rural background	8269	NO <sub>x</sub> , NO <sub>2</sub> , O <sub>3</sub>
<b>Adria</b>	it1213a	Italy	45.04667	12.06194	4	urban background	8306	NO <sub>2</sub> , NO <sub>x</sub> , O <sub>3</sub>
<b>Cennm1</b>	it1375a	Italy	39.44361	9.015278	124	rural background	7595	NO <sub>2</sub> , SO <sub>2</sub>
<b>Teatro d'Annunzio</b>	it1423a	Italy	42.45639	14.23472	4	urban background	8135	NO <sub>2</sub> , O <sub>3</sub> , PM <sub>10</sub> , PM <sub>2.5</sub> , SO <sub>2</sub> , benzene, CO
<b>Cenps7</b>	it1576a	Italy	39.20333	8.386111	25	suburban background	7968	CO, NO <sub>2</sub> , SO <sub>2</sub>
<b>Taranto San Vito</b>	it1610a	Italy	40.42333	17.22528	10	urban background	7871	NO <sub>2</sub>
<b>Lecce - S.M. Cerrate</b>	it1665a	Italy	40.45889	18.11611	10	rural background	7290	NO <sub>2</sub> , O <sub>3</sub>
<b>Brindisi Via Magellano</b>	it1702a	Italy	40.65083	17.94361	10	suburban background	7904	NO <sub>2</sub> , PM <sub>10</sub>
<b>Genga - Parco Gola della Rossa</b>	it1773a	Italy	43.46806	12.95222	550	rural background	5310	NO <sub>2</sub> , O <sub>3</sub> , PM <sub>10</sub> , PM <sub>2.5</sub> , SO <sub>2</sub> , benzene, CO
<b>Civitanova Ippodromo S. Marone</b>	it1796a	Italy	43.33556	13.67472	110	rural background	6699	NO <sub>2</sub> , NO <sub>x</sub> , O <sub>3</sub> , PM <sub>10</sub> , PM <sub>2.5</sub> , benzene
<b>Guardiaregia</b>	it1806a	Italy	41.41889	14.52556	884	rural background	7892	NO <sub>2</sub> , NO <sub>x</sub> , O <sub>3</sub> , SO <sub>2</sub>
<b>Ancona Cittadella</b>	it1827a	Italy	43.61167	13.50861	100	urban background	5985	NO <sub>2</sub> , O <sub>3</sub> , PM <sub>10</sub> , PM <sub>2.5</sub> , benzene, CO, SO <sub>2</sub>
<b>Schivenoglia</b>	it1865a	Italy	44.99694	11.07083	16	rural background	8325	NO <sub>2</sub> , NO <sub>x</sub> , O <sub>3</sub> , SO <sub>2</sub> , benzene
<b>Trapani</b>	it1898a	Italy	38.01237	12.54689	40	urban background	7396	NO <sub>2</sub> , O <sub>3</sub> , benzene, CO



<b>San Rocco</b>	it1914a	Italy	44.87306	10.66389	22	rural background	8398	NO <sub>2</sub> , NO <sub>x</sub> , O <sub>3</sub>
<b>Locri</b>	it1940a	Italy	38.22976	16.25518	11	urban background	8509	NO <sub>2</sub> , O <sub>3</sub> , SO <sub>2</sub> , benzene, CO
<b>GR Maremma</b>	- it1942a	Italy	42.67056	11.09417	40	rural background	7784	NO <sub>2</sub> , O <sub>3</sub>
<b>Censa3</b>	it1947a	Italy	39.06667	9.008889	56	urban background	8169	NO <sub>2</sub> , SO <sub>2</sub> , benzene
<b>Milazzo Termica</b>	- it1997a	Italy	38.19061	15.24911	28	suburban background	8329	NO <sub>2</sub> , O <sub>3</sub> , CO, benzene
<b>Stadio Casardi</b>	it2003a	Italy	41.31667	16.28611	15	urban background	8391	NO <sub>2</sub> , O <sub>3</sub> , benzene
<b>Cenqu1</b>	it2040a	Italy	39.23278	9.188056	8	urban background	8181	NO <sub>2</sub> , O <sub>3</sub> , SO <sub>2</sub> , benzene
<b>Carbonara</b>	it2051a	Italy	41.07694	16.86583	130	suburban background	7505	NO <sub>2</sub> , PM <sub>10</sub>
<b>Cremona Gerre Borghi</b>	it2095a	Italy	45.10954	10.06924	36	rural background	5828	NO <sub>2</sub> , O <sub>3</sub>
<b>Ceglie Messapica</b>	it2148a	Italy	40.64917	17.5125	100	suburban background	8393	NO <sub>2</sub> , PM <sub>10</sub> , PM <sub>2.5</sub> , SO <sub>2</sub> , CO, benzene
<b>LI Piombino-Parco-VIII-Marzo</b>	- it2154a	Italy	42.93194	10.52417	40	urban background	8228	NO <sub>2</sub> , benzene
<b>Gela - Biviere</b>	it2206a	Italy	37.02249	14.34497	0	rural background	8277	NO <sub>2</sub> , O <sub>3</sub> , SO <sub>2</sub>
<b>Bar2</b>	me0008a	Montenegro	42.10035	19.10348	12	urban background	7721	CO, NO, NO <sub>2</sub> , NO <sub>x</sub> , O <sub>3</sub> , SO <sub>2</sub>
<b>Niskic2</b>	me0009a	Montenegro	42.78121	18.94291	629	urban background	7693	CO, NO, NO <sub>2</sub> , NO <sub>x</sub> , O <sub>3</sub> , SO <sub>2</sub>
<b>Celje</b>	si0001a	Slovenia	46.23448	15.26244	240	urban background	7371	NO <sub>2</sub> , NO <sub>x</sub> , O <sub>3</sub> , SO <sub>2</sub>
<b>Nova Gorica</b>	si0034a	Slovenia	45.95551	13.6524	113	urban background	8273	NO <sub>2</sub> , NO <sub>x</sub> , O <sub>3</sub>



---

<b>Koper</b>	si0038a	Slovenia	45.54297	13.71354	56	urban background	8198	NO <sub>2</sub> , NO <sub>x</sub> , O <sub>3</sub>
<b>Balikesir- Bandirma</b>	tr100241	Turkey	40.34795	27.97496	38	urban background	8509	NO <sub>2</sub>
<b>Canakkale- Lapseki</b>	tr170313	Turkey	40.40307	26.77063	12	rural background	8170	NO <sub>2</sub> , NO <sub>x</sub> , O <sub>3</sub> , PM <sub>2.5</sub> , SO <sub>2</sub>
<b>Istanbul- Esenyurt</b>	tr340241	Turkey	41.02028	28.66955	36	urban background	7915	NO <sub>2</sub> , NO <sub>x</sub> , SO <sub>2</sub>
<b>Istanbul- Sultangazi</b>	tr340841	Turkey	41.10197	28.87202	128	urban background	8304	NO <sub>2</sub> , NO <sub>x</sub> , SO <sub>2</sub>
<b>Kirkareli- Luleburgaz-</b>	tr390441	Turkey	41.39841	27.34588	56	rural background	8393	NO <sub>2</sub> , SO <sub>2</sub>

---



### Appendix C: Diurnal cycles of O<sub>3</sub>

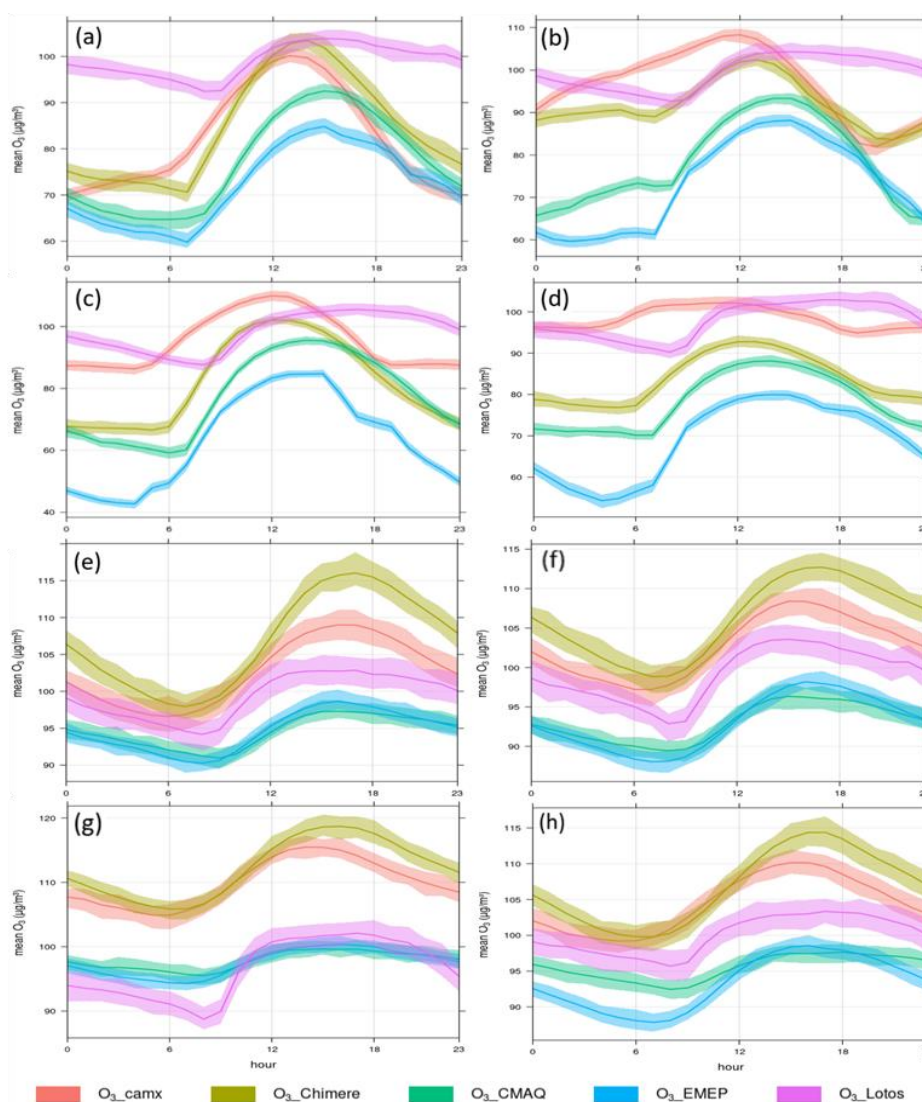


**Figure C1: Diurnal cycle of O<sub>3</sub> in grid cells over land: (a) = Location 1, (b) = Location 2, (c) = Location 3, (d) = Location 4. Diurnal cycle of O<sub>3</sub> in grid cells over water: (e) = Location 5, (f) = Location 6, (g) = Location 7, (h) = Location 8. The map displays the location of the respective chosen grid cell.**



### Appendix D: NO<sub>x</sub> Spatial Distribution

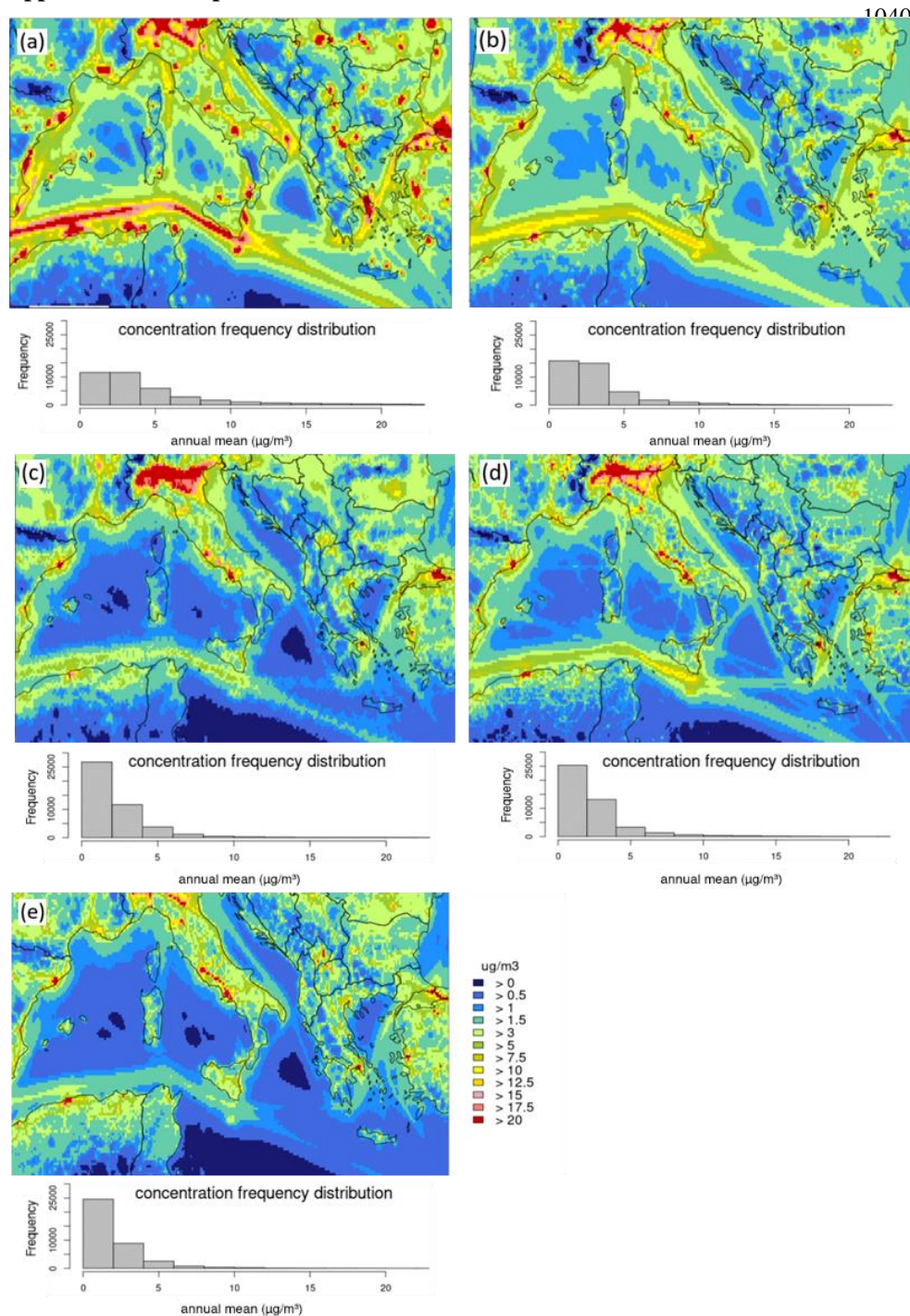


**Figure C2: Annual total dry deposition of NO<sub>x</sub>.** (a) = CAMx, (b) = CHIMERE, (c) = CMAQ, (d) = LOTOS-EUROS. Below maps the respective frequency distribution is displayed for the annual mean NO<sub>x</sub> dry deposition, referred to the whole model domain.

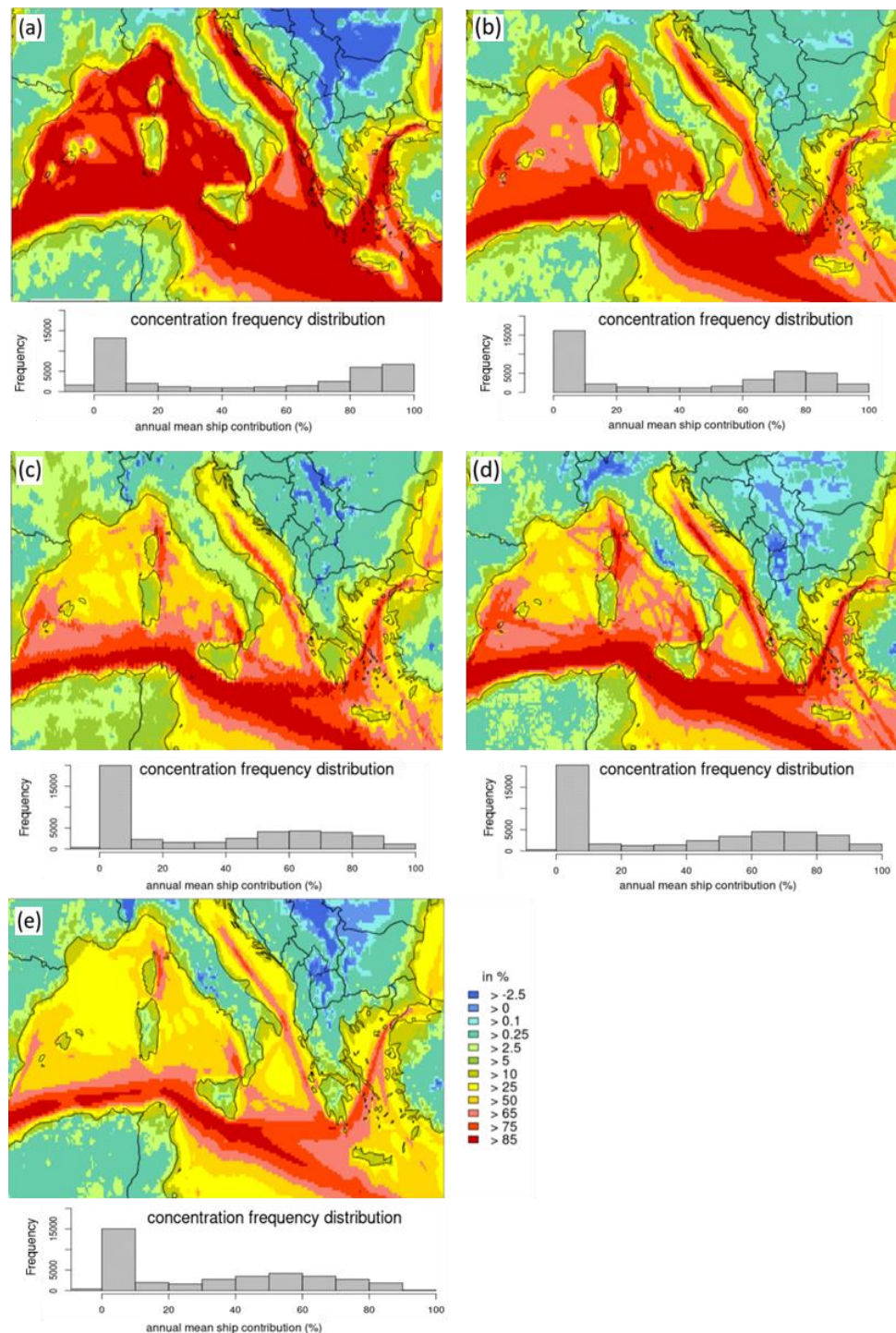


**Figure C3: Annual mean relative ship contribution of  $\text{NO}_x$ . (a) = CAMx, (b) = CHIMERE, (c) = CMAQ, (d) = LOTOS-EUROS. Below maps the respective frequency distribution is displayed for the annual mean relative ship contribution of  $\text{NO}_x$ , referred to the whole model domain.**





### Appendix E: annual total dry deposition of N

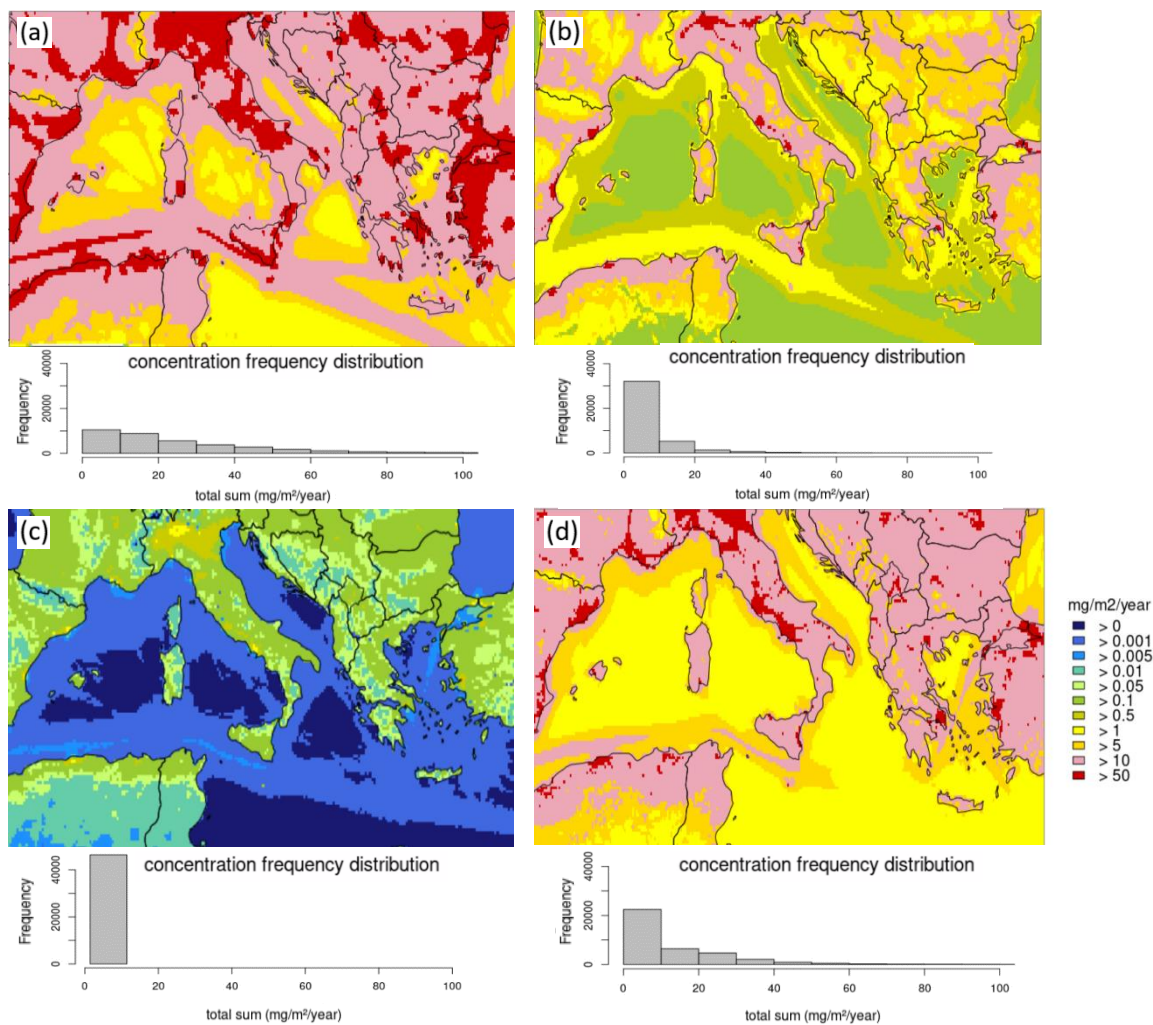


**Figure C4:** Annual total dry deposition of N. (a) = CAMx, (b) = CHIMERE, (c) = CMAQ, (d) = LOTOS-EUROS.